Synchrotron X-ray Scattering Studies of Novel Phase Transitions in Systems with Coupled Order Parameters

by

Qun Joan Harris

B. Sc. Shanghai Jiao Tong University, China
(1989)

Submitted to the Department of Physics
in partial fulfillment of the requirements for the degree of

Doctor of Philosophy

at the

MASSACHUSETTS INSTITUTE OF TECHNOLOGY

September 1996

Author . . . . . .
Department of Physics
August 5th, 1996

Certified by . . . . . .
Robert J. Birgeneau
Dean of Science and Cecil and Ida Green Professor of Physics
Thesis Supervisor

Accepted by . . . . . .
George F. Koster
Chairman, Departmental Committee on Graduate Students

Synchrotron X-ray Scattering Studies of Novel Phase Transitions in Systems with Coupled Order Parameters

by

Qun Joan Harris

Submitted to the Department of Physics
on August 5th, 1996, in partial fulfillment of the
requirements for the degree of
Doctor of Philosophy

Abstract

Many physical systems exhibit interesting critical behavior which depends on the interplay of more than one order parameter. In this thesis, we report experimental studies of the spin-Peierls transition in $CuGeO_3$ and the phases and phase transitions in the mixed Ising-XY magnets with quenched randomness: $Fe_xCo_{1-x}TiO_3$, by using synchrotron x-ray scattering techniques.

In $CuGeO_3$, below the spin-Peierls transition temperature T_{sp}, the superlattice peak resulting from the lattice dimerization has a resolution limited profile, and the peak intensity, which is proportional to the order parameter squared, is well described by a simple power law, $(1 - T/T_{sp})^{2\beta}$. The best fit value of β is 0.33(3). In addition, a spontaneous thermal contraction Δb along the b-axis perpendicular to the chain direction was observed below the spin-Peierls transition temperature T_{sp}. This contraction, Δb, is found to scale like the dimerization squared, $\Delta b \sim \delta^2$. The shift of the transition temperature in magnetic fields, $\Delta T \equiv T_{sp}(0) - T_{sp}(0)$, is found to scale as H^2 in quantitative agreement with the results of magnetic susceptibility measurements and with theory. A small increase in the a-axis lattice constant is observed below T_{sp}. Above the transition temperature T_{sp}, pre-transitional lattice fluctuations are observed within about 1K above T_{sp}. The length scale of these fluctuations is about an order of magnitude larger than that characterizing the bulk critical fluctuations. The line shape of these large length scale fluctuations is consistent with a Lorentzian-squared form. The measured critical exponents associated with the large length scale fluctuations are $\nu = 0.56(9)$, and $\bar{\gamma} = 2.0(3)$. Similar large length scale fluctuations have been observed at the structural transitions in some perovskites and the magnetic transitions in holmium and terbium. We suggest that in $CuGeO_3$ the large length scale fluctuations reflect the disconnected susceptibility originating from random field Ising-type local defects.

In $Fe_xCo_{1-x}TiO_3$, for concentrations $x = 0.35$, 0.50 and 0.65, we observe at high resolution a breakup of both the magnetic and the atomic structures of the crystal into domains, as well as a uniform lattice distortion following the ordering of the XY spin components. We argue that this breakup into domains in the XY phases results

from random anisotropy, random field and magnetoelastic effects in $Fe_xCo_{1-x}TiO_3$. In particular, we find that in random anisotropy XY magnets, there exists a novel phase transition which is critical, but involves no long-range ordered phase. In addition to the XY behavior, the Ising spin component in the mixed phase ($x = 0.65$) is found to break into domains following the (short range) ordering of the XY spin components. Specifically, the scattering profiles of the low temperature mixed states are well described by a Lorentzian squared cross-section, which in three dimensions corresponds to exponential decay of the real space spin-spin correlations. This loss of the long-range order of the Ising order due to the ordering of the XY spin components after initial establishment of the Ising order on cooling is difficult to understand within our current picture of the random field Ising model. Furthermore, we have also carried out a detailed study of the magnetic field effects on phase transitions in the mixed Ising random magnet $Fe_{0.75}Co_{0.25}TiO_3$, for fields up to 3T. It is found, as in the diluted Ising antiferromagnets $Mn_xZn_{1-x}F_2$ and $Fe_xZn_{1-x}F_2$, that when the sample is cooled in the presence of a field, it evolves from the high temperature paramagnetic phase to a low temperature domain state. The low temperature scattering profiles are well described by a Lorentzian squared cross-section. However, if the sample is cooled below the Néel temperature T_N in the absence of a field, and a magnetic field is subsequently applied, the long range magnetic order persists on warming, up to a well defined field-dependent metastability temperature, $T_M(H)$. The shedding of this LRO in the metastable region is consistent with the "*trompe l'oeil* critical behavior" description, with a $\beta_{ZFC} \sim 0.15$. The depression of the metastability temperature in magnetic fields can be well described by $T_M(H) = T_N(0) - bH^2 - aH^{2/\phi}$, with the best fit value for the crossover exponent $\phi = 1.2(1)$. This smaller value (than the theoretical value $\phi = 1.4$) for ϕ arises from the close proximity of a multicritical point at higher fields. At the superlattice reciprocal lattice point $(1, 1, -1.5)$, we observe a drastic field-dependence of the x-ray, but not the neutron, scattering intensity. This additional x-ray intensity is believed to arise from a staggered lattice distortion. In particular, the quadratic magnetic field dependence of the additional intensity is consistent with a lattice and magnetism coupling of the form, $\delta_s M_s M$.

Thesis Supervisor: Robert J. Birgeneau
Title: Dean of Science and Cecil and Ida Green Professor of Physics

Acknowledgments

Throughout the years of studying and research that have led to the completion of this thesis, I have received enormous help from teachers, friends and family. My personal and intellectual debts are numerous and large.

I am extremely fortunate to have an unusually brilliant and inspirational thesis supervisor, Prof. Bob Birgeneau. I am very grateful for Bob's guidance and generous support, which includes, but is by no means limited to, patiently correcting the grammar mistakes of my manuscripts in spite of his busy schedule as the Dean. Bob's deep physics insights, quick mind and elegant approaches have contributed immensely to my enjoyment and appreciation of the subject.

I consider it a great honor to have had the opportunity of working with the legendary Dr. Gen Shirane of Brookhaven National Laboratory, whose ability to quickly identify a problem in experiments, or an important feature of the data, benefited me a great deal. That he is able to do this in his 70s remains a wonder to me. I also thank him for his kindness of coming in on Sunday mornings to offer his generous dose of "moral support" when experiments were not going smoothly.

It is a privilege to have Prof. Patrick Lee and Prof. Larry Ronsenson on my thesis committee. I would also like to thank Prof. A Ito, Prof. K. Uchinokura and Dr. M. Hase for giving me the opportunity to work on two of the most beautiful physics problems.

The completion of this thesis involved research work carried out both on campus at MIT, and off-campus at Brookhaven Nationa Laboratory. At both places, I received enormous help from scientists and administrators. At MIT, thanks are due to the past and present members of Bob's group: Do Young Noh, John Hill, Qiang Feng, Barry Wells, Bill Nuttall, Monte Ramsted, Mike Young, Fang Chou, Yongmei Shao, Doug Turnbull, Bernhard Keimer, Kenny Blume, Kevin Fahey, Young Sang Lee, Young-June Kim, Patrick Mang, Rebecca Christianson, Yujie Wang, Sungil Park and Michelle Girvan. In particular, I thank Doyoung and John for patiently teaching me how to conduct synchrotron x-ray experiments, and continuing to be invaluable

sources of help and advice throughout my many experimental runs at BNL. I am very grateful to Qiang, who helped me on all my experiment runs. Qiang's talent and pleasantness contributed greatly to the success and my enjoyment of the synchrotron experiments. Special thanks are also due to Young, Young-June and Yujie for their help with the experiments in the critical stage of my thesis research, to Barry for many physics discussions, and to Rebecca for her proof-reading of this thesis and her friendship. In addition, I would like to thank Mirang Yoon, Seungheon Song and Beth Parks for their help and friendship. I am also grateful to Debra Martins, Peggy Berkovitz, Ann-Marie LeBlanc, Karen Fosher, Ron Hassaltine, Betty Bradley, Janet Salstrom and Prof. Mary Rowe for their help in making my work and life at MIT productive and enjoyable. On the Brookhaven side, I would like to thank Dr. Jean Jordan-Sweet and Rene Holaday of Light Source for their help with various equipment problems at the beamline, Dr. Steve Shapiro of BNL for his help with my neutron experiment at HFBR, and Maria Grahn for being ever so helpful and thoughtful.

I would like to thank Prof. Samuel Ting for providing me the opportunity of working in his research group at CERN prior to my graduate study. I would also like to thank Prof. William Bertozii for the opportunity of working in his research group during my first year at MIT.

I would like to thank Diane and Jim Craig of Concord for many wonderful weekends and holidays I spent out in Concord. Special thanks are also due to Wen Zhang for her friendship. I met Wen when we were 12 years old, and ever since then she has been a constant source of encouragement and help for me both in Shanghai and abroad.

I am deeply, deeply grateful to my parents and my late grandmother for their tremendous love and support, in particular, for the efforts and sacrifice they made in securing a good education for me. I thank my brother and my sister-in-law Juejue for being ever so supportive and understanding. I thank my parents-in-law for welcoming me to England with open arms during my three month stay in the UK in 1991, and for their help with the wedding. I thank my other sister-in-law Elizabeth for her friendship. I thank my nephew Angang for the joy he brings to me.

Finally, I am indebted to my husband Christopher, whose unfailing love and support I am eternally grateful for, and whose talent I greatly admire. Above and beyond any call of duty, Christopher endured all the inconvenience of a trans-atlantic marriage to allow me to finish my degree at MIT, and accompanied me on my numerous experiment trips to Brookhaven, where not only did he put up with my long and haphazard hours, he did so without a single word of complaint. It is with the utmost gratitude and love I dedicate this thesis to him.

Contents

List of Figures

List of Tables

Chapter 1

Introduction

1.1 Phase Transitions

Phase transitions are a fascinating field of study. During a phase transition, such as the transformation from a thermally disordered paramagnetic state to an ordered ferromagnetic state, in which the neighboring spins tend to align parallel to each other, large number of particles, typically of the order of 10^{23}, behave collectively. Proper description of this cooperative behavior at the phase transition is a challenging problem for both experimentalists and theoreticians. Given the number of particles involved, there is apparently little hope of finding out how each particle behaves with respect to its neighbors. Moreover, even if such a solution existed, it would prove impossible to monitor experimentally the motion of the 10^{23} or so particles at the same time.

We can, however, measure some macroscopic variables, such as the magnetization, $\mathbf{M}$, and from these macroscopic variables, we can easily distinguish one state from the other. For instance, in the case of a paramagnet-to-ferromagnet phase transition, the magnetization $\mathbf{M} = 0$ in a paramagentic state, and $\mathbf{M} \neq 0$ in a ferromagnetic state. The existence of a quantity which is non-zero in one state, and zero in the other state is a common feature with a wide variety of physical systems. We say that the magnetization $\mathbf{M}$ is the *order parameter* for the paramagnet-to-ferromagnet phase transition. In a phase transition between a paramagnet and an antiferromagnet in

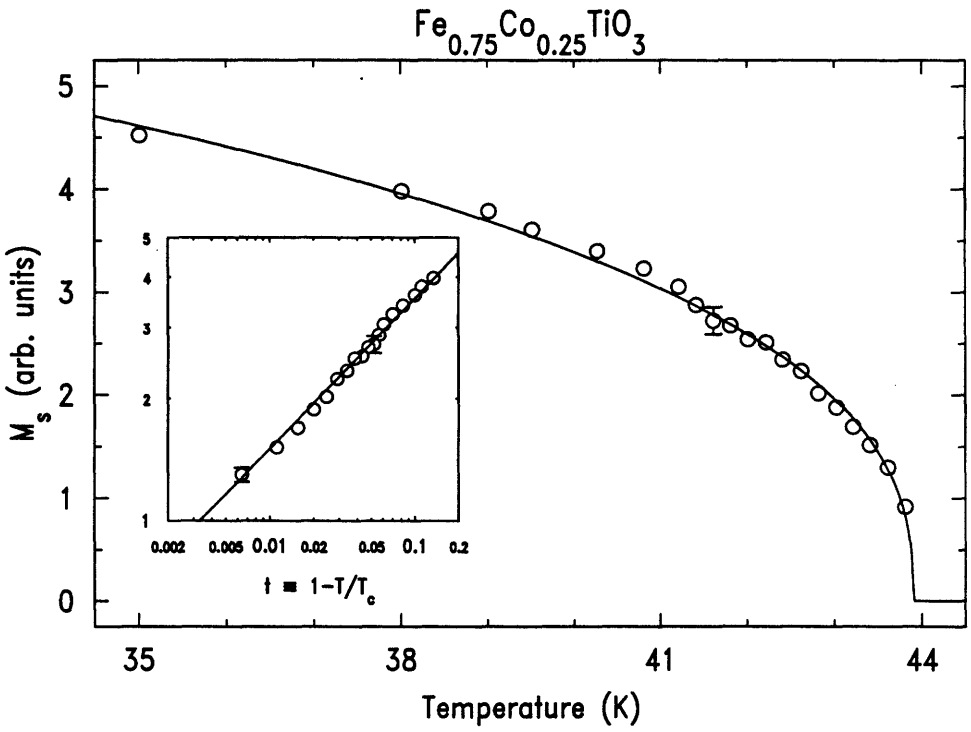

Figure 1-1: The growth of the sublattice magnetization as a function of temperature for single crystal $Fe_{0.75}Co_{0.25}TiO_3$. For T close to T_c, the growth is well described by a power law, $M_s \propto \left(1 - \frac{T}{T_c}\right)^{\beta}$. The solid line in the figure represents the best fit of the data, with the fit β value of 0.36(3). The inset shows the same plot on a log-log scale, and the horizontal axis is the reduced temperature, $t \equiv 1 - \frac{T}{T_c}$.

which the neighboring spins tend to align anti-parallel to each other, the *sublattice* magnetization $\mathbf{M}_s$ serves as the order parameter.

The order parameter usually grows in a certain fashion from zero to non-zero, for an example, Fig. 1-1 shows the evolution of the sublattice magnetization in a transition from a paramagnetic state to an ordered antiferromagnetic state for a single crystal $Fe_{0.75}Co_{0.25}TiO_3$. At a temperature, T_c, there is a sudden rise of the order parameter, M_s. We call T_c *transition temperature.*

For T close to the transition temperature T_c, we notice that the sublattice mag-

netization, M_s, follows a simple power law (Fig. 1-1),

$$M_s \propto \left(1 - \frac{T}{T_c}\right)^{\beta} \tag{1.1}$$

The power law behavior of certain macroscopic variables near the transition temperature is another common feature of phase transitions in a wide variety of physical systems. The index on power, such as β, is called a *critical exponent.* Furthermore, while the transition temperature T_c depends sensitively on the details of the interatomic interactions, and therefore varies considerably from system to system, the critical exponents, such as β, for a continuous phase transition depend on the following three properties and nothing else [1, 2, 3, 4]:

- The dimensionality of the system, d.
- The dimensionality of the order parameter, n, or more precisely, the symmetry of the order parameter; in simple cases, this is equivalent to the number of dimensions in which the order parameter is free to vary.
- Whether the forces between the particles are of short or long range

This enormous generalization is the hypothesis of *universality* [5, 6, 7]. Since it has not been "proven" from more basic ideas, the correctness of universality must be judged by reference to experiments, where in fact measurements seem to support the hypothesis. There are still some doubts as to how good universality is. For instance, Haldane [8, 9] has conjectured different behaviors for one-dimensional magnetic systems with integer and half-integer spins, but, nonetheless, the hypothesis of universality forms a reasonable starting proposition from which to proceed to other questions.

We know that most real systems are three-dimensional ($d = 3$). So when we say the dimensionality of a system is one ($d = 1$) or two ($d = 2$), we usually mean that the one-dimensional (1D) or two-dimensional (2D) systems are actually imbedded in real three-dimensional (3D) systems. In some materials, within the (temperature) region concerned, the interactions between the particles along one direction (1D) or within a particular plane (2D) are much stronger than the interactions along the other

directions. Examples for lower dimensional magnetic systems include $CsNiF_3$ (1D) [10], $(CD_3)_4NMnCl_3$ (TMMC) (1D) [11], K_2NiF_4 (2D) [12] and Rb_2CoF_4 (2D) [13].

We shall again use the language of a magnetic phase transition to explain the dimensionality of the order parameter (n). Due to the detailed atomic arrangements of a system, the spins may be confined to align along one particular axis, we call this magnetic system an *Ising* magnet ($n = 1$); or, the spins may be confined to vary within a particular plane, we then have an XY magnet ($n = 2$); or, there may be no restrictions on spins' direction at all, *i.e.* the spins are allowed to point in any direction, this system is then called a *Heisenberg* magnet ($n = 3$).

The hypothesis of universality also says that the details of the the microscopic interactions between particles, that is, whether they are electronic or magnetic, are irrelevant, the only relevant part regarding the interatomic interactions is whether the interactions themselves are short-ranged or long-ranged, *i.e.* whether the interactions are confined to neighboring sites or they extend beyond the nearest neighbors.

1.2 Coupled Order Parameters

In some physical systems, there are more than one order parameters, or the order parameter itself has several components. The ultimate critical behavior near a phase transition of such systems understandably depends on the interplay of these order parameters, or the different components of the order parameter. A well-studied example is that of a uniaxially anisotropic antiferromagnet in a uniform magnetic field [14, 15, 16, 17], in which spins may order antiferromagnetically parallel to the field for low values of the field, or transverse to the field for high values of the field. A second example is that of the structural displacive phase transition in stressed perovskite crystals, where the direction of the rotations of the atomic octahedra depends on the external uniaxial stress [18, 19, 20].

In this thesis, we present experimental studies of two such systems, which exemplify the importance of the coupled order parameters:

Spin-Peierls Systems

For an ideal one-dimensional magnetic system with short-range interactions, ordering can occur only at $T = 0$K [21]. Weak interchain interactions are therefore necessary to induce a phase transition at a finite temperature $T_c \neq 0$.

For a crystal made up of one-dimensional (1D), spin half-integer, antiferromagnetic Heisenberg or XY chains in a 3D lattice, there are two possibilities: (1) If the interchain interactions are magnetic, the transition leads to a magnetic ordered state below T_c. This ordering temperature is related to the ratio of the interchain to intrachain coupling. (2) Alternatively, if the lattice is allowed to distort, the uniform spin chain can then undergo a phase transition at a transition temperature T_{sp} to a dimerized state. This can be visualized as a state in which neighboring pairs of ions are displaced from their "uniform positions" alternately closer and further apart. This transition is referred as *spin-Peierls transition*, for its close similarity to the Peierls transition in 1D metals [22]. In the spin-Peierls transition, the interchain couplings are in the form of a three-dimensional phonon field. Spin-Peierls transition is therefore a structural transition driven by the coupling between a 1D spin system and a 3D phonon field. The onset of a spin-Peierls transition precludes additional magnetic ordering at lower temperatures; and the onset of a magnetic ordering, in turn, prohibits further spin-Peierls transition in the system.

In real systems, usually neither the interchain magnetic coupling is zero, nor the lattice is completely rigid. We can therefore view the situation as a competition between the magnetic order, which is driven by the interchain magnetic couplings, and the dimerization, which is driven by the couplings of the 1D magnetic interactions and the 3D phonon fields. In the case that the former wins, we will have a low temperature magnetic ordered state. In the spin-Peierls systems, in which we are interested in this thesis, it is the spin-phonon coupling that wins the battle. There are not many 1D magnetic systems in the nature, moreover, there are even fewer cases when the spin-lattice coupling wins its battle with the conventional magnetic order. In Part I of this thesis, which includes Chapter 2, Chapter 3, Chapter 4 and Chapter 5, we report a detailed experimental study on the first known, and to-date, the only

known, inorganic spin-Peierls system $CuGeO_3$. The advantage of being inorganic is that the sample does not deteriorate in an x-ray or neutron beam, which therefore allows for a detailed experimental investigation.

Mixed Ising-XY Magnets with Quenched Randomness

Suppose that we have two magnetic systems A and B, each undergoes a paramagnet-to-ferromagnet phase transition at temperatures T_c^A and T_c^B respectively. The only difference between A and B is that in system A the magnetization is within one particular plane, say, the x-y plane, while the magnetization in system B is confined to a particular direction, say, the z-axis direction, which is perpendicular to the x-y plane. This is to say that for system A,

$$\mathbf{M}^A = \begin{cases} 0 & T \geq T_c^A \\ (M_x^A, M_y^A, 0) \text{ or } (\mathbf{M}_\perp^A, 0), \text{ where } |\mathbf{M}_\perp^A|^2 \equiv (M_x^A)^2 + (M_y^A)^2 \neq 0 & T < T_c^A \end{cases}$$

and for system B,

$$\mathbf{M}^B = \begin{cases} 0 & T \geq T_c^B \\ (0, 0, M_z^B), \text{ where } M_z^B \neq 0 & T < T_c^B \end{cases}$$

In other words, systems A and B exhibit XY and Ising behavior respectively. Now if we mix A and B together to form crystalline random mixtures of A_xB_{1-x}, where x is the concentration of system A in the mixtures, $0 \leq x \leq 1$. Clearly, in the binary compounds A_xB_{1-x}, there is competition between the ordering of the different components $\mathbf{M}_\perp$ and M_z of the magnetization. This can be understood by considering two extreme cases: (1) for very small $x \sim 0$, the phase behavior in the mixed systems is expected be similar to that of system B (in the case of $x = 0$, we simply go back to system B), *i.e.* in the mixture, the behavior of the magnetic component M_z dominates over that of the magnetic component $\mathbf{M}_\perp$; (2) alternatively, for x close to one, we expect the phase behavior in the mixed systems to be similar to that of system A (when $x = 1$, we return to system A), *i.e.* the component $\mathbf{M}_\perp$ is more significant

than the component M_z.

But how about a mixed system with x being neither very close to zero, nor very close to one? Naively, we would expect that the spin component in the x-y plane, $\mathbf{M}_\perp$, follows the behavior of $\mathbf{M}^A$, while the spin component along the z-axis, M_z, mimics the behavior of $\mathbf{M}^B$. Do real mixed magnetic systems behave like this? What are the other factors we must consider in a random mixed magnetic system? Part II of this thesis, which includes Chapter 6, Chapter 7 and Chapter 8, reports an experimental study of one physical realization of such mixed Ising-XY magnetic systems with quenched randomness: $Fe_xCo_{1-x}TiO_3$.

In both cases, the phase transitions involve the change of the structure, that is, magnetic (and atomic) in $Fe_xCo_{1-x}TiO_3$ and atomic in $CuGeO_3$. This makes the scattering technique an excellent choice of the tool in investigating the phase transitions in these two systems. In particular, we used synchrotron x-ray scattering techniques in studying of these two systems with coupled order parameter — $CuGeO_3$ and $Fe_xCo_{1-x}TiO_3$.

1.3 Synchrotron X-ray Scattering in Solids

In order to understand the basic physical and chemical behavior of materials, it is usually essential to understand their structures first. For decades, the x-ray scattering technique has been the technique of choice for the precise determination of the geometric arrangements of atoms and molecules in condensed matter. In the past decade, with the high fluxes available from synchrotron radiation sources, the x-ray scattering technique has also established itself as a powerful tool in studying the magnetic structure, that is, the arrangements of the magnetic moments, in magnetic materials. With the high resolution available from synchrotron radiation sources, synchrotron x-ray-scattering experiments allow the detailed study of physical properties at length scales ranging from 0.1 to several microns. These length scales, which often turn out to be very important in understanding some experimental results, for example, the

two length scale phenomenon reported in Chapter 5 of Part I, and in random magnetic materials as illustrated by the results reported in Part II, are generally inaccessible by other experimental techniques.

Synchrotron Radiation

Synchrotron radiation is electromagnetic radiation emitted by charged particle moving with relativistic speeds in curved trajectories. There are three generic kinds of synchrotron radiation sources: bending magnets, wigglers and undulators [23]:

- **Bending Magnets** — In bending magnets, charged particles constrained to move in arc trajectories at relativistic speeds experience a centripetal acceleration and thus radiate, as predicted by Maxwell's equation [24]. The continuous spectrum is produced in bending magnets. The continuous spectrum is also referred to as a "white beam".

- **Wigglers** — A wiggler is a linear array of magnet poles with alternating polarity. An electron beam passing along the axis of the wiggler will execute a trajectory akin to a series of sine-like wiggles. Synchrotron radiation is emitted from each bend in the wiggler. The output is the sum of these emissions.

- **Undulators** — An undulator is very similiar in construction to a wiggler. The essential difference is that the deflection of the electron beam in the undulator is less than, or of the order of the natural emission angle of synchrotron radiation (given by $\theta = \gamma^{-1} \equiv m_0c^2/E$, the ratio of the electron rest mass energy to its total energy). This allows interference between photons from individual wiggles, giving a radiation spectrum consisting of a discrete line together with many harmonics.

Although the synchrotron radiation may come from different sources, they share some common features: exceptionally high brightness, wide tunability, high polarization and narrow angular divergence, and it is these features that make synchrotron radiation an incisive and versatile probe in modern scientific research.

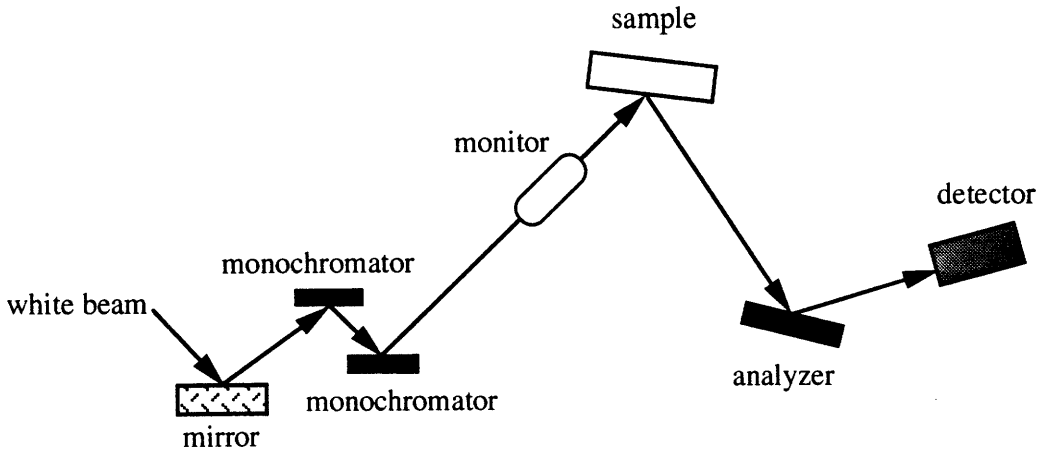

Figure 1-2: The schematic layout for a synchrotron-x-ray scattering experiment.

The Scattering Gemoetry

In Fig. 1-2, we show the setup of a typical synchrotron x-ray scattering experiment. The multi-wavelength beam from the synchrotron radiation source, which is continuous for both bending magnets and wigglers, and discreet for undulators, shines on a mirror, which focuses the beam to a small spot at the sample position, and therefore achieves a high flux density at the sample position. In addition, the mirror also serves to eliminate the higher order harmonics. A single wavelength is then selected by the monochromators. The monochromatic x-ray beam then shines on the sample, and is scattered by the electrons

When an x-ray — an electromagnetic wave — meets an electron in the crystal, the electronic charge is accelerated by the electric field of the wave, and begins to oscillate. This oscillating electron, in turn, emits an electromagnetic wave — the scattered x-ray. However, this is not the full story, since the electromagnetic wave also contains a magnetic field, and the electron has a magnetic moment — both the spin of the electron and its orbital moment. The magnetic field and magnetic moments interact and this interaction produces magnetic scattering.

Therefore, a technically demanding synchrotron x-ray scattering experiment can be simply summarized: x-rays hit the sample, scatter, and an analysis of the dis-

tribution of the intensity of the scattered x-rays reveals information regarding the atomic and magnetic structures of the materials. In the rest of this Section, we will briefly review the formulation of the interactions between x-rays with the electrons in the solids. A full derivation is given in Ref. [25]. X-rays also interact with the protons in the solids. However, this interaction can generally be neglected because the interaction is inversely proportional to the mass of the charged particles, and the mass of a proton is $\sim$ 2000 times that of an electron.

The Hamiltonian

The Hamiltonian for electrons in an electromagnetic field can be written:

$$\begin{aligned}\mathcal{H} &= \sum_j \frac{1}{2m}\left(\mathbf{P}_j - \frac{e}{c}\mathbf{A}(\mathbf{r}_j)\right)^2 + \sum_{ij} V(\mathbf{R}_{ij}) \\ &\quad -\frac{e\hbar}{2mc}\sum_j \mathbf{S}_j \cdot \nabla \times \mathbf{A}(\mathbf{r}_j) - \frac{e\hbar}{2(mc)^2}\sum_j \mathbf{S}_j \cdot \mathbf{E}(\mathbf{r}_j) \times \left(\mathbf{P}_j - \frac{e}{c}\mathbf{A}(\mathbf{r}_j)\right) \\ &\quad + \sum_{\mathbf{k}\alpha} \hbar\omega_k \left(c^\dagger_{\mathbf{k}\alpha} c_{\mathbf{k}\alpha} + \frac{1}{2}\right). \end{aligned} \tag{1.2}$$

where $\mathbf{A}(r_j)$ is the vector potential of the x-ray photon field. The first term on the right-hand side, $\sum_j \frac{1}{2m}\left(\mathbf{P}_j - \frac{e}{c}\mathbf{A}(\mathbf{r}_j)\right)^2$, represents the kinetic energy of the electrons. The second term, $\sum_{ij} V(\mathbf{R}_{ij})$, is the electron-electron pair interaction. The third term, $-\frac{e\hbar}{2mc}\sum_j \mathbf{S}_j \cdot \nabla \times \mathbf{A}(\mathbf{r}_j)$, is the interaction of the electrons' spins with the magnetic field of the x-rays. The fourth term, $-\frac{e\hbar}{2(mc)^2}\sum_j \mathbf{S}_j \cdot \mathbf{E}(\mathbf{r}_j) \times \left(\mathbf{P}_j - \frac{e}{c}\mathbf{A}(\mathbf{r}_j)\right)$, is the interaction between the electrons' orbital moments with the x-ray photon field. The last term, $\sum_{\mathbf{k}\alpha} \hbar\omega_k \left(c^\dagger_{\mathbf{k}\alpha} c_{\mathbf{k}\alpha} + \frac{1}{2}\right)$, is the energy of the photon field. The $c^\dagger_{\mathbf{k}\alpha}$ and $c_{\mathbf{k}\alpha}$ are the creation and annihilation operators for a photon with momentum $\mathbf{k}$ and polarization α.

The Cross-section

One quantity in which we are interested in a scattering experiment is called *partial differential cross-section*, $\frac{\partial^2\sigma}{\partial\Omega\partial E_f}$. It is defined as the scattered power per unit solid

angle, per energy band-width, per unit incident flux:

$$\frac{\partial^2\sigma}{\partial\Omega\partial E_f} = \frac{W\rho(E_f)}{I_0} \tag{1.3}$$

where $\rho(E_f)$ is the density of the final state $\mid f >$, I_0 is the incident flux, and W is the probability of the transition from an initial state $\mid i > \equiv \mid a >_s \mid \mathbf{k}, \alpha >_p$ to a final state $\mid f > \equiv \mid b >_s \mid \mathbf{k}', \alpha' >_p$, where the subscripts s and p denote sample and photon respectively. The transition probability W is simply given by Fermi's "Golden Rule":

$$W = \frac{1}{\hbar}\left| < f \mid \mathcal{H} \mid i > + \sum_m \frac{< f \mid \mathcal{H} \mid m >< m \mid \mathcal{H} \mid i >}{E_i - E_m} \right|^2 \delta(E_i - E_f) \tag{1.4}$$

Careful calculations lead to the following scattering cross-section [25], including all terms up to second order.

$$\begin{aligned}\left(\frac{\partial^2\sigma}{\partial\Omega'\partial E'}\right)_{|i>\rightarrow|f>} &= \frac{e^2}{mc^2}\Bigg| < b \mid \sum_j e^{i\mathbf{Q}\cdot\mathbf{r}_j} \mid a > \hat{\epsilon}\cdot\hat{\epsilon}' \\ &\quad -i\frac{\hbar\omega}{mc^2} < b \mid \sum_j e^{i\mathbf{Q}\cdot\mathbf{r}_j}\left(i\frac{(\mathbf{Q}\times\mathbf{P}_j)}{\hbar k^2}\cdot\mathbf{A} + \mathbf{S}_j\cdot\mathbf{B}\right) \mid a > \Bigg|^2 \\ &\quad \times\delta(E_a - E_b + \hbar\omega_k - \hbar\omega_{k'})\end{aligned} \tag{1.5}$$

where $\mathbf{Q} \equiv \mathbf{k}' - \mathbf{k}$ is the momentum transfer, $\hat{\epsilon}$ and $\hat{\epsilon}'$ are the unit polarization vector for the initial and final photon. The vectors $\mathbf{A}$ and $\mathbf{B}$ are defined as:

$$\begin{aligned}\mathbf{A} &= (\hat{\epsilon}'\times\hat{\epsilon}) \\ \mathbf{B} &= (\hat{\epsilon}'\times\hat{\epsilon}) + (\hat{\mathbf{k}}'\times\hat{\epsilon}')(\hat{\mathbf{k}}'\cdot\hat{\epsilon}) - (\hat{\mathbf{k}}\times\hat{\epsilon})(\hat{\mathbf{k}}\cdot\hat{\epsilon}') + (\hat{\mathbf{k}}'\times\hat{\epsilon}')\times(\hat{\mathbf{k}}\times\hat{\epsilon})\end{aligned} \tag{1.6}$$

where $\hat{\mathbf{k}}$ and $\hat{\mathbf{k}}'$ are the unit momentum vector for the initial and final photon.

The cross-section indeed has contributions from both the charge scattering and the magnetic scattering. However the contribution from the magnetic scattering is a factor of $\left(\frac{\hbar\omega}{mc^2}\right)^2$ smaller than that from the charge scattering. The contribution from the magnetic scattering is further reduced by the fact that only unpaired electrons contribute to the magnetic scattering process. Specifically, the number of the

electrons which participate in the magnetic scattering, N_m, is usually an order of magnitude smaller than the number of those which participate in the charge scattering, N (all electrons). The ratio of the magnetic contribution to the charge contribution is therefore:

$$\frac{\sigma_{mag}}{\sigma_{charge}} \sim \left(\frac{\hbar\omega}{mc^2}\right)^2 \left(\frac{N_m}{N}\right)^2 \tag{1.7}$$

For 10KeV photons this factor is 2.5×10^{-7} [25]! It would be hopeless to try to detect a magnetic signal of 1 on top of a monstrous charge signal of 4×10^6. Fortunately, in some magnetic systems, such as antiferromagnets, the magnetic structure has a periodicity different from that of the atomic structure, one therefore can find positions in the reciprocal space at which the coherent charge scattering is zero. In addition, the high fluxes available at the synchrotron sources have helped to transform magnetic x-ray scattering from an academic curiosity [26, 27, 28] to a powerful everyday tool [29] in studying magnetic materials.

Due to the strong coupling of the neutron spin to the magnetic moments in the sample, magnetic neutron scattering has played an eminent role in the studies of magnetic materials since the techniques were first developed by Clifford G. Shull and Bertram N. Brockhouse, for which the two were awarded the 1994 Nobel Prize in Physics. One may then ask what the advantages are in using synchrotron x-rays scattering techniques to study the magnetic properties. The most significant benefit of using x-rays to probe the magnetic properties on an atomic scale lies in the fact that they provide high wave-vector resolution and are therefore sensitive to even slight magnetic structure distortions — the very same characteristic makes x-ray scattering an unsurpassed tool in studying the geometric arrangements of atoms and molecules. The importance of this advantage will be exemplified in the studies reported in this thesis. In addition, the x-ray beam polarization and energy can be chosen to meet the requirements of a specific experiment. In particular, the scattered radiation by spins and orbital momenta leave different signatures [25], which makes it possible to learn about the spin and orbital contributions to a sample's magnetic moment.

Free of extinction effects, magnetic x-ray scattering is also the best technique for studying the details of the magnetic ordering as the temperature is varied near the critical temperature. Finally, small samples can be studied using x-rays while neutron experiments usually require relatively large samples.

Part I

Spin-Peierls Transition in $CuGeO_3$

The cooperative behavior of lower dimensional quantum spin systems is a subject of continuing research. One particularly interesting phenomenon is the so-called spin-Peierls transition, which is a structural phase transition driven by the magnetic interaction in one dimensional (1D) S = $\frac{1}{2}$ chain compounds. By analogy with the well-known Peierls instability in a 1D metal [22], it can be shown [30, 31] that a uniform antiferromagnetic chain is unstable with respect to a lattice distortion which dimerizes the chain into an alternating antiferromagnet; thereby introducing a gap into the chain spin excitation spectrum.

Until about two years ago, spin-Peierls transitions had only been observed in a few organic compounds such as TTF-$CuS_4C_4(CF_3)_4$ [32, 33] and (MEM)-$(TCNQ)_2$ [34]. However, because of size and crystal quality limitations, information on the static and dynamic spin and lattice fluctuations associated with the spin-Peierls transition in these materials was quite limited. Thus, many essential features of the transition are not yet characterized or understood. Much more complete experimental work on the spin-Peierls transition has been made possible by the discovery that a structurally simple, inorganic chain compound, copper germanate ($CuGeO_3$), exhibits the behaviors predicted for a spin-Peierls system.

In the first half of this thesis, we report a detailed synchrotron x-ray study of the phase behavior at the spin-Peierls transition in $CuGeO_3$. The organization of this Part is as follows. In Chapter 2, we summarize the theoretical understandings of the spin-Peierls transition. In Chapter 3, we measure the temperature dependence of the superlattice reflections, resulting from the lattice dimerization. In Chapter 4, we report the observation of a concomitant thermal contraction below the spin-Peierls transition temperature in $CuGeO_3$. Finally in Chapter 5, we report the observation of large length scale fluctuations at the spin-Peierls transition in $CuGeO_3$ for temperatures above the transition temperature.

Chapter 2

The Spin-Peierls Transition

2.1 What is the Spin-Peierls Transition?

Consider a system which consists of an assembly of uniform quantum spin chains described by a spin-$\frac{1}{2}$ Heisenberg or XY, for reasons which we will explore in next section, Hamiltonian with nearest-neighbor-only antiferromagnetic exchange couplings. These chains are stacked parallel to one another, and interchain magnetic couplings are neglected. However, allowance is made for the possibility of an elastic distortion of the lattice, *i. e.* the lattice is soft. Since the exchange energy of the neighboring spins along the chain direction is a function of separation between adjacent lattice sites, an elastic distortion of the lattice will influence the spin hamiltonian of the system. It turns out that for some of such systems, as the temperature is lowered, the uniform spin chain undergoes a transition at a finite critical temperature T_{sp} to a dimerized state, which is a state in which the neighboring pairs of ions are displaced a small amount from their "uniform positions", alternately closer and further apart. We call this magnetoelastic transition *spin-Peierls transition* for its similarities to the Peierls transition in a quasi-one-dimensional metal [22]; and the systems that undergo the spin-Peierls transition are referred to as *spin-Peierls systems.*

To understand why the dimerized state is energetically favored at low temperatures for spin-Peierls systems, we first examine the excitation spectrum for both a uniform and a dimerized chain as well as the effects of quantum fluctuations.

2.2 Excitation Spectra and the Role of Quantum Fluctuations

The excitation spectrum [35] for a uniform infinite one-dimensional antiferromagnet Heisenberg chain is depicted in the left panel of Fig. 2-1. The salient point is that the excitation spectrum is degenerate with the ground state at $q = 0, \pm\pi/a$. This degeneracy brings excited states infinitely close to the ground state (of which the Néel state is a component). Therefore, quantum zero-point fluctuations of the chain will populate the low-lying excited states. This implies that the state at $T = 0$K is a composite of the singlet ground state and triplet excited states. The consequences are that the Néel state is not a true eigenstate of the Hamiltonian, and there is no long-range order at $T = 0$K. If the chain is dimerized, a gap develops in the excitation spectrum which lifts the above-mentioned degeneracy of the ground and excited states (see the right panel of Fig. 2-1). The zero-point fluctuations can now no longer populate the excited states, and the net magnetic energy is lowered. However, this lowering of magnetic energy is countered by the increase of the elastic energy due to the distortion of the lattice.

We emphasize that the spin-Peierls transition results from an inherent instability of a quantum Heisenberg or XY chain. An Ising or classical antiferromagnetic chain can not show the spin-Peierls effect. This is because an Ising chain effectively has an energy gap between the ground and excited states. A classical chain has no zero-point energy, and therefore its magnetic energy is independent of chain dimerization. Also, the spin-Peierls transition can only occur in quantum magnetic chain systems with S being half-interger. This is because in contrast to half-integer spin chains, integer spin chains have a gap — Haldane gap — in the excitation spectrum. Furthermore, quantum fluctuations decrease rapidly as S increases, so one would therefore expect spin-Peierls transition more likely to occur in systems with S=$\frac{1}{2}$. A spin-Peierls transition is such that its onset precludes the establishment of magnetic order at lower temperature; *i. e.*, the spin excitations remain paramagnetic down to $T = 0$K. The order parameter is therefore given by the degree of the lattice distortion δ, or

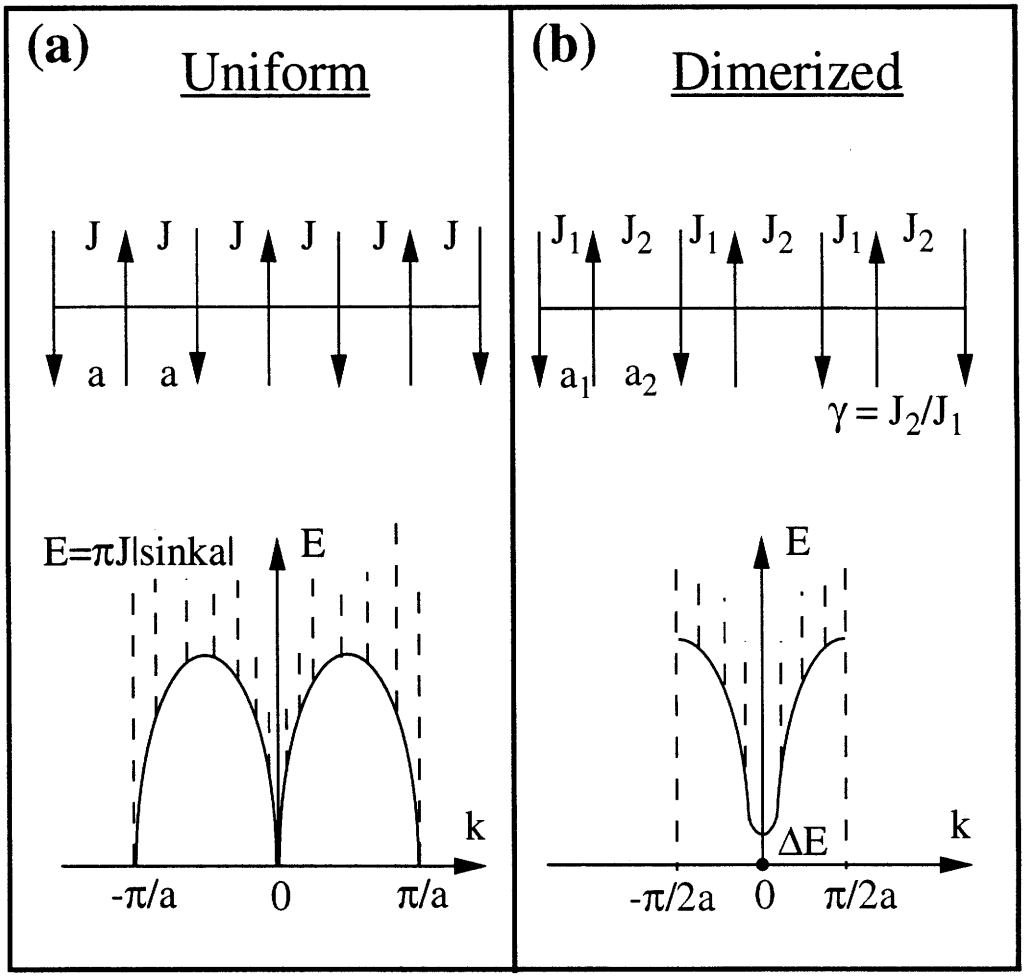

Figure 2-1: Schematic representation of the elementary excitations versus wave vector for a uniform Heisenberg antiferromagnet chain(a) and an alternating chain(b). In (b), the dot at k=0 indicates the ground state. Also notice that the unit cell is doubled in an alternating chain.

equivalently the magnitude of the magnetic gap Δ.

In order for the spin-Peierls transition to occur, the decrease of the magnetic energy produced by a lattice dimerization must outweigh the increase of the elastic energy due to the lattice distortion. In the following section, we will show that this is indeed the case in the spin-Peierls systems.

2.3 Formulation of the Problem and Some Theoretical Results

2.3.1 Hamiltonian

The Hamiltonian for nearest-neighbor-coupling-only spins with antiferromagnetic interactions on a rigid lattice is simply:

$$\mathcal{H}_s = \sum_j J(j, j+1)(\mathbf{S}_j \cdot \mathbf{S}_{j+1}) \tag{2.1}$$

where $J > 0$, and the sum over lattice sites j includes nearest intrachain neighbors only. Now, if we assume that the exchange integral J depends on the instantaneous positions of the magnetic ions, and that the lattice is soft *i. e.* the lattice is allowed to distort, an elastic distortion can influence the spin hamiltonian $\mathcal{H}_s$. This effect represents the spin-phonon (or spin-lattice) coupling. In addition, as we pointed out earlier, in spin-Peierls systems the decrease of the magnetic energy is countered by an increase in the elastic energy due to the lattice distortion. This elastic energy can be written as $\sum_{\mathbf{q}\alpha} \omega_0(\mathbf{q}\alpha) b^\dagger_{\mathbf{q}\alpha} b_{\mathbf{q}\alpha}$, where $b^\dagger_{\mathbf{q}\alpha}(b_{\mathbf{q}\alpha})$ is the creation (destruction) operator for three-dimensional phonons with wave-vector $\mathbf{q}$ on branch α, and ω_0 is the phonon energy. The Hamiltonian for a model spin-Peierls system may therefore be written as

$$\mathcal{H} = \sum_j J(j, j+1)(\mathbf{S}_j \cdot \mathbf{S}_{j+1}) + \sum_{\mathbf{q}\alpha} \omega_0(\mathbf{q}\alpha) b^\dagger_{\mathbf{q}\alpha} b_{\mathbf{q}\alpha}. \tag{2.2}$$

Since the exchange constant $J(j, j+1)$ is a function of the *three-dimensional* spatial separation of sites j and $j+1$, the one-dimensional spin interactions depend on the three-dimensional motion of the lattice sites. Thus we are treating a one-dimensional magnetic system coupled to a three-dimensional phonon system. The treatment presented here largely follows Ref. [36].

2.3.2 Jordan-Wigner Transformation

The most common method [31, 37] of tackling Eq. 2.2 is to first convert the spin operators to pseudofermion operators via the Jordan-Wigner transformation [38]. In the pseudofermion representations [39, 40], a site with spin-down is said to have a pseudofermion and a site with spin-up is said to be empty.

Following Ref. [37], we will describe the spin system by the fermion operators

$$\Psi_j = (-2)^{j-1} S_1^z S_2^z \cdots S_j^- \tag{2.3}$$

where

$$S^{\pm} = S^x \pm i S^y.$$

In terms of these operators, we have

$$\begin{aligned} \{\Psi_j, \Psi_{j'}^\dagger\} &= \delta_{jj'} \\ S_j^+ S_{j+1}^- &= \Psi_j^\dagger \Psi_{j+1} \\ S_j^z &= \frac{1}{2} - \Psi_j^\dagger \Psi_j. \end{aligned} \tag{2.4}$$

Making use of Eq. 2.3 and Eq. 2.4, Eq. 2.2 becomes

$$\begin{aligned} H &= \sum_j \frac{1}{2} J(j, j+1)[\Psi_j^\dagger \Psi_{j+1} + \Psi_{j+1}^\dagger \Psi_j - 2\Psi_j^\dagger \Psi_j + 2\Psi_j^\dagger \Psi_j \Psi_{j+1}^\dagger \Psi_{j+1} + \frac{1}{2}] \\ &\quad + \sum_{\mathbf{q}\alpha} \omega_0(\mathbf{q}\alpha) b_{\mathbf{q}\alpha}^\dagger b_{\mathbf{q}\alpha}. \end{aligned} \tag{2.5}$$

In the above and the following equations, three-dimensional vectors are boldface and wave vectors along the chain direction are italic.

Since Eq. 2.5 can not be solved exactly, various approximations have to be employed.

2.3.3 Linearization of $J(j, j+1)$

One important approximation involves the treatment of the separation dependence of J. By far the most common approach is to expand $J(j, j+1)$ only to first order in inter-site spacing, thereby obtaining a spin-phonon coupling term [37].

$$J(j, j+1) = J + \sum_j [\mathbf{u}(j) - \mathbf{u}(j+1)] \cdot \nabla_j J(j, j+1) + \cdots \tag{2.6}$$

Here the $\mathbf{u}$ are the lattice displacement operators in three dimensions. It is important to notice that the phonons are three-dimensional, because the one-dimensional spin system by itself can not undergo a phase transition at a non-zero temperature [21]. The treatment of this three-dimensionality is therefore crucial to the ultimate transition. This has been discussed in detail by Cross and Fisher [31]. An exact treatment of the three-dimensional lattice is impossible, and most theoretical work has used methods such as the Hartree-Fock approximation or the random phase approximation, which effectively treated the chains as decoupled. However, the three-dimensional nature of the phonons is implicitly used to suppress the one-dimensional fluctuations of a single chain, which as noted above otherwise would preclude a phase transition at non-zero temperature.

The lattice displacement operator $\mathbf{u}$ and the phonon operators $b_{\mathbf{q}\alpha}$, $b^\dagger_{\mathbf{q}\alpha}$ are connected through the following:

$$\mathbf{u}(j) = (mN)^{-1/2} \sum_{\mathbf{q}\alpha} \mathbf{e}(\mathbf{q}\alpha) e^{i\mathbf{q}\cdot\mathbf{R}_j} Q(\mathbf{q}\alpha) \tag{2.7}$$

where

$$Q(\mathbf{q}\alpha) = [2\omega_0(\mathbf{q}\alpha)]^{-1/2}(b_{\mathbf{q}\alpha} + b^\dagger_{-\mathbf{q}\alpha})$$

and where $\mathbf{e}(\mathbf{q}\alpha)$ is the phonon polarization vector, m is the mass of the magnetic site, and N is the number of chain sites.

Combining Eq. 2.6, Eq. 2.7 and $\Psi_k = N^{-1/2}\sum_j e^{ikj}\Psi_j$, we have [37]:

$$\begin{aligned}
\mathcal{H} &= \sum \varepsilon_k \Psi^\dagger_k \Psi_k + N^{-1} \sum_{k_1+k_2=k_3+k_4} v(k_2-k_3)\Psi^\dagger_{k_1}\Psi^\dagger_{k_2}\Psi_{k_3}\Psi_{k_4} \\
&+N^{-1/2}\sum_{k\mathbf{q}\alpha} g_1(k\mathbf{q}\alpha)\Psi^\dagger_k\Psi_{k-\mathbf{q}}(b_{\mathbf{q}\alpha} + b^\dagger_{-\mathbf{q}\alpha}) \\
&+N^{-1} \sum_{k_1+k_2=k_3+k_4-q} g_2(k_2-k_3,\mathbf{q}\alpha)\Psi^\dagger_{k_1}\Psi^\dagger_{k_2}\Psi_{k_3}\Psi_{k_4}(b_{\mathbf{q}\alpha} + b^\dagger_{-\mathbf{q}\alpha}) \\
&+\sum \omega_0(\mathbf{q}\alpha) b^\dagger_{\mathbf{q}\alpha} b_{\mathbf{q}\alpha}
\end{aligned} \tag{2.8}$$

where

$$\begin{aligned}
\varepsilon_k &= J(\cos ka - 1) \\
v(k) &= J\cos ka \\
g_1(k\mathbf{q}\alpha) &= \frac{1}{2}g(\mathbf{q}\alpha)(1-e^{-iq\alpha})(e^{ika}-1)(1-e^{i(q-k)a}) \\
g_2(k\mathbf{q}\alpha) &= g(\mathbf{q}\alpha)e^{ika}(1-e^{-iq\alpha}) \\
g(\mathbf{q}\alpha) &= [2m\omega_0(\mathbf{q}\alpha)]^{-1/2}\mathbf{e}(\mathbf{q}\alpha)\cdot\nabla J(j,j+1).
\end{aligned}$$

Eq. 2.8 is exact except for the linearization of $J(j, j+1)$.

2.3.4 Hartree-Fock Approximation

To proceed from Eq. 2.8, earlier work by Pytte [37] and Bulaevskii [41] treated the four-fermion terms in Eq. 2.8 in the Hartree-Fock approximation to reduce Eq. 2.8 to the same form as that used to describe the conventional Peierls transition.

Specifically, all four-fermion terms can be converted to two-fermion terms through:

$$< \Psi_k^\dagger \Psi_q >= n_k \delta_{kq} \tag{2.9}$$

where $n_k = [\exp(\beta E_k)+1]^{-1}$ ($\beta \equiv 1/k_B T$), and the average is taken in the undistorted state. Eq. 2.8 thus becomes [37]

$$\mathcal{H} = \sum_k E_k \Psi_k^\dagger \Psi_k + \sum g(k\mathbf{q}\alpha)\Psi_k^\dagger \Psi_{k-q}(b_{\mathbf{q}\alpha} + b_{-\mathbf{q}\alpha}^\dagger) + \sum \omega_0(\mathbf{q}\alpha) b_{\mathbf{q}\alpha}^\dagger b_{\mathbf{q}\alpha} \tag{2.10}$$

where

$$\begin{aligned} E_k &\equiv pJ\cos ka \\ g(k\mathbf{q}\alpha) &= ipg(\mathbf{q}\alpha)\{\sin ka - \sin[(k-q)a]\} \\ p &= 1 - 2N^{-1}\sum_k n_k \cos ka. \end{aligned}$$

The renormalization factor p is approximately constant $p = 1.64$ for temperatures $T \ll J$.

2.3.5 Random-phase Approximation (RPA)

Similar to the Fröhlich Hamiltonian used to model the conventional Peierls transition [42], the pseudofermion-phonon interactions in Eq. 2.10 are treated by appling the random-phase approximation (RPA). The random-phase approximation, like any other mean-field approach, neglects the effects of fluctuations. While it is well known that mean-field approach is a poor approximation for lower dimensional systems, the use of the RPA here may, however, be justified by the fact that the phonons are three-dimensional. In particular, in systems, such as (TTF)(CuBDT), the three-dimensional softening of the phonon leading to the phase transition persists to much higher temperatures than expected [34].

We then obtain the dispersion curve for the renormalized phonon in the undis-

torted lattice:

$$\omega^2 = \omega_0^2(\mathbf{q}\alpha) + \frac{1}{N}\sum g(k\mathbf{q}\alpha)\frac{g(k-q,\mathbf{q}\alpha)n_k - g^*(k\mathbf{q}\alpha)n_{k-q}}{\omega - E_{k-q} + E_k} \tag{2.11}$$

where $\omega_0(\mathbf{q}\alpha)$ is the phonon frequency in the absence of the spin interactions. Eq. 2.11, at $q = \pi/a$ and near T_{sp}, leads to:

$$\omega^2 = \omega_0^2(T/T_{sp} - 1)/\ln(0.83pJ/T_{sp}). \tag{2.12}$$

At T_{sp}, $\omega(q = 2k_F) = 0$, where $k_F = \pi/2a$ is the Fermi wave vector. This leads to the gap equation:

$$\omega_0^2(\mathbf{q}, q = 2k_F) = \frac{g^2}{J^2}\frac{2}{\pi}\int_{-Jp}^{Jp} dE \frac{[(Jp)^2 - E^2]^{1/2}}{E}\tanh\left(\frac{1}{2}\beta_c E\right). \tag{2.13}$$

In the limit, $T_{sp} \ll pJ$, *i.e.* the weak-coupling assumption, the expression for the transition temperature is of the Bardeen-Cooper-Schrieffer (BCS) form [43]:

$$T_{sp} = 0.83pJe^{-1/\lambda} \tag{2.14}$$

where

$$\begin{aligned} \lambda &\equiv 4g^2p/\omega_0^2\pi J \\ g &\equiv g(\alpha\mathbf{q}, q = 2k_F) \\ \omega_0 &\equiv \omega_0(\alpha\mathbf{q}, q = 2k_F). \end{aligned}$$

2.3.6 Dimerization

Some authors [30, 44, 45] have elected to begin with a different Hamiltonian:

$$\mathcal{H}' = \sum_j (J_1\mathbf{S}_{j,1}\cdot\mathbf{S}_{j,2} + J_2\mathbf{S}_{j,2}\cdot\mathbf{S}_{j+1,2}) + \sum_{\mathbf{q}\alpha}\omega_0(\mathbf{q}\alpha)b^+_{\mathbf{q}\alpha}b_{\mathbf{q}\alpha} \tag{2.15}$$

where J_1 and J_2 are intra- and inter-dimer exchange couplings and j labels the dimer. It is easy to see that the dimerization is built into this Hamiltonian. Since Eq. 2.15 and Eq. 2.2 represent the same physical system, specifically, $J_1 = J_2 = J(j, j+1)$ at $T = T_{sp}$, their proper solution should give identical results. The problem is that for the mean-field approximation most often used, their solutions are not the same. Fortunately, they are not wildly different.

Below T_{sp}, the lattice is dimerized and two unequal and alternating J's are produced. If we again assume the J is linearly dependent on the inter-site separations, we have:

$$\begin{aligned} J_1 &= J(1+\eta\delta) \\ J_2 &= J(1-\eta\delta) \end{aligned} \tag{2.16}$$

where δ is the distortion magnitude. It then follows [37] that if the phonon normal mode coordinate is replaced by its thermal average

$$Q(\lambda \mathbf{q}) =< Q > \delta_{q,2k_F} \tag{2.17}$$

then

$$\delta = (2g/J) < Q > . \tag{2.18}$$

Furthermore, the gap energy Δ scales like the dimerization δ:

$$\Delta(T) = pJ\delta(T), \tag{2.19}$$

and the ground-state magnetic energy E_0 at $T = 0$K as a functions of dimerization δ is found to be:

$$E_0 \propto -\delta^2 \ln^2 \delta. \tag{2.20}$$

The cost in lattice energy is proportional to δ^2. Therefore, the energy difference

between the uniform chain and the dimerized chain is:

$$\Delta E \sim A\delta^2 - \delta^2 \ln^2 \delta. \tag{2.21}$$

Hence for very small δ, $\Delta E < 0$, the dimerized state is energetically favored.

2.3.7 Beyond The Hartree-Fock Approximation

While the random phase approximation in treating spin-phonon coupling may be justified by the three-dimensional nature of the phonons, it is difficult to justify the use of Hartree-Fock approximation, which is also mean-field, in treating the four-fermion terms. Cross and Fisher [31] therefore went beyond the mean-field approach to give a better account of the effects of the interaction terms. Specifically, the Cross-Fisher treatment takes advantage of the close similarity between the pseudofermion representation and the exactly soluble [46] Luttinger-Tomonaga model [47, 48]. The basic idea is that responses that are divergent can be approximately calculated by modeling the Hamiltonian with a soluble form that maintains the essential features in the region near the Fermi surface which lead to the divergence. Within this model the four-fermion interactions can be exactly included, and no perturbation expansion is needed [31]. It should be noted here that although Cross-Fisher treatment is non-perturbative, it is still approximate in treating the four-fermion interaction terms.

In general, the Cross-Fisher results support the approximate accuracy of thermodynamic properties calculated in the mean-field approach. However, there are some notable difference in their solutions. For T_{sp}, they obtain a linear functional dependence on λ [31] (cf. Eq. 2.14):

$$T_{sp} = 0.8J\lambda_{CF} \tag{2.22}$$

where $\lambda_{CF} \equiv \lambda/p = 4g^2/\pi J\omega_0^2$. Also, they find an increase of the rate of phonon

softening above T_{sp} (cf. Eq. 2.12):

$$\omega^2(2k_F, T) = \omega_0^2(T/T_{sp} - 1). \tag{2.23}$$

They find that the mean-field order parameter should be scaled by a factor $(T_{sp}/J)^{1/2}$, and that the lattice distortion for a given λ and T/T_{sp} is reduced from the mean-field result by the factor $(T_{sp}/J)^{1/2}$.

Finally, they find that at $T = 0$K the dependence of the ground-state magnetic energy of the spin system E_0 and the excitation gap Δ on the distortion parameter δ are (cf. Eq. 2.19 and Eq. 2.20)

$$\begin{aligned} E_0 &\propto -\delta^{4/3} \\ \Delta &\propto \delta^{2/3}. \end{aligned} \tag{2.24}$$

This result is very close to that of Duffy and Barr [49], which was derived by extrapolation from numerical calculations of finite dimerized chains.

2.4 Field Dependence of Spin-Peierls Transition

Since the spin-Peierls transition is a magnetically driven transition, one expects magnetic fields to have interesting effects on the transition. This is indeed the case. For instance, very large magnetic fields may have drastic effects: when H is larger than a critical field, H_c, it may force all spins to align along the field direction. However, this is trivial, and not the case that interests us. The interesting limit is $H \leq H_c$, and this is the situation we are concerned with here.

The magnetic field H couples to the system via a Zeeman term:

$$H_M = -\tilde{g}\mu_B H \sum_j S_j^z \tag{2.25}$$

where $\tilde{g}$ is the gyromagnetic ratio, and μ_B is the Bohr magneton. This Zeeman energy term must be added to the Hamiltonian, Eq. 2.2 (or Eq. 2.15). It turns out that the

addition of the Zeeman term to Eq. 2.10 merely modifies ε_k:

$$\varepsilon_k = J(\cos ka - 1 - h) \tag{2.26}$$

where $h \equiv 2\mu_B H/J$.

Mean-field results

Within the mean-field approximation, the Zeeman energy manifests itself in the modification of the Fermi wave vector:

$$k_F(0) - k_F(H) = 1.44\mu_B H/pJa \quad \text{for} \quad \mu_B H \ll J. \tag{2.27}$$

The magnetic energy now has its minimum at a different wave vector $2k_F(H)$. However, the lattice Umklapp energy associated with the reciprocal lattice vector $Q = \pi/a = 2k_F(0)$ causes the lattice to distort at π/a until H becomes large enough for the reduction in magnetic energy to exceed the Umklapp energy. This Umklapp energy is also called the commensurability energy, and is present for all values of $2k_F(H)$ that are commensurate with the lattice. In the regime of small H where the distortion wave vector q is fixed at π/a, $T_{sp}(H)$ is determined by [50, 51]:

$$\ln(T_{sp}(H)/T_{sp}(0)) + Re[\Psi(\frac{1}{2} + i\mu(H)/2\pi T_{sp}(H)) - \Psi(\frac{1}{2})] = 0 \tag{2.28}$$

where for $\mu_B H \ll J$, the Fermi level $\mu(H) \simeq -1.44\mu_B H$. Ψ is the digamma function. For small $\mu_B H/k_B T_{sp}(0)$, one obtains the following expansion [50, 51]:

$$T_{sp}(H) = T_{sp}(0)(1 - \alpha_2(\frac{g\mu_B H}{2k_B T_c(0)})^2 - \alpha_4(\frac{g\mu_B H}{2k_B T_c(0)})^4), \tag{2.29}$$

where $\alpha_2 = 0.44$, and $\alpha_4 = 0.2$.

Beyond the mean-field approximation

Cross [52] went beyond the mean-field approach by using the boson algebra approach

[31], and obtained the following results (cf. Eq. 2.27 and Eq. 2.29):

$$k_F(0) - k_F(H) = 1.27\mu_B H/Ja \tag{2.30}$$

$$T_{sp}(H) = T_{sp}(0)(1 - \alpha_2'(\frac{g\mu_B H}{2k_B T_c(0)})^2) \tag{2.31}$$

where $\alpha_2' = 0.36$. These results are qualitatively the same as the mean-field results, with some quantitative differences.

We see from both Eq. 2.29 and Eq. 2.31 that in a spin-Peierls system, $T_{sp}(H)$ is a monotonically decreasing function of H. This is consistent with the role of the magnetic field and quantum fluctuations. The effect of H is effectively to decrease the number of the spin components by one. Magnetic quantum fluctuations decrease as the spin-dimensionality (n) decreases. But as discussed in earlier sections, in a spin-Peierls system it is the quantum spin fluctuations that provide the driving force for the transition. Since H reduces these fluctuations, it therefore reduces the energy available to form the spin-Peierls phase. This effect and the Zeeman energy effect, which also reduces the transition temperature, combine to depress the transition temperature $T_{sp}(H)$.

When H exceeds a critical value H_c, q rapidly moves away from π/a either to $2k_F(H)$ — commensurate-incommensurate (C-I) transition, or to some new commensurate values where it stays for some range of H — commensurate-commensurate (C-C) transition. The details can depend on the actual phonon spectrum of the system concerned. Direct observation of a magnetic field induced commensurate to incommensurate transition has been reported in x-ray scattering studies of the organic and inorganic (*i.e.* $CuGeO_3$) spin-Peierls systems in magnetic fields [53, 54].

2.5 Pre-$CuGeO_3$ Spin-Peierls Systems

The spin-Peierls transition was predicted theoretically in the 1960s [55, 56, 57]. However, the first clear-cut experimental realization was not discovered until 1975 [32, 33]. The discovery was first made in the organic compounds (TTF)(MBDT) where M is a

metal atom such as Cu, Au or Pt. Later, another organic compound $MEM(TCNQ)_2$ [58] was also found to undergo the spin-Peierls transition. Most theoretical work on the spin-Peierls transition is built around and tested against the experimental results in these organic systems.

The spin-Peierls transition in these organic systems exhibits quite mean-field-like behavior [32, 33, 34, 58]. This is thought to be the direct consequence of one important feature shared by these systems: the existence of a precursive three-dimensional softening of the phonon corresponding to the dimerization wave vector ($2k_F$), which reduces the phonon frequency to about an order of magnitude below its usual value. Actually, the occurrence of the spin-Peierls transition in these organic systems is generally attributed to this pre-existing soft mode, *i.e.* the spin-phonon coupling wins the battle with regular magnetic ordering. The three-dimensional, rather than one-dimensional, character of the soft phonon, which corresponds essentially to lattice planes perpendicular to the chains moving in unison [31], goes a long way toward validating a mean-field approach to the problem [31, 32], which, as noted above, is the foundation of most theoretical treatments.

Chapter 3

The Spin-Peierls Transition in $CuGeO_3$

3.1 $CuGeO_3$

The crystal structure of $CuGeO_3$ is orthorhombic, space group $P_{bmm}(D^5_{2h})$, with a unit cell (Fig. 3-1(a)) of dimensions a = 4.81 Å, b = 8.47 Å, and c = 2.94 Å at room temperature [59, 60]. There are two molecules in a unit cell, with the atoms occupying the following positions [59, 60]:

		x	y	z
Cu	in 2(d): with	$\frac{1}{2}$	0	0
Ge	in 2(e): with	0.0743(8)	$\frac{1}{4}$	$\frac{1}{2}$
O(1)	in 2(f): with	0.870(6)	$\frac{1}{4}$	0
O(2)	in 4(i): with	0.281(4)	0.084(2)	$\frac{1}{2}$.

In $CuGeO_3$, each Ge^{2+} is tetrahedrally coordinated to four oxygens, and each distorted tetrahedron shares oxygens at the corners with two other tetrahedra to form a [GeO_3] chain along the c axis. The Cu^{2+} ion, which carries a spin $S = \frac{1}{2}$, is octahedrally coordinated to the neighboring oxygens, and each distorted octahedron shares edges with two neighboring octahedra (Fig. 3-1 (b)) to form [CuO_4] chain parallel to the [GeO_3] chain. The two chains are linked together through oxygen atoms.

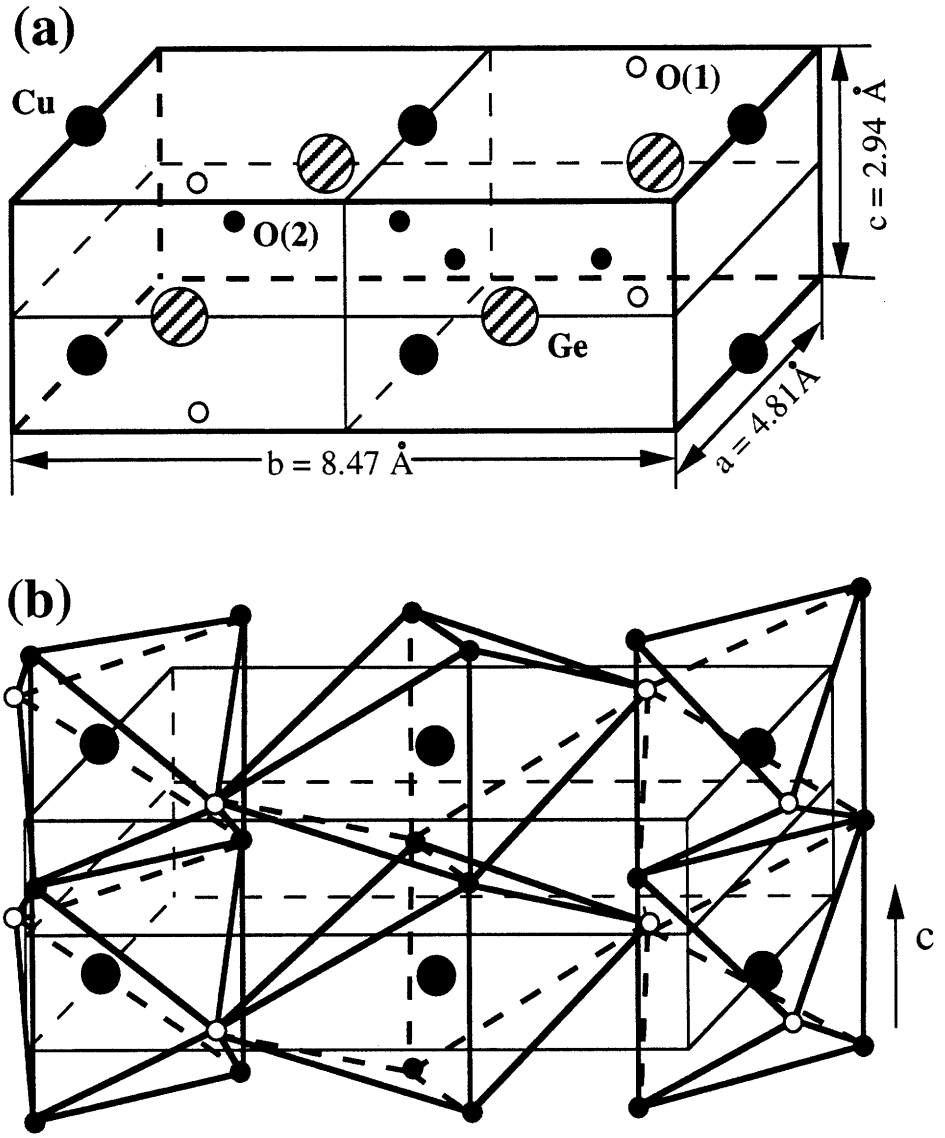

Figure 3-1: (a) The unit cell of $CuGeO_3$; the space group is $P_{bmm}(D^5_{2h})$. The atomic positions are: Cu in $2(d)$ at $\frac{1}{2}$, 0, 0; Ge in $2(e)$ at $x, \frac{1}{4}, \frac{1}{2}(x = 0.0743)$; O(1) in $2(f)$ at $x, \frac{1}{4}, 0(x = 0.870)$ and O(2) in $4(i)$ at $x, y, \frac{1}{2}(x = 0.281, y = 0.084)$. (b) The successive Cu^{2+} $S = \frac{1}{2}$ spins along the c-axis direction are coupled through the superexchange interactions via the bridging oxygen atoms, O(2).

The successive Cu^{2+} $S = \frac{1}{2}$ spins along the c-axis direction are antiferromagnetically coupled through the superexchange interactions via the bridging oxygen atoms. The intrachain and interchain nearest-neighbor exchange parameters are $J_c \approx 10.4$ meV, $J_b \approx 0.1J_c$ and $J_a \approx -0.01J_c$ [61].

Since the first report of magnetic susceptibility measurements by Hase *et al.* [62], $CuGeO_3$ has been found to exhibit the behavior predicted for a spin-Peierls system in several respects. First, Hase *et al.* [62] discovered that the magnetic susceptibilities in all directions drop exponentially to small constant values below a transition temperature (T_{sp}) of 14K. Second, T_{sp} shifts to lower values with increasing magnetic field [63, 62]. Third, Nishi *et al.* [61] confirmed the formation of a gap in the spin excitation spectrum below the transition temperature by using inelastic neutron scattering techniques. Using the same experimental technique, Fujita *et al.* [64] characterized the nature of this gap mode to be triplet by observing the splitting of the gap mode into three distinct modes under the application of a magnetic field. Fourth, the superlattice reflections resulting from the lattice dimerization below the transition temperature have been observed by electron diffraction [65], x-ray and elastic neutron diffraction [63, 66, 67]. Hirota *et al.* [67] mapped out the low temperature dimerized phase in a detailed neutron study. It is found that the dimerization of Cu-Cu pairs along the c-axis direction (Fig. 3-2 (b)) is accompanied by shifts of the bridging oxygen atoms in the a-b plane (Fig. 3-2 (a)), which gives rise to superlattice reflections at the $(\frac{h}{2}\ k\ \frac{l}{2})$ (h, l: odd and k: integer) reciprocal-lattice positions [67]. In this Chapter, we present an x-ray-scattering study of the spin-Peierls transition in $CuGeO_3$.

3.2 Experimental Details

The experiments were carried out on the MIT/IBM beamline X20A at the National Synchrotron Light Source at Brookhaven National Laboratory, interested readers are referred to Ref. [68]. In brief, the white x-ray beam from the bending magnet was focused by a platinum coated, fused quartz mirror and monochromatized by a pair of

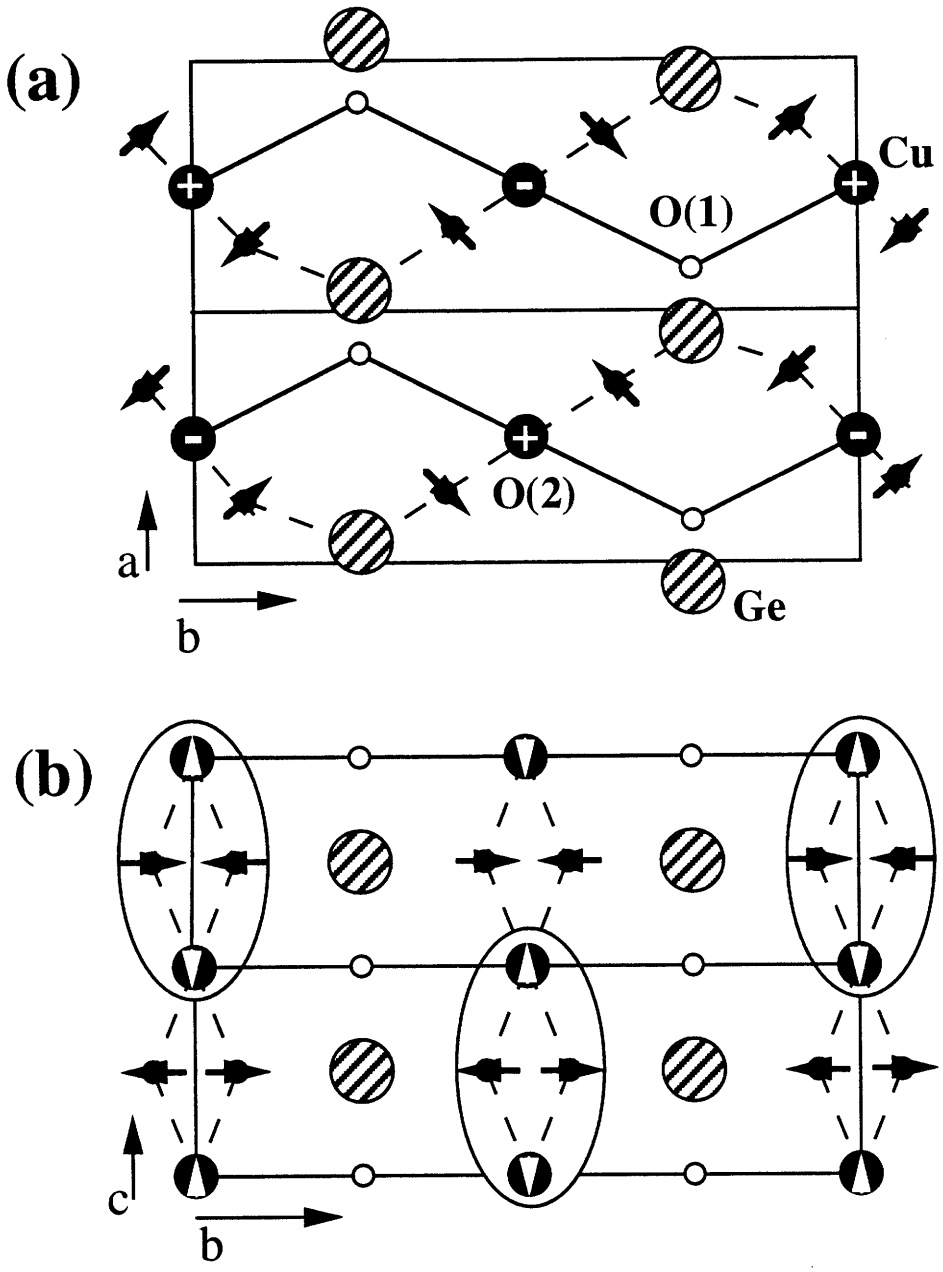

Figure 3-2: The dimerized structure of $CuGeO_3$ below the spin-Peierls transition (T_{sp}). The dimerization of the Cu^{2+} ions along the c-axis(b) is accompanied by the shifts of the bridging oxygen ions in the a-b plane(a).

bounce Ge(111) crystals. The incident photon energy was E = 8.0KeV($\lambda = 1.5498$Å). The scattering occurred in the reflection geometry in the horizontal plane and a flat Ge(111) crystal was used as the analyzer. The two single crystals labeled sample #1 and sample #2 used in the experiments were grown by the floating-zone method. The single crystal of $CuGeO_3$ is translucent, blue in color, and easy to cleave along the a-axis direction. One of the two crystals, sample #2, had a transition temperature of $\sim$ 13.26(3)K, about 1K lower than the more typical value of $\sim$ 14K as reported previously in the literature [62, 65, 66, 67, 69, 70, 71]. Sample #1, on the other hand, had a transition temperature of 14.25(3)K. Both samples showed essentially the same phase behavior and properties. Due to the superior quality of sample #2, which gave higher scattering intensity than sample #1, most of the data presented in this chapter (Chapter 3) and Chapter 5 were taken from sample #2, unless otherwise stated. The samples were mounted with $(h, 0, h)$ and $(0, k, 0)$ in the scattering plane in a split pair superconducting magnet, manufactured by Oxford Instrument, Ltd. Ref. [25] provides a detailed description of the apparatus. The samples were cleaved along the a-axis direction just before being put into the cryostat (within a minute or two). The temperature stability was within 15mK during the course of a scan. The measurements were carried out around the reciprocal-lattice position $(1.5, -1, 1.5)$.

3.3 Spin-Peierls Transition in $CuGeO_3$

Representative scans below the transition temperature along the **H**, **K** and **L** directions through the superlattice reflection $(1.5, -1, 1.5)$ are shown in Fig. 3-3 . Below the transition temperature T_{sp}, the widths of the superlattice peaks are independent of temperature, resolution-limited, and the peak profiles are well described by the functional form:

$$I(\mathbf{q}) = I_0 e^{-(H-H_0)^2/\sigma_H^2} \left[\frac{1}{(K-K_0)^2+\sigma_K^2}\right]^2 e^{-(L-L_0)^2/\sigma_L^2} \qquad (3.1)$$

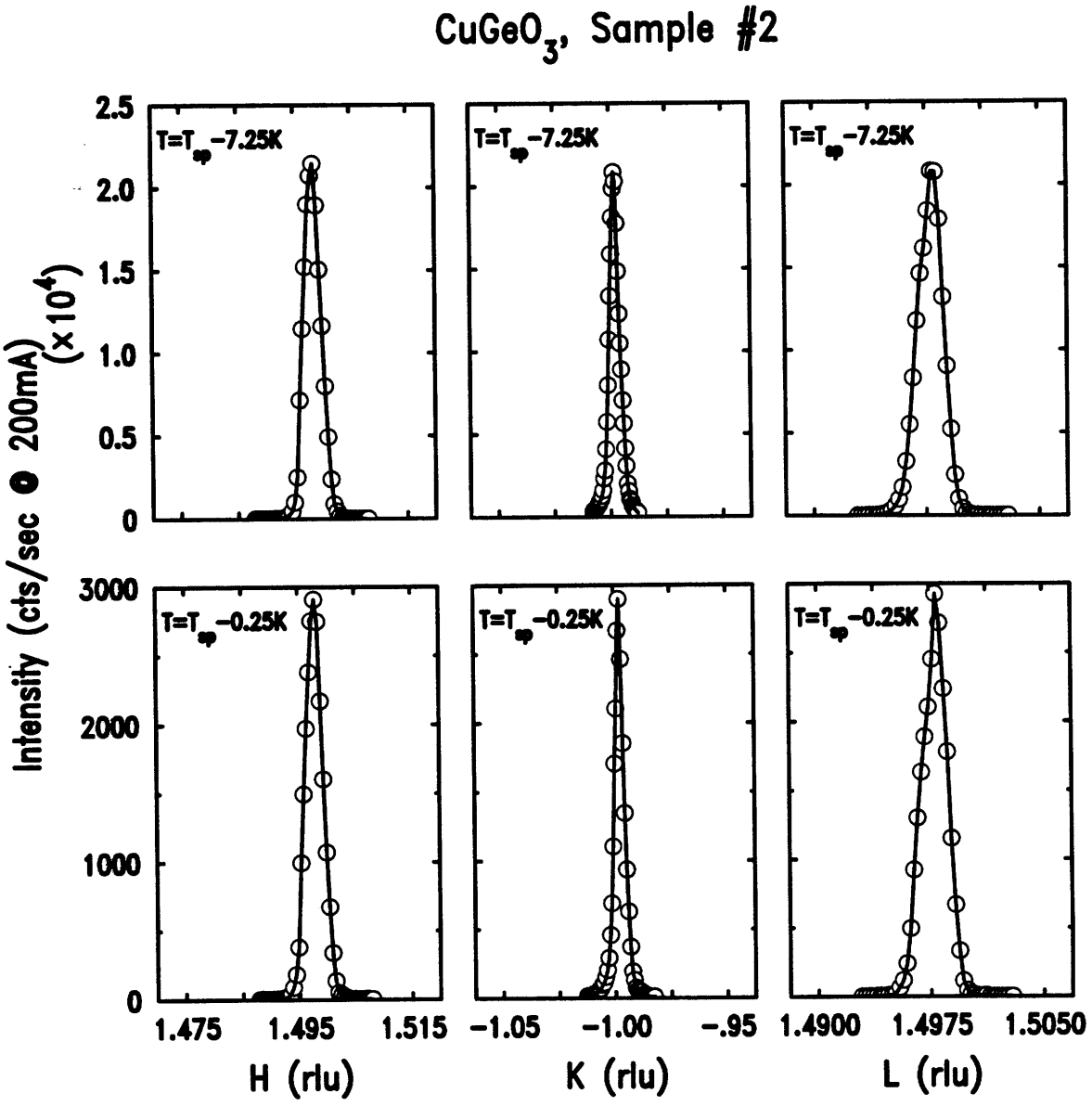

Figure 3-3: Representative scans through the superlattice reflection $(1.5, -1, 1.5)$ below the spin-Peierls transition temperature, T_{sp} for $CuGeO_3$. The solid lines are the results of least-square fits to the data of the resolution function, Eq. 3.1. The count rates are normalized to a ring current of 200 mA.

where (H_0, K_0, L_0) is the superlattice reflection position $(1.5, -1, 1.5)$. Eq. 3.1 is therefore the measured spectrometer resolution function. The half-width-at-half-maxima (HWHM) of the resolution function, that is, $\sqrt{\ln 2}\sigma_H, \sqrt{\sqrt{2}-1}\sigma_K$, and $\sqrt{\ln 2}\sigma_L$, had the values of 0.00242 Å^{-1}, 0.00188 Å^{-1} and 0.00215 Å^{-1} along the **H, K** and **L** directions respectively. The solid lines in Fig. 3-3 are Eq. 3.1 with the above HWHM.

Below the transition temperature, the superlattice peak is resolution limited and its peak intensity, I_0, is therefore proportional to the square of the order parameter, that is, the lattice dimerization, δ, $I_0 \propto \delta^2$. Fig. 3-4 illustrates the peak intensity below the transition temperature as a function of reduced temperature, $t = \left|1 - \frac{T}{T_{sp}}\right|$. Close to the transition temperature, T_{sp}, the peak intensity is well fitted by a simple power law, $I_0 \sim \delta^2 \sim |t|^{2\beta}$. The best fit β value is 0.33(3), in quantitative agreement with the results of neutron scattering measurements [70]. The slight difference between the β value obtained in this work and that reported in Ref. [71] ($\beta = 0.26 \pm 0.03$) results from fitting the data over different temperature ranges. Specifically, only data very close to the transition temperature are included in the fitting in this work whereas a broader range was used in Ref. [71]. This difference in β could indicate a tricritical $\beta = 0.25$ to three-dimensional Ising ($\beta = 0.325$) crossover near T_{sp} [70, 71].

The theory of Cross and Fisher predicts that the spin gap Δ varies as $\delta^{2/3}$ or equivalently $\Delta \sim I^{1/3}$ [31]. We show in Fig. 3-5 the data of Nishi *et al.* [61] for the spin gap together with the power law of Fig. 3-4 raised to the power $\frac{1}{3}$ and the low temperature superlattice intensity data of superlattice reflection $(1.5, -1, 1.5)$ also raised to the power $\frac{1}{3}$. These different sets of data are normalized at 8K. Clearly the agreement is quite satisfactory given the combined uncertainties. Thus once more we see the consistency between the theory for the spin-Peierls transition and the experimental data of $CuGeO_3$. The small gap exponent of 0.093 suggested in the paper of Nishi *et al.* [61] is the result of fitting the gap data far away from the transition temperature to a power law. Clearly, in order to draw a definitive conclusion on the scaling of the spin gap with the atomic displacements, additional data on the gap energy, especially close to the transition temperature, are needed.

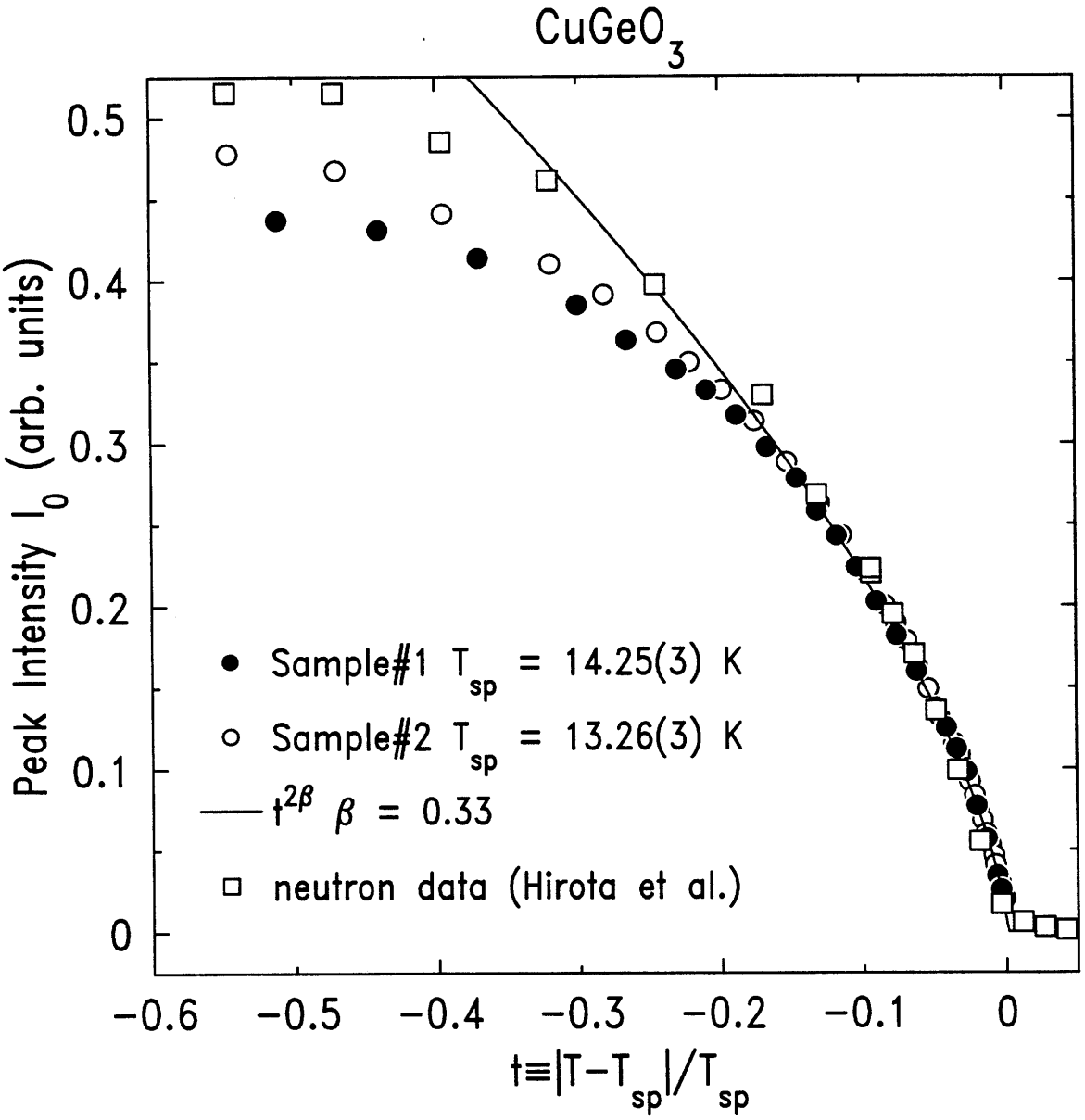

Figure 3-4: The order parameter squared as a function of the reduced temperature. The empty circles are data taken from Sample#1, the filled circles are data taken from Sample#2, the empty squares are neutron data from Hirota *et al.* and the solid line represents a simple power law, $\delta^2 \sim t^{0.66}$ where δ is the lattice dimerization.

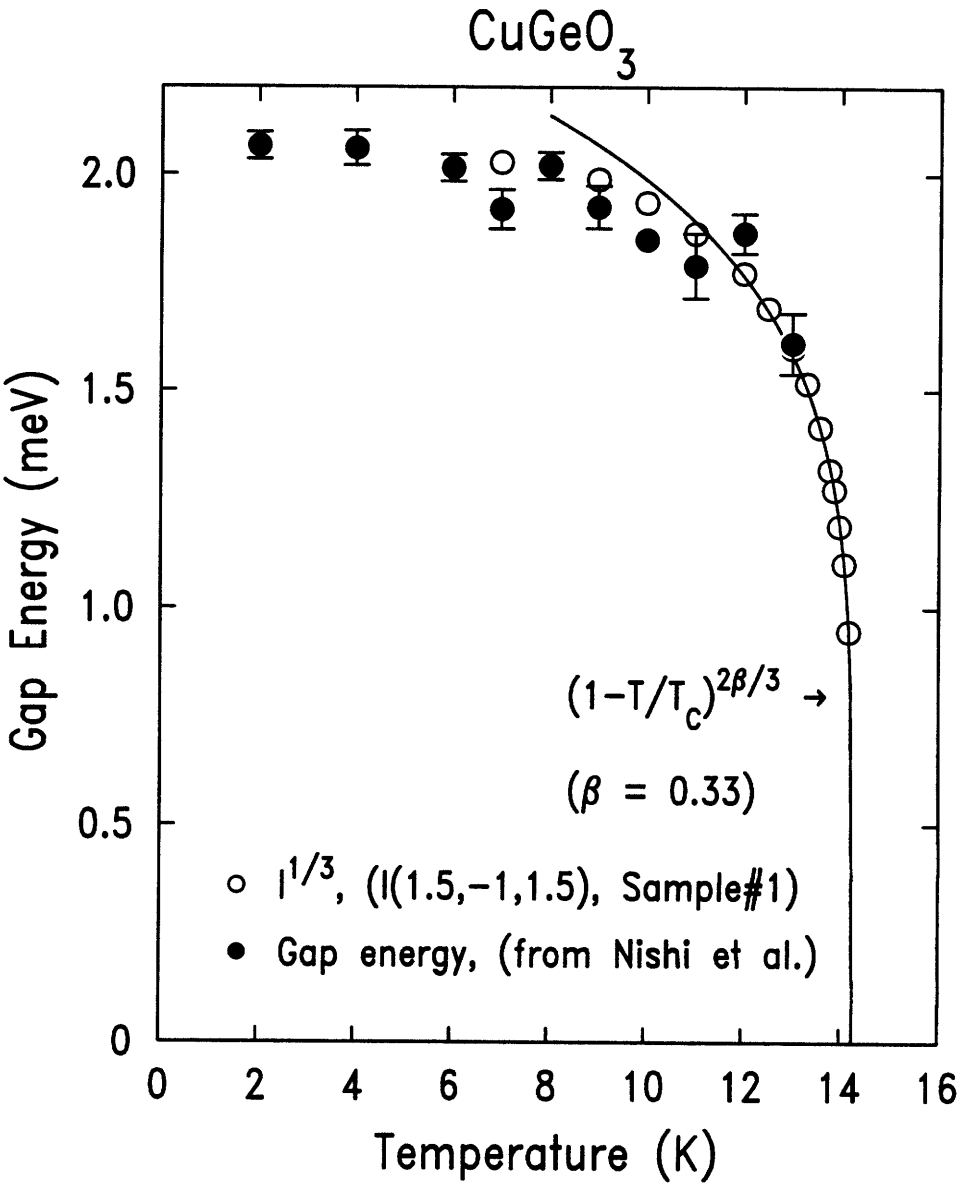

Figure 3-5: Gap energy together with $I^{1/3}$ and the power law in Fig. 3-4 raised to the power $\frac{1}{3}$. The empty circles are the intensity of the superlattice reflection at $I(1.5, -1, 1.5)$ raised to the power $\frac{1}{3}$. The solid line is the power law $(1 - \frac{T}{T_c})^{2\beta}$ of Fig. 3-4 raised to the power $\frac{1}{3}$. The filled circles are the gap energy.

Magnetic Field H	Transition temperature T_{sp}	β ($I \sim (1 - \frac{T}{T_{sp}(H)})^{2\beta}$)
0T	14.25(3)K	0.33(3)
6T	13.57(3)K	0.29(3)
7T	13.33(3)K	0.30(3)

Table 3.1: The depression of the spin-Peierls transition temperature in the magnetic fields.

3.4 Field Dependence of the Spin-Peierls Transition in $CuGeO_3$

Since the spin-Peierls transition is a magnetically driven, progressive spin-lattice dimerization, one expects that the application of an external magnetic field should alter some features of the transition. This is indeed the case in $CuGeO_3$.

This experiment was conducted at X20B. The setup of the experiment was similar to that described in Section 3.2 , except that the incident wavelength was fixed at $\lambda = 0.71$Å. A vertical magnetic field was applied along the direction that was perpendicular to the scattering plane defined by $(h, 0, h)$ and $(0, k, 0)$. The direction of the magnetic field was constrained by the limitation of the tilt angle of the spectrometer (a maximum of $\pm 5°$). However, since the magnetic interactions in a Heisenberg system is isotropic, the field effects on a spin-Peierls transition should be indifferent to which direction the field is applied with respect to its crystalline axes.

The results from magnetic field $H = 6$T and $H = 7$T are plotted in Fig. 3-6. The solid lines in the figure are the best fits of a simple power law, $I \propto (1 - \frac{T}{T_{sp}(H)})^{2\beta}$, where the best fit values for β and T_{sp} in these two fields are listed in Table 3.1, together with the results from $H = 0$T.

Clearly, the magnetic field depresses the spin-Peierls transition temperature in $CuGeO_3$. Apart from this, the phase behavior of the transition in magnetic fields retains the characteristics of that in zero field. However, this is the case only for magnetic fields up to 12.5T. Kiryukhin and Keimer [54] observed an incommensurate phase in $CuGeO_3$ for fields exceeding 12.5T. Specifically, they find that the chains

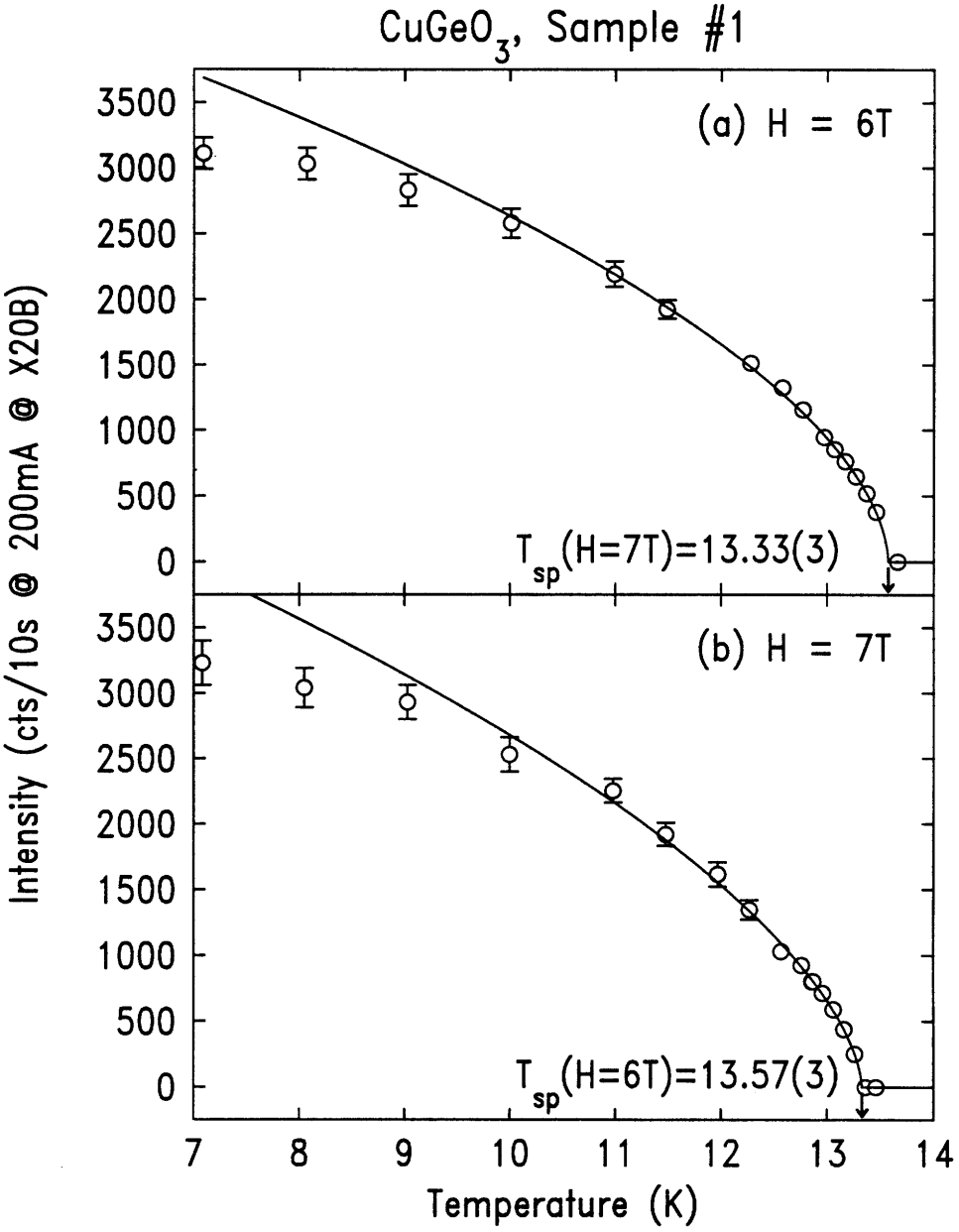

Figure 3-6: The magnetic dependence of the spin-Peierls transition temperature. The magnetic field depresses the spin-Peierls transition temperature. The data at $H = 6$T and $H = 7$T, shown in this figure, were taken at X20B. The solid lines in the figure are the best least-square fits of the data to a simple power law, $I \propto (1 - \frac{T}{T_{sp}(H)})^{2\beta}$, where the best fit β and T_{sp} values in two fields are (a) T_{sp}(6T)=13.57(3)K, β(6T) = 0.29(3). (b)T_{sp}(7T) = 13.33(3)K, β (7T) = 0.30(3). These numbers are to be compared with T_{sp}(0T)= 14.25(3)K and β(0T)= 0.33(3) from a different experiment at X20A on the same sample, Sample # 1.

are no longer simply dimerized, instead the interatomic spacing is modulated with a wavelength determined by the external magnetic field.

3.5 Why $CuGeO_3$ Favors Spin-Peierls Transition?

As we have seen, in many aspects, $CuGeO_3$ has demonstrated itself to be a model spin-Peierls system. However, there are still some questions yet to be answered. Among them, the most significant is how important the interchain couplings are, that is, whether $CuGeO_3$ is best described as a *one*-dimensional antiferromagnetic chain system or a spatially anisotropic *two*-dimensional system. Specifically, the temperature dependence of the magnetic susceptibilities are found to depart significantly from the Bonner-Fisher [72] curve for a linear spin-$\frac{1}{2}$ antiferromagnetic chain. Nishi *et al.* [61] find significant dispersion of the magnetic excitations along both the b and c axes, with zone boundary energies of ~ 6 meV and ~ 16 meV respectively, while the dispersion along the a-axis is negligible.

For pedagogical purpose, it is useful to review the effects of the interchain couplings, in particular their effects on the occurrence of the spin-Peierls transition. Most magnetic systems enter a long-range ordered phase, commonly ferromagnetic or antiferromagnetic, as the temperature is lowered through a transition temperature. However, in the case of an ideal one-dimensional magnetic model with short-range interactions, ordering can occur only at $T = 0$K [21]. Weak interchain interactions are necessary to induce a nonzero transition temperature. Such systems are termed quasi-one-dimensional. The order temperature is related to the ratio of interchain to intrachain coupling and is therefore relatively low. This ratio is, in fact, a measure of the degree of one-dimensional character of the material. Quasi-one-dimensional ordering occurs in a model of exchange-coupled spins on a rigid lattice. If allowance is made for the possibility of an elastic distortion of the lattice, a spin-Peierls transition can occur. One may therefore view the situation as a competition between the spin-phonon and the inter-chain spin-spin coupling. In the case that spin-phonon coupling mechanism dominates, one expects the spin-Peierls transition to occur, and in the case

that inter-chain spin-spin coupling dominates, one expects the quasi-one-dimensional magnetic transition to occur.

As we pointed out earlier, the inter-chain coupling is not that small in $CuGeO_3$, $J_b \approx 0.1 J_c$ [61], a reasonable guess is that the inter-chain interactions would lead the system to a magnetic order, which subsequently would have precluded the occurrence of the spin-Peierls transition. However, in reality, the spin-Peierls transition sets in first, which prevents the establishment of magnetic order at lower temperatures. So what makes the spin-Peierls transition preferencial to the magnetic transition in $CuGeO_3$? Recently, Castilla *et al.* [73] have suggested that it is the competing exchange interactions — the antiferromagnetic interactions between both the nearest and the next-nearest neighbors along the chain direction — that increases the temperature at which the spin-Peierls transition takes place in $CuGeO_3$. As inferred from an electronic calculation by Mattheiss [74], the Cu-Cu superexchange interaction along the chain should be much smaller than typical CuO chains because the $O(2p)$ orbitals are not directed toward both of the adjacent Cu^{2+} ions. Thus, the next-nearest-neighbor interactions may well not be negligible. The view that the next-nearest-neighbor effects play an important role in the spin-Peierls transition in $CuGeO_3$ is supported by Zhang *et al.* [75] in a theoretical study of the phase diagram, ground-state properties and excitation gaps of a spin-Peierls chain with both nearest-neighbor and next-nearest-neighbor interactions; and is further supported by some numerical studies [76, 77], which find that a model including both the nearest-neighbor and the next-nearest-neighbor antiferromagnetic interactions along the chain satisfactorily reproduces the experimental results for the magnetic susceptibility, the dispersion relation, the temperature dependence of the spin-gap, and the spin-Peierls transition temperature of $CuGeO_3$.

The atomic displacements below the transition temperature as determined by Hirota *et al.* [67] in $CuGeO_3$ are also more complicated than the simple dimerization along the chain direction as expected from an idealized spin-Peierls transition. The atomic displacements of Cu^{2+} and O(2) may not only dimerize the intrachain interaction, but may also modify the interchain interactions, suggesting that spin-ladder gap

effects could also play a role [78, 79]. Recently, Plumer [80] employed a Landau-type phenomenological model to describe the atomic displacements below the transition temperature T_{sp} as proposed by Hirota *et al.* [67], and suggested that the Cu displacements are primary, and the O(2) displacements are secondary.

Chapter 4

Thermal Contraction at the Spin-Peierls Transition in $CuGeO_3$

In a neutron scattering study, Lorenzo *et al.* [81] observed an anomalous softening of the longitudinal acoustic phonons propagating along the b-axis perpendicular to the chain direction. They also observed a spontaneous lattice contraction in the same direction below the transition temperature of 14K which coincides with the spin-Peierls transition temperature in the magnetic susceptibility measurements [62, 69], and the superlattice measurements [63, 65, 66, 67]. The motivation of this study was to understand the nature of this thermal contraction, in particular, its relation to the spin-Peierls transition in $CuGeO_3$.

In this chapter, we present an x-ray-scattering measurement of the lattice constant b as a function of temperature under various external magnetic fields [71].

4.1 Experimental Details

This experiment was carried out on MIT/IBM beamline X20B at NSLS. For the details regarding beamline X20B, interested readers are referred to J. P. Hill's thesis [25]. The white x-ray beam from a bending magnet was monochromatized by a single Si(111) crystal. The energy of the incident x-ray photons was fixed at 17.4KeV. Scattering was in the horizontal plane and a flat Si(111) crystal was utilized as the

analyzer. A single crystal of $CuGeO_3$, labeled Sample # 3, grown by the floating zone method, was used in the experiment. The sample was mounted with wave vectors $(0kl)$ in the scattering plane in an x-ray-compatible split pair superconducting magnet. The measurements were carried out around the (080) reciprocal-lattice position, since in this experimental configuration, the ratio of $\frac{\Delta q}{q}$, where Δq is the HWHM, at (080) was the smallest among those at (020), (040), (060) and (080). The longitudinal HWHM at (080) was $\sim 0.0013\text{Å}^{-1}$, while the in-plane transverse resolution was controlled by the sample mosaic of $\sim 0.009°$ HWHM. A variable temperature insert of liquid He flow type was used. Hence stable and reproducible experimental conditions could only be obtained for $T > 7\text{K}$, where the experiment was performed.

4.2 Results and Data Analysis

Representative scans along the K-direction in the reciprocal space, around the reflection (0,8,0) are shown in Fig. 4-1 , at different temperatures. Notice the peak position, which is inversely proportional to the lattice constant, shifts to the smaller values with increasing temperature. The solid lines in the Fig. 4-1 are the best fits of the data to a Lorentzian squared,

$$I(\mathbf{K}) = \frac{I_0}{[(K - K_0)^2 + \kappa_K^2]^2}, \tag{4.1}$$

where $(0, K_0, 0)$ is the reflection position $(0, 8, 0)$.

The experimental results at zero field are shown in Fig. 4-2. The lattice contraction appears below a T_c of $\sim 14.2\text{K}$, consistent with Lorenzo *et al.*'s observation [81]. As noted in Ref. [71, 81], this T_c of $\sim 14.2\text{K}$ coincides with the spin-Peierls transition, T_{sp}. The b-axis direction lattice constant data are well described by the simple form:

$$b(T) = b_0(1 + BT^4) - \Delta b \tag{4.2}$$

where the first term on the right-hand side of the equation is the conventional thermal expansion of the lattice derived from $\alpha \equiv \frac{1}{b}\frac{\partial b}{\partial T} \propto T^3$ for small T [82]. The second

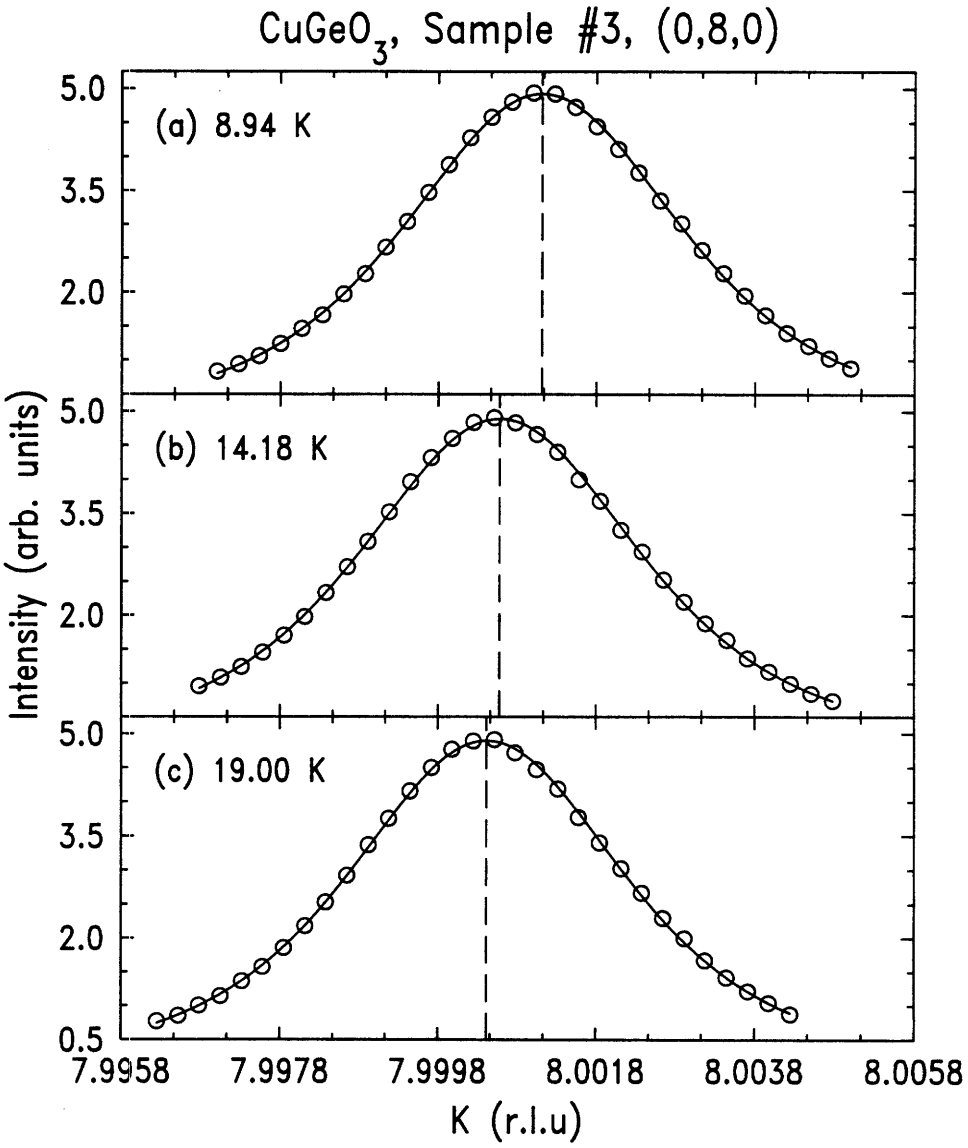

Figure 4-1: Representative scans along the K-direction in the reciprocal space, around $(0, 8, 0)$ across the transition temperature. Notice the peak position, which is inversely proportional to the lattice constant, shifts to the smaller values with increasing temperature. The solid lines are the best fits to a Lorentzian squared, Eq. 4.1 of the data.

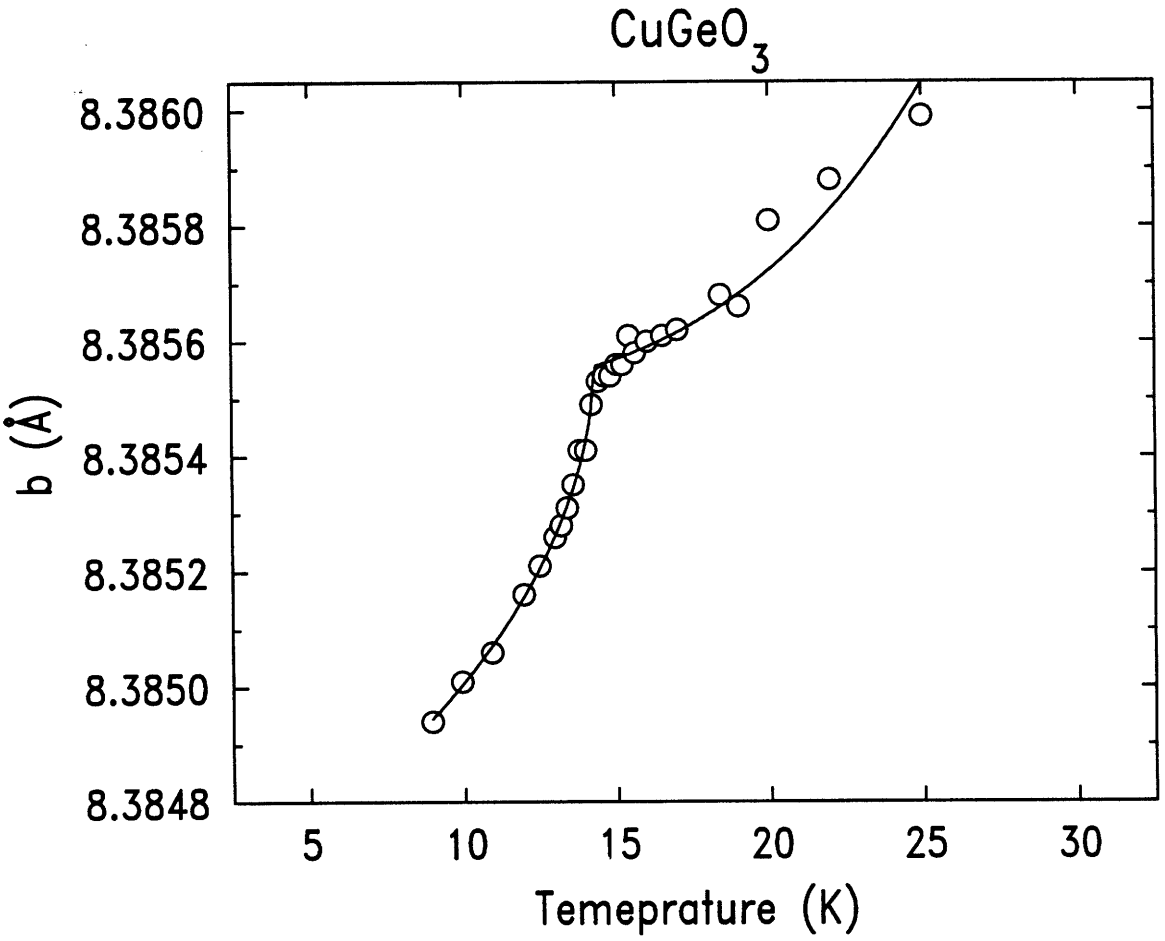

Figure 4-2: The lattice constant b of $CuGeO_3$ as a function of temperature. A spontaneous contraction along the b-axis is observed below a $T_c \sim 14$K. The solid line is the best fit to Eq. 4.2.

term Δb is well represented by the single power-law form:

$$\Delta b = \begin{cases} 0 & T > T_{sp} \\ A(1 - \frac{T}{T_c})^x & T \leq T_{sp} \end{cases} \tag{4.3}$$

where the exponent x is found to be close to 0.5. The solid line in Fig. 4-2 is the result of a least squares fit to Eq. 4.2 of the data with the exponent x fixed at 0.5.

In order to probe further the connection of this thermal contraction along the b-axis to the spin-Peierls transition observed in this compound, we repeated the measurement of the lattice constant as a function of temperature in several fields up to 6T. The magnetic field was applied in the vertical direction, that is, the a-axis direction. Results similar to those found at zero field were obtained for a series of fields up to 6T. Shown in Fig. 4-3 are the lattice constant measurements under $H = 2$T and $H = 5$T along with the lattice constant measurement at $H = 0$T. While applying magnetic fields, the sample position moved slightly compared with that at zero field; this necessitated realigning the spectrometer, thence causing a slight difference in the arm-zero position in different magnetic fields; this subsequently led to a small difference in the apparent absolute value of the lattice constant. Accordingly, in Fig. 4-3 we have normalized the lattice constants in different magnetic fields at 25K.

In Fig. 4-3, the solid curves are the best fits of the data to Eq. 4.2 with $x = 0.5$; one can clearly see that T_c shifts to lower values with increasing magnetic field. Fig. 4-4 shows the magnetic field dependence of T_{sp}. The solid line in the figure is the best fit to:

$$T_{sp}(H) \;=\; T_{sp}(0)\;(1 - \alpha(\frac{\tilde{g}\mu_B H}{2k_B T_{sp}(0)})^2), \tag{4.4}$$

where μ_B is the Bohr magneton and k_B is the Boltzmann constant [41, 52]. The $\tilde{g}$-factors of $CuGeO_3$ observed by ESR along the a-, b- and c-axes are $\tilde{g}_a = 2.15$, $\tilde{g}_b = 2.23$ and $\tilde{g}_c = 2.05$ respectively [83]. The fit value for α is 0.45 ± 0.09, in very good agreement with the value $\alpha = 0.40$ deduced from magnetic susceptibility measurements [62] on a polycrystalline sample of $CuGeO_3$. These two values for α in turn also agree well with the theoretical values of 0.44 calculated in the Hartree-Fork ap-

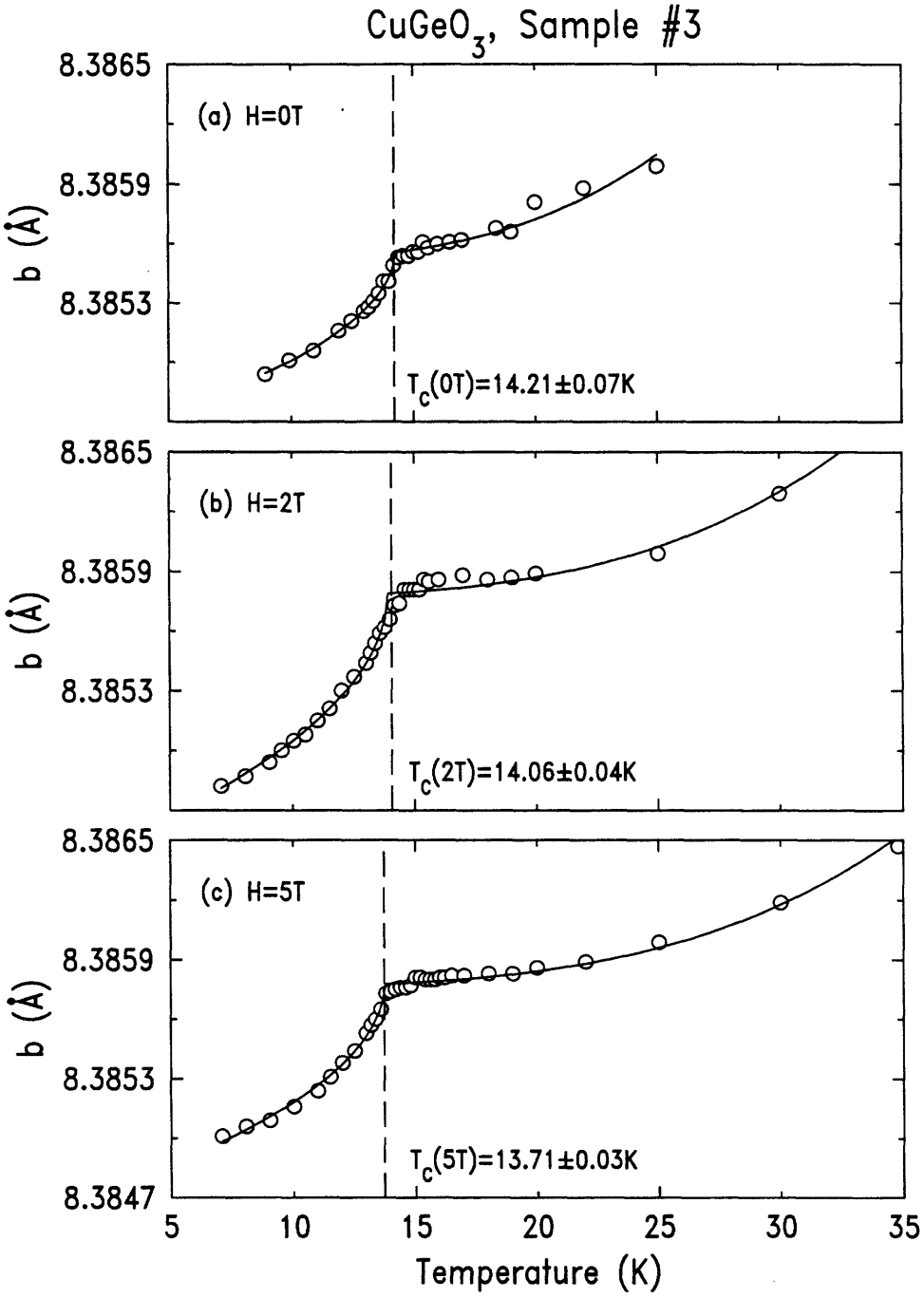

Figure 4-3: The lattice constant b of $CuGeO_3$ as a function of temperature and magnetic field. A spontaneous contraction along the b-axis is observed below $T_c \sim$ 14K; the solid lines are the best fits to Eq. 4.2 & Eq. 4.3 with exponent $x = 0.5$. The fit error bars are smaller than the symbols shown in the figure, though the absolute error bars are larger. (a) $H = 0$T, $T_c(0) = 14.21 \pm 0.07K$. (b) $H = 2$T, $T_c(2T) = 14.06 \pm 0.04K$. (c) $H = 5$T, $T_c(5T) = 13.71 \pm 0.03K$. The lattice constants in different magnetic fields are normalized at 25K.

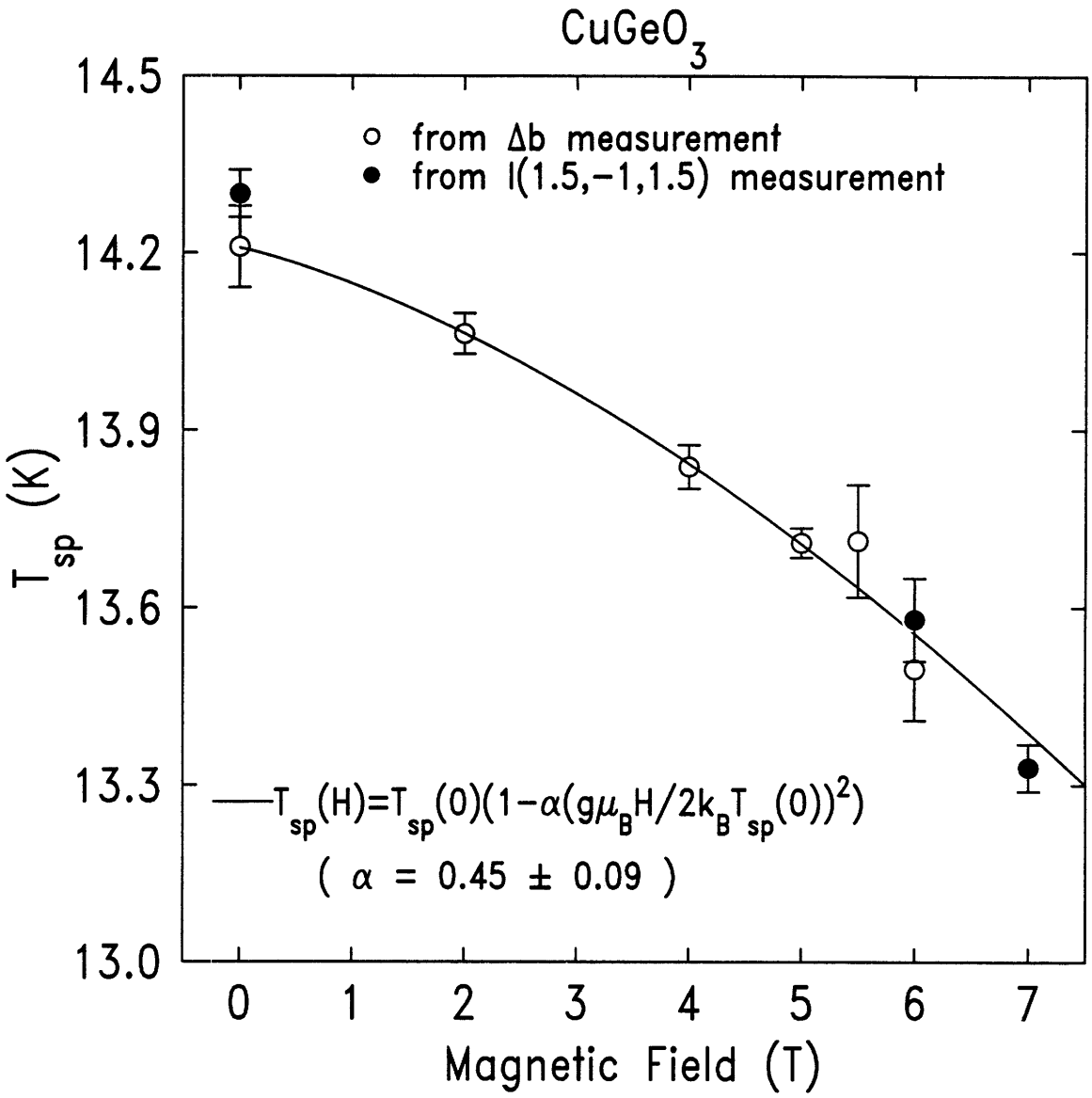

Figure 4-4: The transition temperature T_{sp} as a function of applied magnetic field H. The solid line is the result of a least squares fit to the form $T_{sp}(H) = T_{sp}(0)\left(1-\alpha\left(\frac{g\mu_B H}{2k_B T_{sp}(0)}\right)^2\right)$, where the fit value of α is 0.45 ± 0.09. The magnetic field dependence of the transition temperature $T_{sp}(H)$ agrees quantitatively with the results from magnetic susceptibility measurements.

proximation [41] and 0.36 in a theory based on the Luther-Peschel type treatment of the spin-correlation functions [52]. We note that the approximation of Eq. 4.4, $\frac{g\mu_B H}{k_B T_{sp}(0)} \ll 1$, is only moderately well satisfied since $\frac{g\mu_B H}{k_B T_{sp}(0)} \sim 0.1$ and 0.6 for H=1T and 6T respectively.

We also fitted all of the b-axis lattice constant data simultaneously to the following equation:

$$b(H,T) = b_0(1 + BT^4) - \Delta b(H,T) \tag{4.5}$$

where

$$\Delta b(H,T) = \begin{cases} 0 & T > T_{sp}(H) \\ A(H)(1 - \frac{T}{T_{sp}(H)})^x & T \leq T_{sp}(H) \end{cases} \tag{4.6}$$

with b_0, B, $A(H)$, $T_{sp}(H)$ and x as adjustable parameters. The best fit gives $x = 0.53 \pm 0.02$. This value for x provides satisfactory fits to the temperature dependence of Δb at all magnetic fields studied.

As noted in Chapter 6, the intensity (I) of the superlattice reflections from the x-ray [63] and neutron diffraction measurements [67] is well described by a simple power law, $I \propto (1 - \frac{T}{T_{sp}})^{2\beta}$. In Fig. 4-5, we show the measured lattice contraction Δb from x-ray studies together with the intensity of the superlattice reflection at $I(0.5, 5, 0.5)$ from neutron measurements [67], and the intensity $I(1.5, -1, 1.5)$ of the superlattice reflection at $(1.5, -1, 1.5)$ from x-ray measurement [63]. The agreement is clearly quite good; this can be understood simply as originating in the coupling between the lattice contraction and the order parameter in a Landau free energy formalism. We also note that both Δb and the intensities are well described by a single power law $(1 - T/T_c(0))^y$, with the best fit value of exponent y being 0.58(8).

The appearance of the superlattice reflections is the result of the Cu^{2+} dimerization and oxygen displacements below the spin-Peierls transition temperature. If we let δ denote a generalized lattice distortion amplitude, then the intensity of the superlattice reflections, I, is simply proportional to δ^2. We can write down the extended Landau

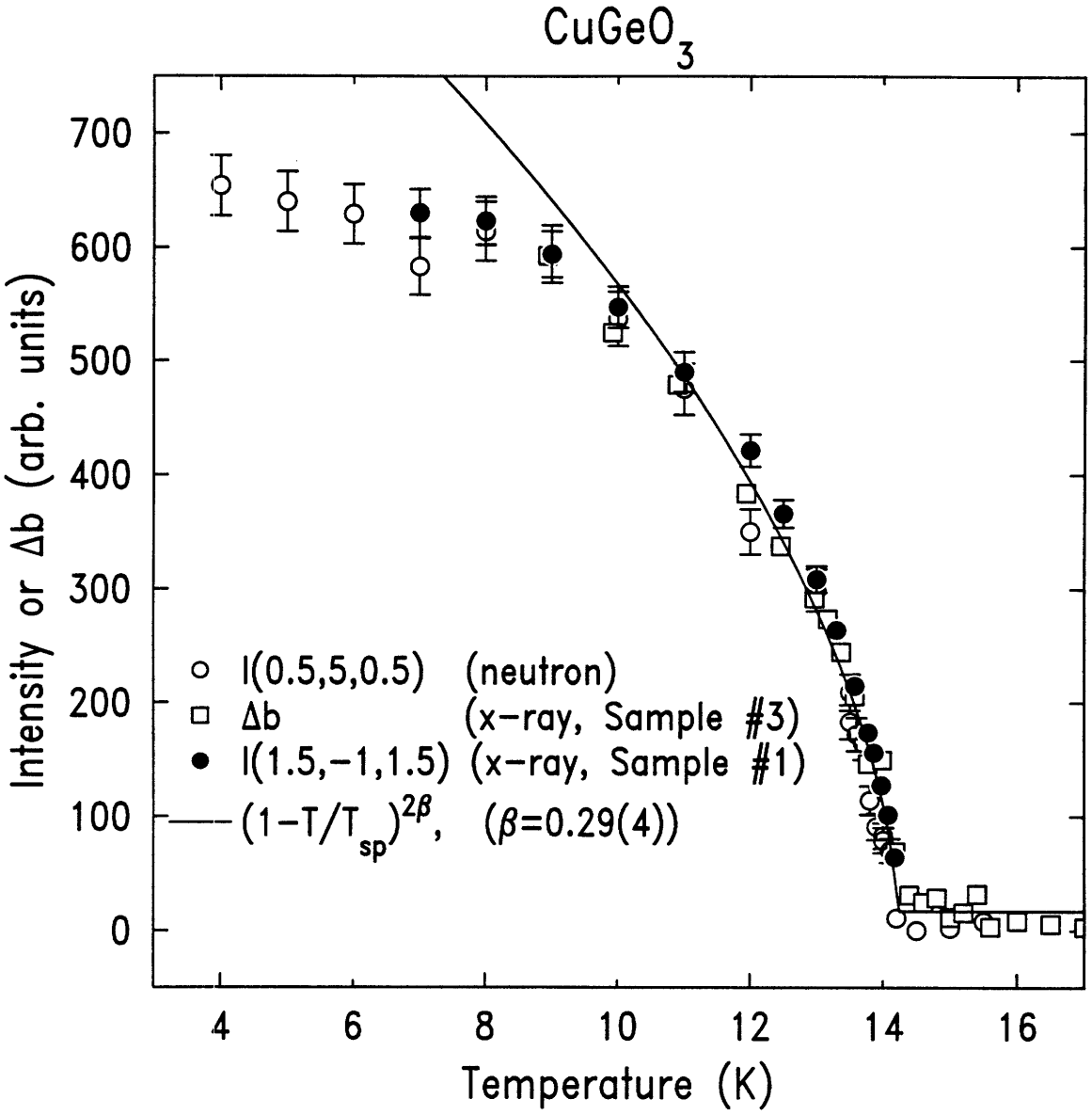

Figure 4-5: Δb together with the intensity, I, of the superlattice reflections measured using x-ray and neutron diffraction techniques. The empty circles are the intensity of the superlattice reflection at $(0.5, 5, 0.5)$ measured by neutron scattering. The filled circles are the intensity of the superlattice reflection at $(1.5, -1, 1.5)$ measured by x-ray scattering technique. The empty squares are the lattice contraction Δb data from the x-ray measurements reported here. The solid line is the result of the fit of all data to a simple power law, $I \propto \left(1 - \frac{T}{T_{sp}}\right)^{2\beta}$, where the fit value of β is 0.29 ± 0.04.

free energy F after integrating out the spin degrees of freedom [84]:

$$\mathcal{F} = \mathcal{F}_0 + \frac{1}{2}a(T - T_{sp})\delta^2 + \frac{1}{4}u_4\delta^4 + \frac{1}{6}u_6\delta^6 + \frac{1}{2}K(\Delta b)^2 + \gamma\Delta b\delta^2 \qquad (4.7)$$

where $\frac{1}{2}K(\Delta b)^2$ is the elastic energy contribution of the lattice contraction (K is the corresponding elastic constant) and the $\gamma\Delta b\delta^2$ term represents the lowest order non-vanishing coupling between the distortion amplitude δ and the contraction Δb. From the condition that the sample is stress-free, one has $\frac{\partial\mathcal{F}}{\partial(\Delta b)} = 0$, which gives:

$$\Delta b = -\frac{\gamma}{K}\delta^2. \qquad (4.8)$$

Combining Eq. 4.8 with $I \propto \delta^2$, we have $\Delta b \sim I$, which is exactly the result displayed in Fig. 4-5.

By inserting Eq. 4.8 back into the free energy expression Eq. 4.7, we can see some indication why β might be close to the tricritical value of 0.25. Combining Eq. 4.7 and Eq. 4.8, one has:

$$\mathcal{F} = \mathcal{F}_0 + \frac{1}{2}a(T - T_c)\delta^2 + \frac{1}{4}(u_4 - \frac{2\gamma^2}{K})\delta^4 + \frac{1}{6}u_6\delta^6. \qquad (4.9)$$

Since $u_4' \equiv (u_4 - \frac{2\gamma^2}{K}) < u_4$, the system is closer to a tricritical point ($u_4 = 0$ at the tricritical point) than the non-coupling situation ($\gamma = 0$). The magnetoelastic interaction between the 1D antiferromagnetic chains and the 3D phonon field in the lattice drives the system $CuGeO_3$ through a spin-Peierls transition and opens up a finite energy gap in the spin excitations spectrum [61, 64] by dimerizing the lattice [63, 65, 66, 67]. The atomic shifts induce the lattice contraction Δb and the coupling between the contraction and the lattice distortion in turn puts the system near the tricritical point. A similar argument might be made for the organic spin-Peierls system TTF-$CuS_4C_4(CF_3)_4$ which instead has $\beta = 0.5$. However, in that case, there is a precursive 3D soft phonon mode at the superlattice position which persists to very high temperatures [34]. Cross and Fisher [31] argue that this soft phonon mode causes the mean field $\beta = \frac{1}{2}$ behavior in the TTF-$CuS_4C_4(CF_3)_4$ salt. No such soft

phonon has been observed in $CuGeO_3$ so far.

We also observed a small increase of the lattice constant a in the a-axis direction below the transition temperature T_c (Fig. 4-6). The change of the lattice constant a between 10K and 15K is about 0.002%, which is to be compared with the 0.0065% change along the b-axis direction.

The relevance of the appearance of these elastic anomalies to the spin-Peierls transition in $CuGeO_3$ is further confirmed in several recent experimental studies: Winkelmann *et al.* [85] measured the thermal expansion coefficients α of $CuGeO_3$ along the three orthorhombic directions using a high-resolution capacitance dilatometer; Poirier *et al.* [86, 87] and Saint-Paul *et al.* [88] measured elastic constants of $CuGeO_3$ with an ultrasonic propagation technique. The results they obtained are consistent with those reported here.

4.3 Summary

In summary, we have accurately measured the lattice constant b as a function of temperature and magnetic field in $CuGeO_3$. A spontaneous thermal contraction Δb is observed below the transition temperature T_c of about 14K, which coincides with the spin-Peierls transition temperature, T_{sp}. The quadratic magnetic field dependence of T_{sp} agrees quantitatively with the results from the magnetic susceptibility measurements [62], which in turns agrees with theory [41, 52]. Δb is well described by a simple power law, with an exponent x close to 0.5. Δb is also found to scale with the intensity of the superlattice reflections, which is explained through a simple coupling term between the contraction and the order parameter in the Landau free energy formalism. It is noted that the transition may be close to a tricritical point. Future, more precise experiments on the heat capacity, the critical fluctuations above T_c and the order parameter below T_c should serve to distinguish between tricritical behavior and the expected asymptotic 3D Ising behavior at the spin-Peierls transition.

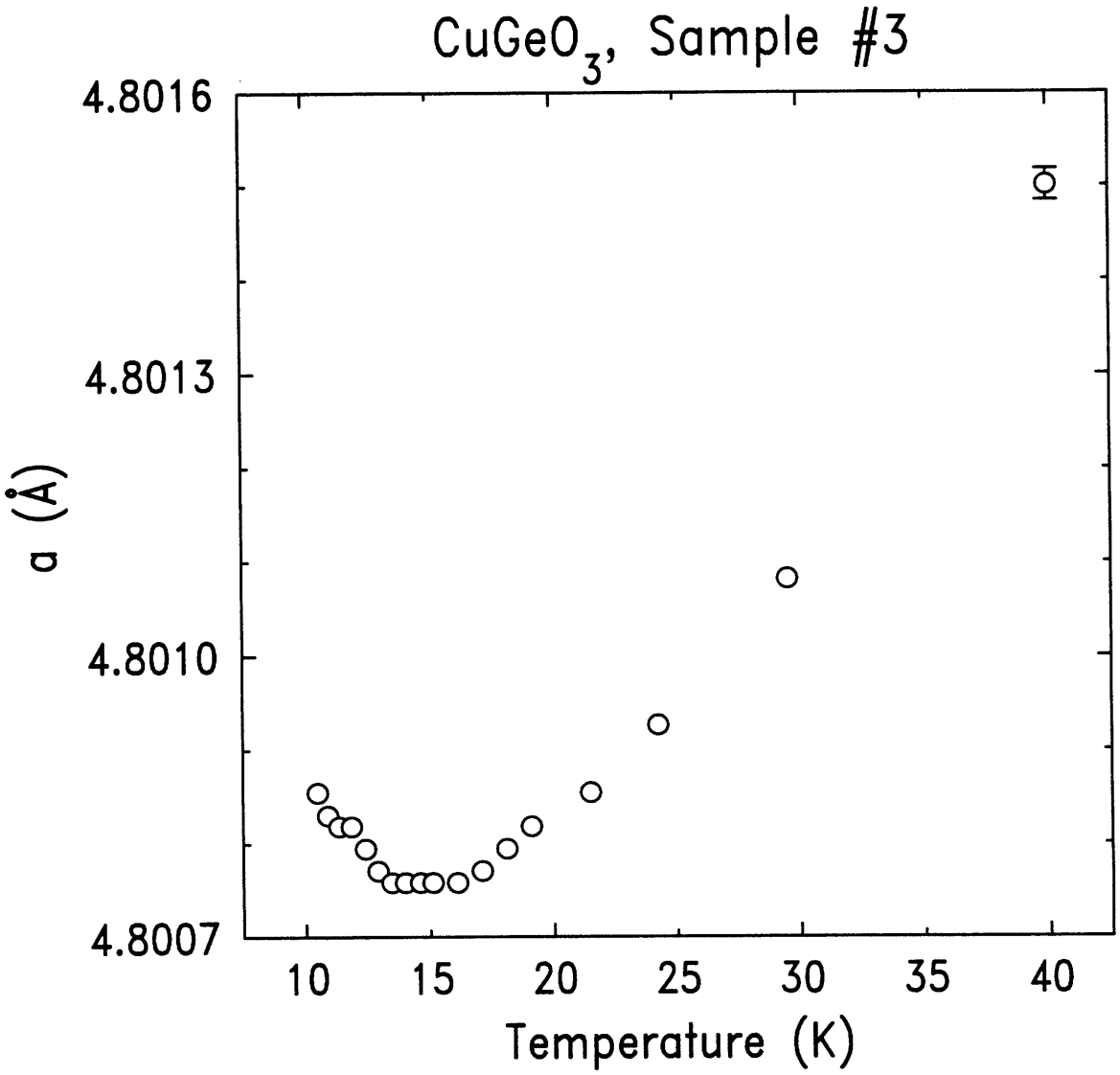

Figure 4-6: The lattice constant along the a-axis as a function of temperature.

Chapter 5

Large Length Scale Fluctuations at the Spin-Peierls Transition in $CuGeO_3$

A second order phase transition is one in which the order parameter (*e.g.* the sublattice magnetization in a paramagnet-to-antiferromagnetic phase transition or the lattice distortion in a structural transition) grows continuously from zero as the temperature is lowered below the critical temperature T_c. Above T_c, there is no long-range order, but one finds that regions with typical linear dimension ξ, the *correlation length*, tend to be momentarily ordered such that the system exhibits critical fluctuations into the ordered phase with characteristic length ξ. As T approaches T_c, ξ becomes longer and longer, and eventually it diverges at T_c, with a characteristic behavior, $\xi = \left(1 - \frac{T}{T_c}\right)^{-\nu}$, where ν, like β, is a critical exponent.

The modern theory of critical phenomena rests in a fundamental way on the assumption that the correlation length ξ is the only length scale at a given temperature, *i.e.* that all quantities having the dimension of length will change with temperature as ξ itself. This is the *scaling hypothesis.* Recently however, the existence of a second larger length scale fluctuation has been reported in a couple of magnetic systems [89, 90, 91, 92, 93]. These results are reminiscent of the two length-scale phenomenon reported at the cubic-to-tetragonal structural transition in some

perovskites [94, 95, 96, 97, 98, 99, 100]. However, in the case of structural transitions in perovskites, the situation is made complicated by the first-order nature of the transition in the bulk sample.

In this Chapter, we report the observation of large length scale lattice fluctuations at the spin-Peierls transition in $CuGeO_3$. The length scale of these fluctuations is about an order of magnitude larger than that characterizing the thermal fluctuations probed with neutron [70] and lower resolution x-ray scattering [66]. Detailed deconvolution of the effects of the instrumental resolution function on the measured profiles suggests that the intrinsic line shape is described by a Lorentzian squared form. We suggest that a model involving both random fields and random bonds not only explains our experimental results, but also appears consistent with the published data on the two length scale phenomenon in other systems [63]. The experimental set-up is identical to that of Section 3.2 in Chapter 3. We therefore proceed directly to present the experimental results.

5.1 Large Length Scale Lattice Fluctuations

As the sample, $CuGeO_3$, is heated above the transition temperature T_{sp}, the superlattice peak broadens rapidly and anisotropically in all three directions. Representative scans at temperatures 0.2K and 0.55K above T_{sp} are shown in the Fig. 5-1. The solid lines are the best fits of these scans to the following functional form:

$$I(\mathbf{q}) = \int R(\mathbf{q}')S(\mathbf{q}-\mathbf{q}')d\mathbf{q}' \tag{5.1}$$

where $I(\mathbf{q})$ is the measured intensity at the momentum transfer $\mathbf{q}$, and $R(\mathbf{q}')$ represents the experimentally measured instrumental resolution function (Eq. 3.1). The cross-section, $S(\mathbf{Q})$, which we take as a Lorentzian squared, is given by:

$$S(\mathbf{Q}) = \frac{T\chi_d}{[1+(H-H_0)^2/\kappa'^2_H + (K-K_0)^2/\kappa'^2_K + (L-L_0)^2/\kappa'^2_L]^2} \tag{5.2}$$

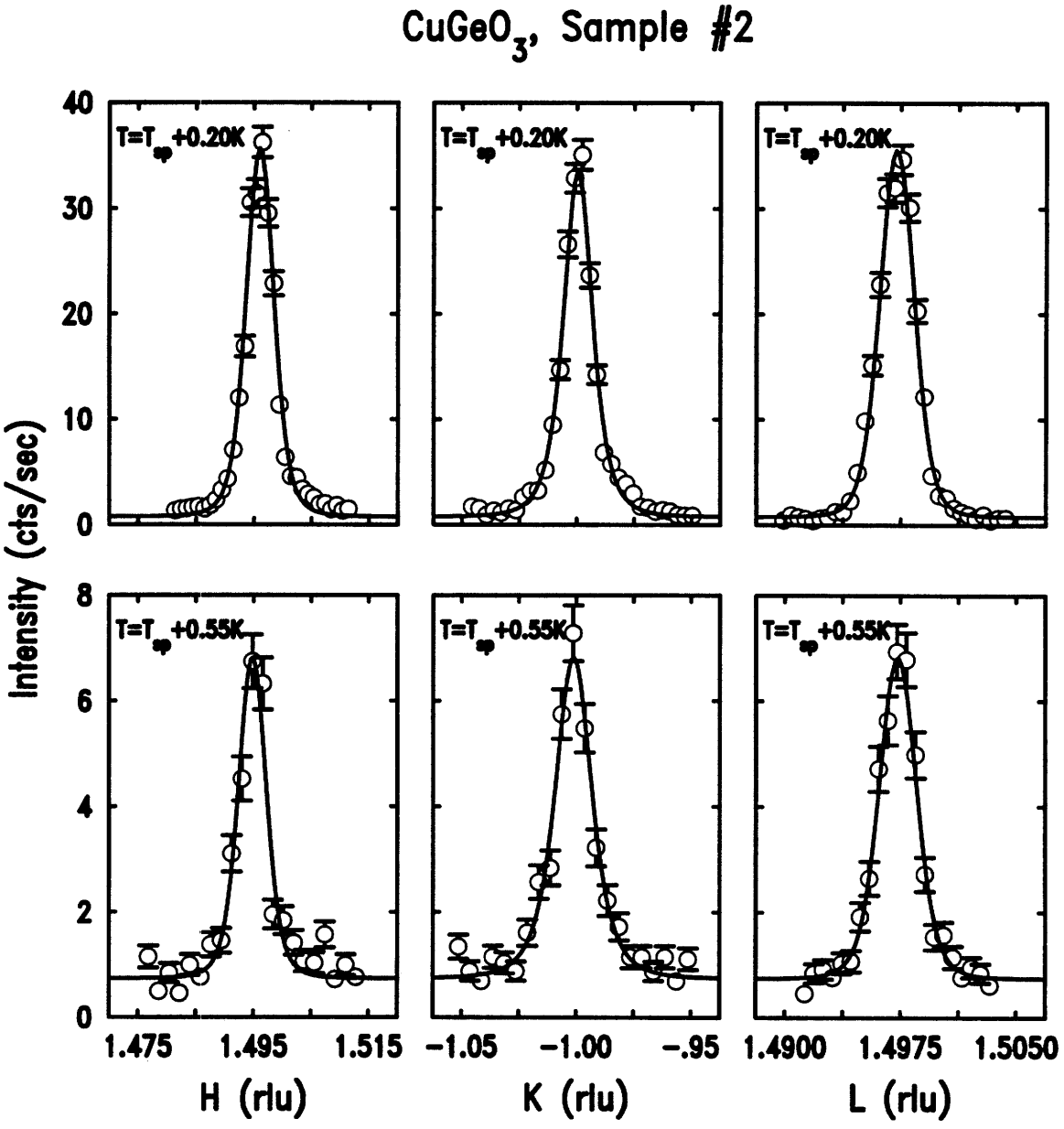

Figure 5-1: The diffuse scattering arising from the large length-scale fluctuations observed at temperatures 0.2 and 0.55K, respectively, above the transition temperature T_{sp}. The solid lines are the results of least-square fits of the data to a Lorentzian squared line shape convoluted with the instrumental resolution function. The count rates are normalized to a ring current of 200mA.

Temperature	The value of χ^2 with S(**Q**) given by a Lorentzian	The value of χ^2 with S(**Q**) given by a Lorentzian squared
T_{sp}+0.10K	9.388	5.542
T_{sp}+0.15K	4.986	2.002
T_{sp}+0.20K	4.353	2.819
T_{sp}+0.25K	2.233	2.654
T_{sp}+0.30K	2.287	2.423
T_{sp}+0.75K	1.060	1.163

Table 5.1: Comparison between the fits to Eq. 5.1 of the data, with the cross-section, $S(\mathbf{Q})$ given by either a simple Lorentzian and a Lorentzian squared to the data for $T > T_{sp}$. The value of χ^2 indicates the goodness of the fit.

This choice of a Lorentzian squared is motivated by earlier research on the two length scale phenomenon [89, 94] and the possible origin of the large length scale fluctuations observed here, which we shall discuss later in this section. We have also tried to fit the data to Eq. 5.1 with $S(\mathbf{Q})$ given by a simple Lorentzian. We found that, although away from T_{sp} both Lorentzian and Lorentzian squared line shapes give similar quality of fits, for the data very close to the transition temperature T_{sp}, the cross-section given by a Lorentzian squared describes the data much better than that given by a simple Lorentzian. This is reflected in a smaller goodness-of-fit χ^2 value for the Lorentzian squared line shape near T_{sp}, as shown in Table 5.1.

Least squares fits of these scans to Eq. 5.2, convoluted with the instrumental resolution function, Eq. 3.1, yield values for the inverse correlation lengths κ'_{H}, κ'_{K} and κ'_{L} as well as the staggered susceptibility χ_d. The solid lines in Fig. 5-1 represent the results of such fits. Evidently, as stated above, Eq. 5.2 describes the measured profiles quite well. The results of these fits are given in Fig. 5-2 which shows the inverse of the correlation lengths along the **H, K** and **L** directions as functions of the reduced temperature. The correlation lengths diverge continuously as the temperature approaches T_{sp}. The solid lines represent the results of fits to simple power laws, $\xi'^{-1} \sim t^{\nu}$, for the data close to T_{sp}. The best fit value for the exponent ν is 0.56 ± 0.09, which is consistent with the result $\nu \sim \frac{1}{2}$ from Ref. [66] obtained for the thermal critical fluctuations over a much wider range of temperature (15 K $\leq$ T $\leq$

40K). However, there are marked differences between the results shown in Fig. 5-2 and those reported by Pouget *et al.* [66] and Hirota *et al.* [70]. First, we find that the length scale of the fluctuations in *both* samples studied in this work is about an order of magnitude larger than that observed by Pouget *et al.* [66] and Hirota *et al.* [70]. Secondly, the anisotropy ratio associated with these large length scale fluctuations is different from that reported in Ref. [66]. Namely, instead of the relationship $\xi_c : \xi_b : \xi_a \sim 5.5 : 1.8 : 1$ in the vicinity of T_{sp}, the large length scale fluctuations exhibit $\xi'_c > \xi'_a > \xi'_b$.

Concomitantly, the amplitude, $S(0) \sim \kappa_B T \chi_d$ observed in our high-resolution x-ray measurements increases precipitously with decreasing temperature. Fig. 5-3 shows χ_d as a function of reduced temperature on a semi-log plot. The solid line is the best fit to a simple power law, $\chi_d \sim t^{-\bar{\gamma}}$, of the data, with the best fit $\bar{\gamma}$ value of 2.0 ± 0.3. The value of T_{sp} determined by fitting the simple power law, t^{ν}, to the inverse of the correlation lengths above T_{sp} is consistent with the value for T_{sp} obtained from power law ($t^{-\bar{\gamma}}$) fits of χ_d above T_{sp}. These fitted values for T_{sp}, in turn, are consistent with the value of T_{sp} determined by fitting a simple power law, $t^{2\beta}$, to the peak intensity for the data below T_{sp}. We note that for conventional thermal critical scattering the susceptibility exponent $\gamma < 2\nu = 1.12 \pm 0.18$, whereas we find $\bar{\gamma} = 2.0 \pm 0.3$. This difference may provide an important clue to the microscopic origin of the large length scale fluctuations in $CuGeO_3$.

5.2 The Effects of Defects and Strains

Although we cannot pinpoint the precise origin of the large length scale fluctuations observed in this work, earlier work on the two length scale phenomenon indicates that the narrow component arises predominantly from the outer 0.1mm of the sample [91, 92, 93] and is correlated with random defects in the sample [94, 101]. In all systems studied to-date, the length ratio between the large length scale fluctuations and the bulk critical fluctuations is a factor of 10 to 20. Further, the large length scale scattering profiles are better described by a Lorentzian squared rather than a

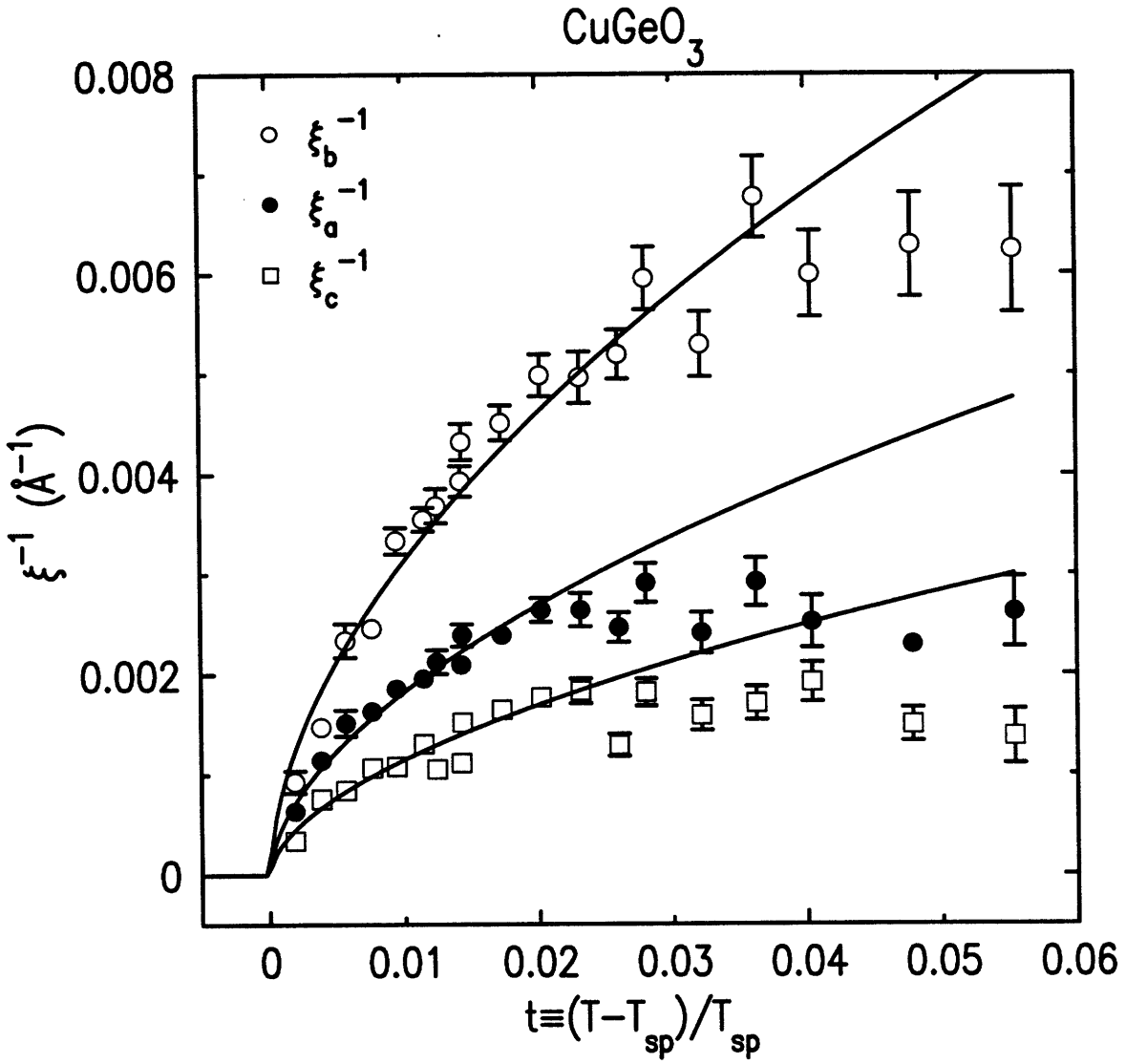

Figure 5-2: Inverse of the correlation lengths along the **H**, **K** and **L** directions as functions of the reduced temperature. The solid line for ξ_b^{-1} data represents the results of a least squares fit to a simple power law, $\xi_b^{-1} \sim t^{\nu}$, of the data, with the best fit ν value of 0.56 ± 0.09, while the solid lines for the data along the other two directions represent the results of power-law fits of the data close to the transition temperature with the exponent ν fixed at 0.56.

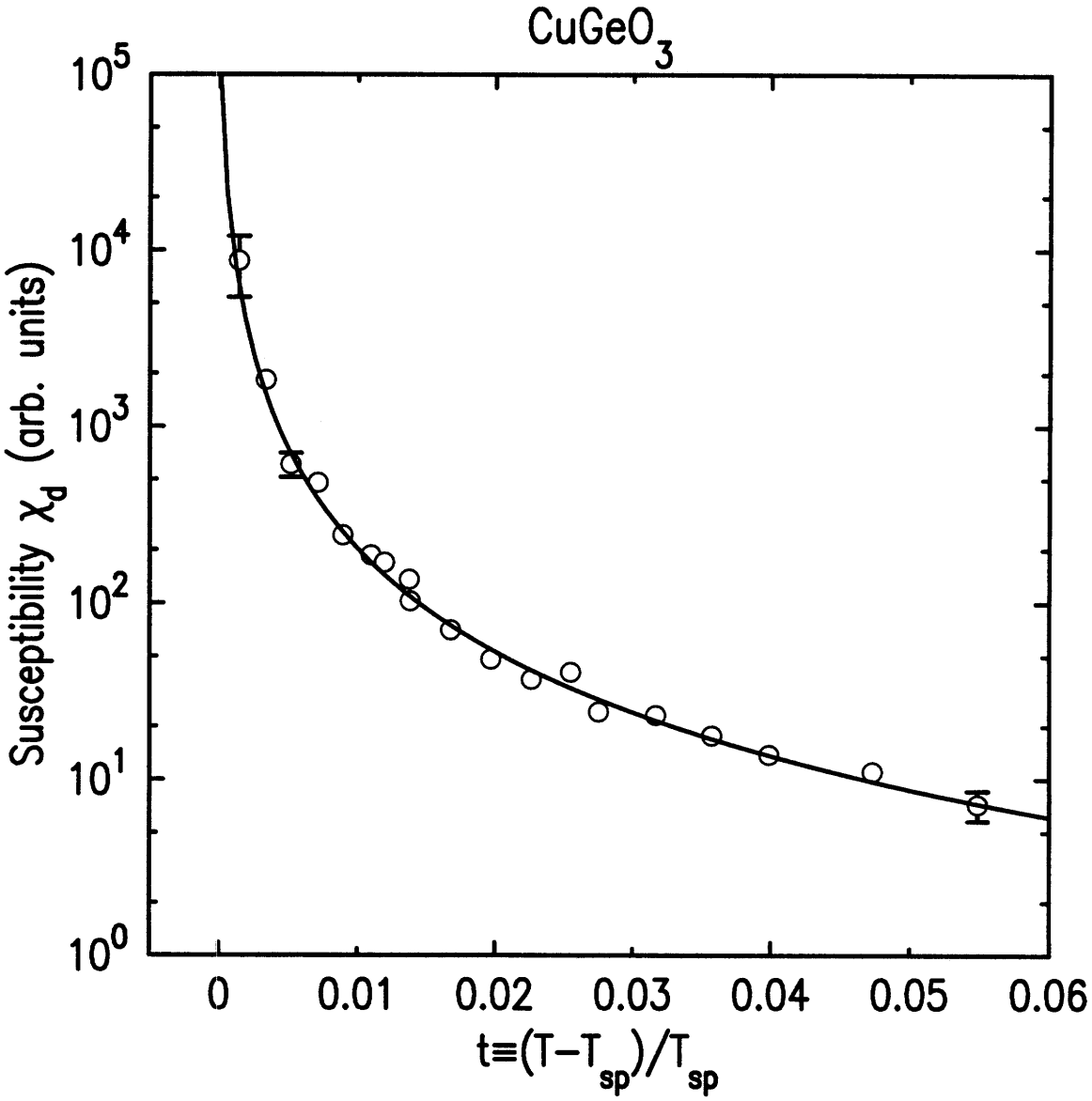

Figure 5-3: χ_d as a function of the reduced temperature plotted on a semi-log scale. The solid line is the result of a least squares fit to a simple power law, $\chi_d \sim t^{-\bar{\gamma}}$, of the data. The best fit value of $\bar{\gamma}$ is 2.0(3).

simple Lorentzian line-shape. Finally, in $CuGeO_3$ as well as in certain other systems, the Lorentzian squared amplitude exponent $\bar{\gamma}$ is $\sim 3.5\nu$. It is not clear at this stage how universal this latter result is.

The large length scale fluctuations in $CuGeO_3$ can be simply explained by postulating that they arise from extended defects or strains in the near-surface region. These defects may create both random bonds and random fields. If the random field aspects dominate, then technically, we could expect that asymptotically, $CuGeO_3$ would exhibit a random field Ising spin-Peierls phase transition. More generally in the random field picture one would expect crossovers from mean field to Ising to random field Ising behavior as T_{sp} is approached from above and below (for a review of theory, see Ref. [102]). In each of these separate temperature regions $S(\vec{Q})$ should be comprised of both connected and disconnected components [102, 103]. The former is typically described by a Lorentzian line-shape and the latter by a Lorentzian squared profile [103, 104]. In mean field theory for random field Ising magnets the characteristic lengths for the Lorentzian and Lorentzian squared components should be the same [103]. More generally, however, scaling only requires that the exponents and not the absolute lengths be identical. A dramatic illustration of this phenomenon has recently been found for the first and second harmonic fluctuations in XY density wave systems [105]. In that case the first and second harmonic correlation lengths differ by nearly an order of magnitude even though the exponents themselves are, by necessity, the same. To explain the large length scale phenomenon in $CuGeO_3$ we would then simply hypothesize that with high resolution x-rays we measure the disconnected susceptibility which arises from random fields associated with strains and defects in the near-surface region probed by the x-rays. We would hypothesize further that the disconnected susceptibility is characterized by fluctuations whose absolute length scale is about a factor of 10 larger than that characterizing the thermal fluctuations as measured by neutrons or diffuse x-ray scattering. Presumably, this larger length scale would be caused by the extended nature of the defects generating the random fields. For the amplitude of the disconnected susceptibility one has the exponent $\bar{\gamma} = (4 - \bar{\eta})\nu$ with $0 \leq \bar{\eta} < 1$ for a second order phase transition [106, 107].

In $CuGeO_3$ we determine $\bar{\gamma} = 3.6\nu$, consistent with the above bound for $\bar{\eta}$. The fact that we find $\nu = 0.56 \pm 0.09$ would imply that over the measured temperature range one is in the mean field ($\nu = \frac{1}{2}$) and/or Ising ($\nu = 0.63$) [108, 109] rather than random field Ising ($\nu \simeq 1.4$) [106, 107] critical regimes. Below T_{sp} we measure $\beta = 0.33(3)$ which also is consistent with simple Ising rather than random field Ising behavior [106, 107, 108, 109]. In this model, asymptotically close to T_{sp}, one must measure random field Ising critical behavior. From our empirical results we would hypothesize that the defect density is sufficiently low that the random field Ising critical regime only occurs very close ($< 0.1K$) to T_{sp}.

The above random field model appears to be consistent with the data of Thurston *et al.* [89, 90] in holmium. In that case for $t < 10^{-2}, \nu \simeq 1$ and $\bar{\gamma} \simeq 4$; for $t > 10^{-2}$ Thurston *et al.* [89, 90] find $\nu \simeq 0.5$ and $\gamma \simeq 1.2$ for the thermal fluctuations. To be consistent with our picture, this would require that as T_{sp} is approached there is a crossover from mean field/critical behavior to random field critical behavior at $t \sim 10^{-2}$ in the near surface region of the holmium sample as probed by x-rays.

Altarelli *et al.* [110] have emphasized the random bond rather than the random field aspects of near-surface defects and dislocations. As we have noted above, we expect both random field and random bond effects to occur and in a given physical system, it is simply a matter of which dominates over the measured temperature range. For defects which produce short range random bond disorder one expects only a subtle change in the critical behavior and no dramatically new length scale [111]. As emphasized in Ref. [110], building on the work of Weinrib and Halperin [112], more dramatic effects may occur if the random bond disorder is of long range. Specifically if the attendant temperature fluctuations fall off with distance like r^{-a} then one expects a crossover to new critical behavior with $\nu_s = 2/a$. This random bond picture appears to be consistent with the data of Gehring *et al.* [91, 92, 93] in terbium. We emphasize that in random bond systems the narrow component arises from the connected rather than the disconnected susceptibility. A model involving both random fields and random bonds also appears to be consistent with the published data on the two length scale phenomena accompanying various structural phase transi-

tions [94, 95, 96, 97, 98, 99, 100]. However, in these cases the interpretation is made complicated by the first order nature of the transition in the bulk sample. Indirect support for the importance of quenched defects in solids comes from measurements of the critical fluctuations of the nematic-smectic A transition in thermotropic smectic liquid crystals. These systems, which typically have annealed rather than quenched disorder, do not exhibit large length scale fluctuations [113].

We believe that the large length scale fluctuations in $CuGeO_3$ which we have measured can be understood heuristically by considering the effects of extended random field defects in the near-surface region of the sample. More generally, to explain data obtained to-date on large length scale fluctuations in a wide variety of physical systems, one must consider the effects of both random bonds and random fields generated by the presumed near-surface defects. It is, of course, possible that the large length scale fluctuation phenomenon is truly intrinsic and would occur in the near-surface region of a defect-free crystal undergoing a second order phase transition. In that case, one must devise a surface region-specific mechanism which would generate the large length scale fluctuations in solids over macroscopic distances ($\sim$0.1mm) beneath the surface. Clearly, much more work will be required to unravel this conundrum and to put the above ideas on a quantitative basis both experimentally and theoretically.

Part II

Phases and Phase Transitions in the Mixed Ising-XY Magnet: $Fe_xCo_{1-x}TiO_3$

In recent times, as homogeneous systems have become increasingly well understood, the emphasis in condensed matter physics has shifted from the properties of perfect systems towards those of imperfect systems. This is because imperfect systems are, in a sense, generic by nature, while perfectly ordered structures are, strictly speaking, idealized objects. One important class of imperfect systems is the class of systems with quenched disorder. These are systems in which the disorder has been 'frozen in'. Random magnets have emerged as prototypes for a wide variety of systems with quenched disorder. This is due in part to the fact that many different kinds of generic randomness can be physically realized in magnetic systems, and in part to the remarkable fact that simple models of magnetism often capture the essential physics of much more complicated systems.

In the second half of this thesis, we present synchrotron x-ray scattering studies of the mixed Ising-XY magnet with quenched randomness: $Fe_xCo_{1-x}TiO_3$. This Part is organized as follows. In Chapter 6, we state the motivation of this work, and give a brief description of the physical properties of the binary solid solution $Fe_xCo_{1-x}TiO_3$. In Chapter 7, we detail the results of random anisotropy and random field effects on the XY behavior in $Fe_xCo_{1-x}TiO_3$ ($x = 0.35$, 0.50 and 0.65). Finally, in Chapter 8 we describe the effects of applied magnetic fields on the phase behavior of the mixed random Ising magnet, $Fe_{0.75}Co_{0.25}TiO_3$.

Chapter 6

Mixed Ising-XY Random Magnet: $Fe_xCo_{1-x}TiO_3$

6.1 Introduction

In crystalline magnetic materials, the magnetic moments are arranged on a lattice. In ideal magnets, this lattice structure is characterized by translational invariance. The existence of this invariance often simplifies the theoretical analysis. In random magnets, however, this translational invariance is absent. The fundamental problem in the study of random magnets is to understand the effects of this lack of translational invariance — the randomness — on the magnetic properties. In particular, at the simplest level one would like to understand whether or not there exists a transition out of the high-temperature paramagnetic phase and, if there is a transition, whether it is to a state of conventional magnetic order or to a low-temperature disordered phase not present in uniform magnets.

One version of the random Ising magnet problem — the Random Field Ising Model (RFIM) — has been a subject of intense research for two decades [114, 102]. Fishman and Aharony [115] observed that the physics of the RFIM is closely related to the behavior of a random Ising antiferromagnet in a uniform field. Following this suggestion, a series of experiments (for reviews see Refs. [116, 117, 118, 119]) have been performed on the properties of diluted Ising antiferromagnets in applied mag-

netic fields. These experiments have revealed a number of interesting features, and these features are believed to be the consequences of random staggered magnetic field effects. Specifically, in earlier neutron studies [120, 121, 122, 123], it was found that if the field was applied in the paramagnetic phase, above the Néel temperature T_N, and the sample was then cooled slowly through T_N (this procedure was referred to as field-cooled, or FC), the system evolved continuously from the normal paramagnetic state to a low-temperature microdomain state. Different behavior was, however, observed if the sample was first cooled to low temperatures in the absence of a magnetic field, and the field subsequently applied (this procedure was labeled zero-field-cooled, or ZFC). In this case, the zero field long range magnetic order persisted until the sample was heated above a well-defined field-dependent metastability temperature $T_M(H)$. Recently, with the development of dedicated synchrotron radiation sources, RFIM systems have also been studied in detail with magnetic x-ray scattering techniques. Besides confirming the above-stated hysteresis effects, two very intriguing results emerged. (1) The ZFC transition was found to broaden progressively with increasing magnetic field. The loss of the long range order (LRO) near the transition was well described by a power law with a Gaussian distribution of transition temperatures, of width σ_{ZFC}, and this width σ_{ZFC} increased as H^2. This phenomenon was labeled "*trompe l'oeil* critical behavior" [124, 125]. (2) The apparent discrepancies in the RFIM literatures between the scattering measurements of the order parameter and fluctuations [124, 125] and thermodynamic measurements [126, 127] could be readily reconciled provided that one included the phenomenological term $\frac{dM_s^2}{dT}$ in the interpretation of indirect heat capacity measurements and assumed the "*trompe l'oeil* critical behavior" description for the sublattice magnetization M_s [128]. However, most of the experimental work on the RFIM to-date has been carried out on the diluted Ising antiferromagnets $Mn_xZn_{1-x}F_2$ and $Fe_xZn_{1-x}F_2$. It is therefore clearly of some interest to see how universal these results are, and specially whether alternative realizations of RFIM systems exhibit the same features.

Contemporaneously, significant interest has also been directed toward the effects of quenched randomness in systems with a planar (XY) symmetry; this is partly

stimulated by the relevance of the random field XY model to the problem of the structure of the vortex lattice [129] in type II superconductors, which include the high-T_c superconductors. It is generally agreed that there is no LRO in XY magnets with quenched random fields or random anisotropies in less than four dimensions due to the domain-wall arguments of Imry and Ma [114]. However, the nature of the ground state is not well understood. Some theoretical studies [130, 131] suggest that the low-temperature phase possesses algebraically decaying spin-spin correlations, while others [132, 133] imply a real space spin-spin correlation of the form $e^{-\kappa r}$. Very recently, Gingras and Huse [134] argued that in an XY magnet in the presence of a weak random field, the length scale ξ_v at which the vortices appear is larger than the pinning length ξ_p [114], and that the spin-spin correlation is expected to decay as a power-law for $\xi_p < r < \xi_v$ and exponentially for $r \geq \xi_v$. It is therefore highly desirable to measure experimentally the low temperature spin-spin correlations in an XY magnet with random fields and random anisotropies.

6.2 $Fe_xCo_{1-x}TiO_3$

The crystal structure of both $FeTiO_3$ and $CoTiO_3$ is rhombohedral, space group $C_{3i}^2(R\bar{3})$, with a unit cell (Fig. 6-1(a)) of dimensions $a_0 = 5.54$Å, $\alpha = 54°41$ for $FeTiO_3$, and $a_0 = 5.49$Å, $\alpha = 54°42$ for $CoTiO_3$ [135]. The similarity of the lattice constants ensures that excellent quality random alloys, $Fe_xCo_{1-x}TiO_3$, can be crystallized.

There are two molecules per primitive cell, as shown in Fig. 6-1(a). A triple hexagonal unit cell (Fig. 6-1(b)) is often used to describe the rhombohedral structure. The hexagonal lattice vectors ($\vec{x}_h$, $\vec{y}_h$, $\vec{z}_h$) are related to the rhombohedral ones ($\vec{x}_r$, $\vec{y}_r$, $\vec{z}_r$) by

$$\begin{aligned} \vec{x}_h &= \vec{x}_r - \vec{y}_r, \\ \vec{y}_h &= \vec{y}_r - \vec{z}_r, \\ \vec{z}_h &= \vec{x}_r + \vec{y}_r + \vec{z}_r \end{aligned} \tag{6.1}$$

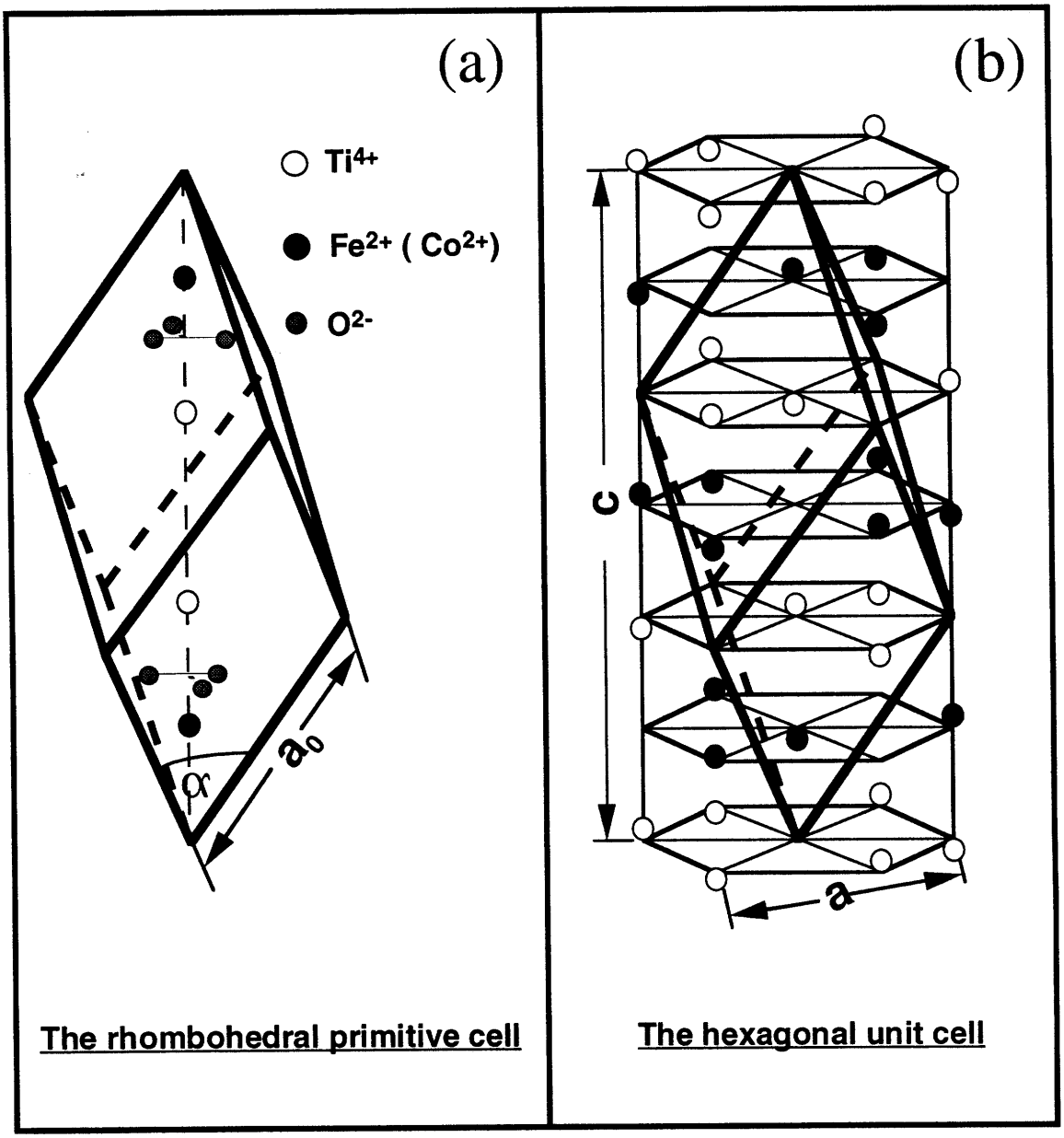

Figure 6-1: Crystal structure of $FeTiO_3$ and $CoTiO_3$. (a) The rhombohedral primitive cell contains two molecules. (b) The hexagonal triple cell contains six molecules.

As illustrated in Fig. 6-1(b), this hexagonal unit cell consists of six molecules. The magnetic interaction between the neighboring magnetic ions (Fe^{2+} or Co^{2+}) in these two titanate compounds are ferromagnetic within the a-b plans of the hexagonal unit cell, and antiferromagnetic along the c-axis direction. [136, 137]. The magnetic ions (Fe^{2+} or Co^{2+}) situate at (0,0,$\pm u$), ($\frac{2}{3}, \frac{1}{3}, \frac{1}{3} \pm u$), ($\frac{1}{3}, \frac{2}{3}, \frac{2}{3} \pm u$). The indices in this and the next chapters are based on the triple hexagonal (chemical) unit cell (Fig. 6-1(b)). The difference between the two magnetic structures is that at low temperatures, the Fe^{2+} spins order along the hexagonal c-axis ($\|$) in $FeTiO_3$ [136], while the Co^{2+} spins in $CoTiO_3$ order in the a-b plane ($\perp$), perpendicular to the c-axis [137]. These anisotropies originate in the crystal-field effects due to the surrounding ions as well as the spin-orbit interaction within the cations themselves. Detailed crystal-field theory calculations on these ground terms exist [138]. The general conclusion is that the Fe^{2+} ion has a triplet ground state and the Co^{2+} ion has a doublet ground state, appropriate to the pseudospin assignment $S^{Fe} = 1$, $S^{Co} = \frac{1}{2}$. The Fe^{2+} and Co^{2+} spins have Ising and XY characters respectively. The magnetic exchange interaction within these ground states can then be described by the diagonal pseudospin Hamiltonian:

$$\mathcal{H} = 2\sum_{ij} \left\{ J_{\|}(ij)\vec{S}_{\|}(i) \cdot \vec{S}_{\|}(j) + J_{\perp}(ij)\vec{S}_{\perp}(i) \cdot \vec{S}_{\perp}(j) \right\}, \tag{6.2}$$

or equivalently,

$$\mathcal{H} = 2\sum_{ij} \left\{ J(ij)\vec{S}(i) \cdot \vec{S}(j) + D(ij) \left[\vec{S}_{\|}(i) \cdot \vec{S}_{\|}(j) - \frac{1}{2}\vec{S}_{\perp}(i) \cdot \vec{S}_{\perp}(j) \right] \right\}, \tag{6.3}$$

where the $\|$ and $\perp$ signs are with respect to the hexagonal c-axis..

The binary compound $Fe_xCo_{1-x}TiO_3$ has been studied in the context of competing spin anisotropies [139, 140]. Similar to $Fe_xCo_{1-x}Cl_2$ [141, 142] and $Fe_xCo_{1-x}Br_2$ [143, 144, 145] it was found to exhibit a tetracritical-like phase diagram with Ising, XY and mixed phases (Fig. 6-2).

In addition, as emphasized by Wong *et al.* [141, 142], the exchange interactions between ions with orbital degeneracy are not necessarily well represented by the

usual Heisenberg form $J(ij)\vec{S}_i \cdot \vec{S}_j$. The charge distribution of these ions is spatially anisotropic; their overlap (exchange) depends not just on whether the spins are parallel or antiparallel but also on the relative orientation of the charge cloud to the displacement vector $\vec{R}_{ij}$. The pseudospin vectors $\vec{S}_i$ and $\vec{S}_j$ are coupled to the charge cloud of the two ions; the electronic exchange interaction is represented by an interaction between $\vec{S}_i$ and $\vec{S}_j$. For the same $\vec{S}_i \cdot \vec{S}_j$, the amount of charge overlap is different for different $\vec{r}_{ij}$ ($\vec{r}_{ij} \equiv \vec{R}_{ij}/|\vec{R}_{ij}|$). In molecular-field approximation there should be three independent components of the molecular field acting on $\vec{S}_i$ in the directions of $\vec{S}_j$, $\vec{r}_{ij}$ and $(\vec{S}_j \times \vec{r}_{ij})$. This should exhaust the possibility of bilinear scalar coupling between $\vec{S}_i$ and $\vec{S}_j$. If the charge clouds are isotropic, the extra terms are unnecessary. For ions with large spin anisotropy, the charge cloud is by necessity anisotropic; hence instead of Eq. 6.3, the Hamiltonian should have the form

$$\mathcal{H} = \sum_{ij} \left\{ J(ij)\vec{S}(i) \cdot \vec{S}(j) + K(ij)[\vec{r}_{ij} \cdot \vec{S}(i)][\vec{r}_{ij} \cdot \vec{S}(j)] + G(ij)[\vec{S}(j) \times \vec{r}_{ij}] \cdot \vec{S}(i) \right\} \quad (6.4)$$

In a pure system, the additional terms may sum to zero by symmetry. However, in a mixed system these symmetry requirements no longer exist. In particular, for a random mixed system we shall expect the local environment to vary from site to site. Therefore the coupling constants $K(ij)$ and $G(ij)$ are site-random. These terms thus serve to generate random anisotropy and random field effects.

In addition, the magnetoelastic coupling between the lattice and the magnetism of the system may induce uniform distortions via coupling terms of the form $M_s^2\delta$, or, in the presence of a magnetic field, staggered distortions via coupling terms of the form $MM_s\delta_s$. Furthermore, discomposition of the magnetic LRO may lead to a breakup into structural domains through the magnetoelastic coupling. These, together with random anisotropy and random field effects, can be extremely important in understanding mixed random magnets, as the results reported here illustrate.

The phase behavior in $Fe_xCo_{1-x}TiO_3$ is thus the result of the collective effects of fixed and random anisotropies and magnetoelastic coupling as noted above, with both random field and random anisotropy effects perturbing Ising, XY and mixed phases.

This yields a rich phase diagram in the concentration (x) versus temperature (T) plane. Fig. 6-2 is the phase diagram from Ref. [140] revised with two results from this study: (1) the low temperature phase at low Fe^{2+} concentration (the area bounded by line AB and BD) is found to lack LRO, instead, it is a $\vec{S}_{\perp}$ domain-state; (2) the line AB that separates the two disordered phases — paramagnet and $\vec{S}_{\perp}$ domain-state — is a novel *critical* line in the sense that the correlation length diverges on the line and yet there is no transition to LRO involved in this phase transition.

In the next two Chapters, we present the results from synchrotron x-ray scattering studies of the mixed Ising-XY magnetic system with quenched randomness: $Fe_xCo_{1-x}TiO_3$, with Chapter 7 emphasizing the XY behavior, and Chapter 8 devoting to the behavior of the Ising spin component in external magnetic fields.

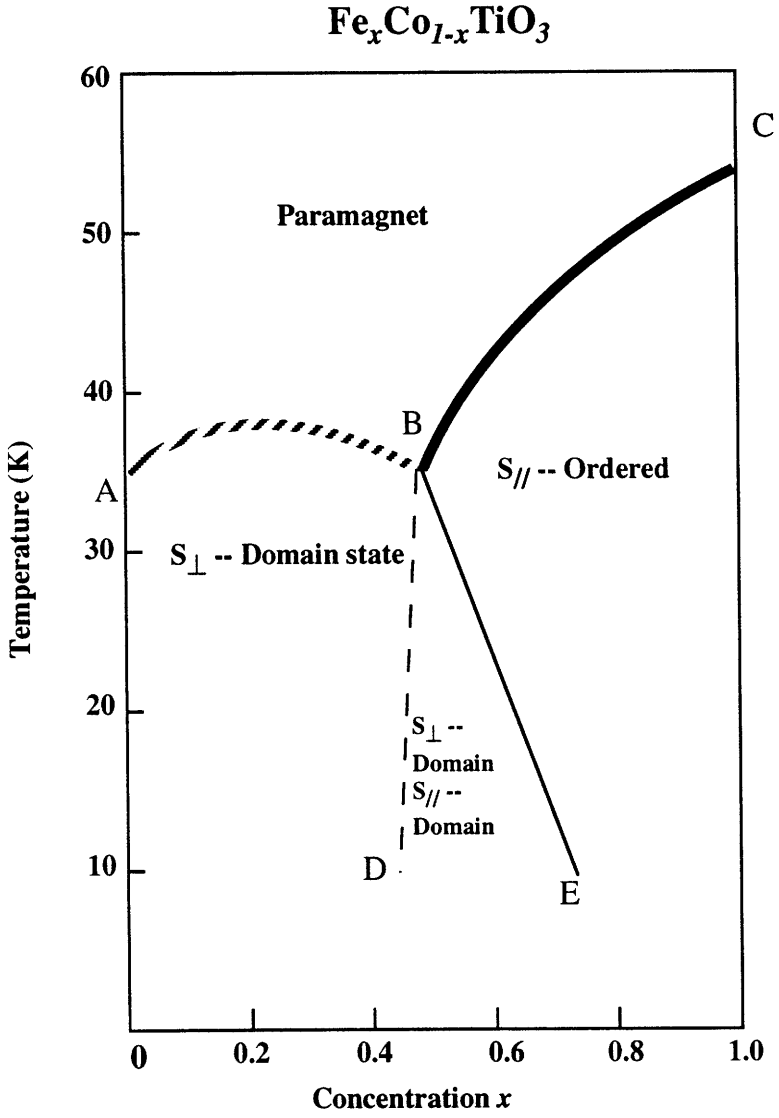

Figure 6-2: The magnetic phase diagram of the crystalline binary compound $Fe_xCo_{1-x}TiO_3$ in the concentration (x) versus temperature (T) plane (from Ref. [140] revised with the two results from this work). There exist four phases: paramagnet, $S_{||}$-ordered antiferromagnet, $\vec{S}_\perp$-domain state, and the mixed domain state, in which both the $\vec{S}_\perp$ and $S_{||}$ form short-range ordered domain states.

Chapter 7

Random Anisotropy and Random Field Effects in XY Magnets with Quenched Randomness

7.1 Experimental Specifications

The experiments were carried out on the beamline X20A at NSLS. The incident wavelength was set at $\lambda = 1.305$Å (E = 9.5 KeV). The penetration depth at this wavelength for $Fe_xCo_{1-x}TiO_3$ was typically $\sim 2\mu m$. The diffraction occurred in the reflection geometry in the vertical scattering plane and a flat Ge(111) crystal was used as the analyzer. The excellent quality single crystals of $Fe_xCo_{1-x}TiO_3$ were kindly made available by Dr. A. Ito of Ochanomizu University, Japan. The samples studied in the second half of this thesis (Chapter 7 and Chapter 8) are identical to the ones Ito *et al.* studied with neutron scattering techniques in Ref. [139, 140]. The samples were mounted on the cold finger of a closed cycle refrigerator. The temperature stability was within 10mK in the course of a scan.

The sublattice magnetization measurements were carried out around the magnetic-superlattice positions $(0, 0, 4.5)$ and $(1, 1, 1.5)$. Following Ref. [25, 146], the magnetic

x-ray intensity is given by

$$I_M \sim Tr[< M_m > \rho < M_m >^{\dagger}], \tag{7.1}$$

where Tr denotes the trace operator, ρ is a 2×2 density matrix for the incident polarization state, given by

$$\rho = \begin{pmatrix} P^{\perp} & 0 \\ 0 & P^{\parallel} \end{pmatrix},$$

where the supscripts $\parallel$ and $\perp$ indicate the directions that are parallel and perpendicular to the scattering plane, and the matrix $< M_m >$ is

$$< M_m >= \begin{pmatrix} (\sin 2\theta) S_{\mathrm{V}} & -2\sin^2\theta[(L_{\mathrm{T}} + S_{\mathrm{T}})\cos\theta - S_{\mathrm{L}}\sin\theta] \\ 2\sin^2\theta[(L_{\mathrm{T}} + S_{\mathrm{T}})\cos\theta - S_{\mathrm{V}}\sin\theta] & \sin 2\theta[2(\sin^2\theta)L_{\mathrm{V}} + S_{\mathrm{V}}] \end{pmatrix},$$

where the subscripts L and T denote the directions that are longitudinal and transverse to the momentum transfer $\vec{\mathrm{Q}}$ within the scatteing plane, while the subscript V denotes the direction perpendicular to the scattering plane. The magnetic x-ray intensities at the magnetic-superlattice positions $(0, 0, 4.5)$ and $(1, 1, 1.5)$ therefore are:

$$\begin{aligned} I_{(0,0,4.5)} &\propto 0.5|\vec{\mathrm{S}}_{\perp}|^2 \\ I_{(1,1,1.5)} &\propto 0.93|\mathrm{S}_{\parallel}|^2 + 0.036|\vec{\mathrm{S}}_{\perp}|^2 + 0.038|\vec{\mathrm{S}}_{\perp} + \vec{\mathrm{L}}_{\perp}|^2. \end{aligned} \tag{7.2}$$

where the subscripts $\parallel$ and $\perp$ are the directions along the hexagonal c-axis and within the a-b plane, respectively. In reaching Eq. 7.2, we made use of $\theta_{(0,0,4.5)} \simeq 12°$ and $\theta_{(1,1,1.5)} \simeq 16°$ (for incident x-ray wavelength $\lambda = 1.305$Å). In the spin-only approximation, the ratio between the contribution of $\vec{\mathrm{S}}_{\perp}$ to $I(1, 1, 1.5)$, $I_{\perp}(1, 1, 1.5)$, and its contribution to $I(0, 0, 4.5)$, $I_{\perp}(0, 0, 4.5)$, is

$$\frac{I_{\perp}(1,1,1.5)}{I_{\perp}(0,0,4.5)} \sim \left(\frac{\sin 2\theta_{(1,1,1.5)}}{\sin 2\theta_{(0,0,4.5)}} \frac{f_{(1,1,1.5)}}{f_{(0,0,4.5)}}\right)^2 \frac{0.074}{0.5} \sim 0.2, \tag{7.3}$$

for $\lambda = 1.305$Å, where f denotes the magnetic form factor, and $\frac{f_{(1,1,1.5)}}{f_{(0,0,4.5)}} \sim 0.88$ when $\lambda = 1.305$Å.

7.2 Results and Data Analysis

7.2.1 $Fe_{0.35}Co_{0.65}TiO_3$

Our first effort was to study the XY ordering in $Fe_{0.35}Co_{0.65}TiO_3$. According to earlier neutron scattering studies [140], only the XY spin component $\vec{S}_\perp$ orders in $Fe_{0.35}Co_{0.65}TiO_3$, while the Ising spin component $S_\parallel$ does not order, at least for temperatures higher than 7K.

In Fig. 7-1, we show transverse scans at the magnetic-reciprocal lattice position $(0, 0, 4.5)$ for several temperatures. As noted early, the magnetic intensity at $(0, 0, 4.5)$ is proportional to $|\vec{S}_\perp|^2$. The scattering intensity at $(0, 0, 4.5)$ therefore reflects the magnetic structure of the XY spin component $\vec{S}_\perp$ along the hexagonal c-axis direction. In Fig. 7-1, as the temperature is lowered, the scattering profile broadens with an increasing peak intensity.

This broadening is detailed in Fig. 7-2, where we show the temperature dependence of the peak intensity, the in-plane transverse HWHM and the longitudinal HWHM of the magnetic reflection $(0, 0, 4.5)$ for $Fe_{0.35}Co_{0.65}TiO_3$. At the transition temperature, $T_\perp(x = 0.35) = 36.89(3)$K, there is a sudden rise of the scattering intensity (Fig. 7-2(a)), indicating the onset of the ordering of the spin component $\vec{S}_\perp$. Immediately following the onset of this ordering, the reflection profile broadens progressively with decreasing temperature in both the longitudinal and transverse directions (Fig. 7-2(b) & (c)). For temperatures below $T_\perp(x = 0.35)$, the spin component $\vec{S}_\perp$ starts to order, but instead of achieving LRO, it forms finite size clusters — albeit with a very large length scale — along the hexagonal c-axis, and the size of these clusters becomes *smaller* with decreasing temperature. We note that thermal disordering effects become less important as one lowers the temperature. This therefore exemplifies the domination of the quenched disorder over the thermal disorder at lower temperatures

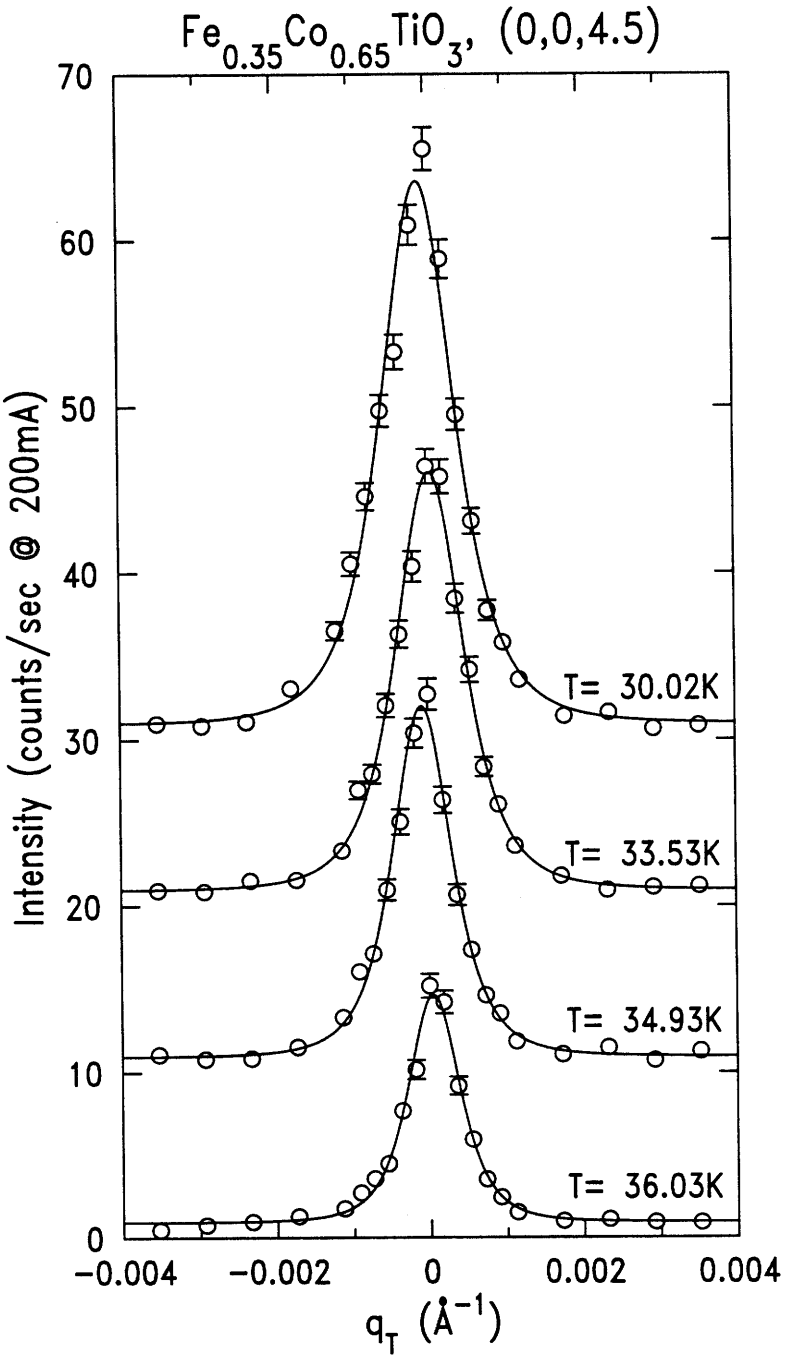

Figure 7-1: Representative scans along the transverse direction at the magnetic-superlattice position $(0, 0, 4.5)$ for $Fe_{0.35}Co_{0.65}TiO_3$.

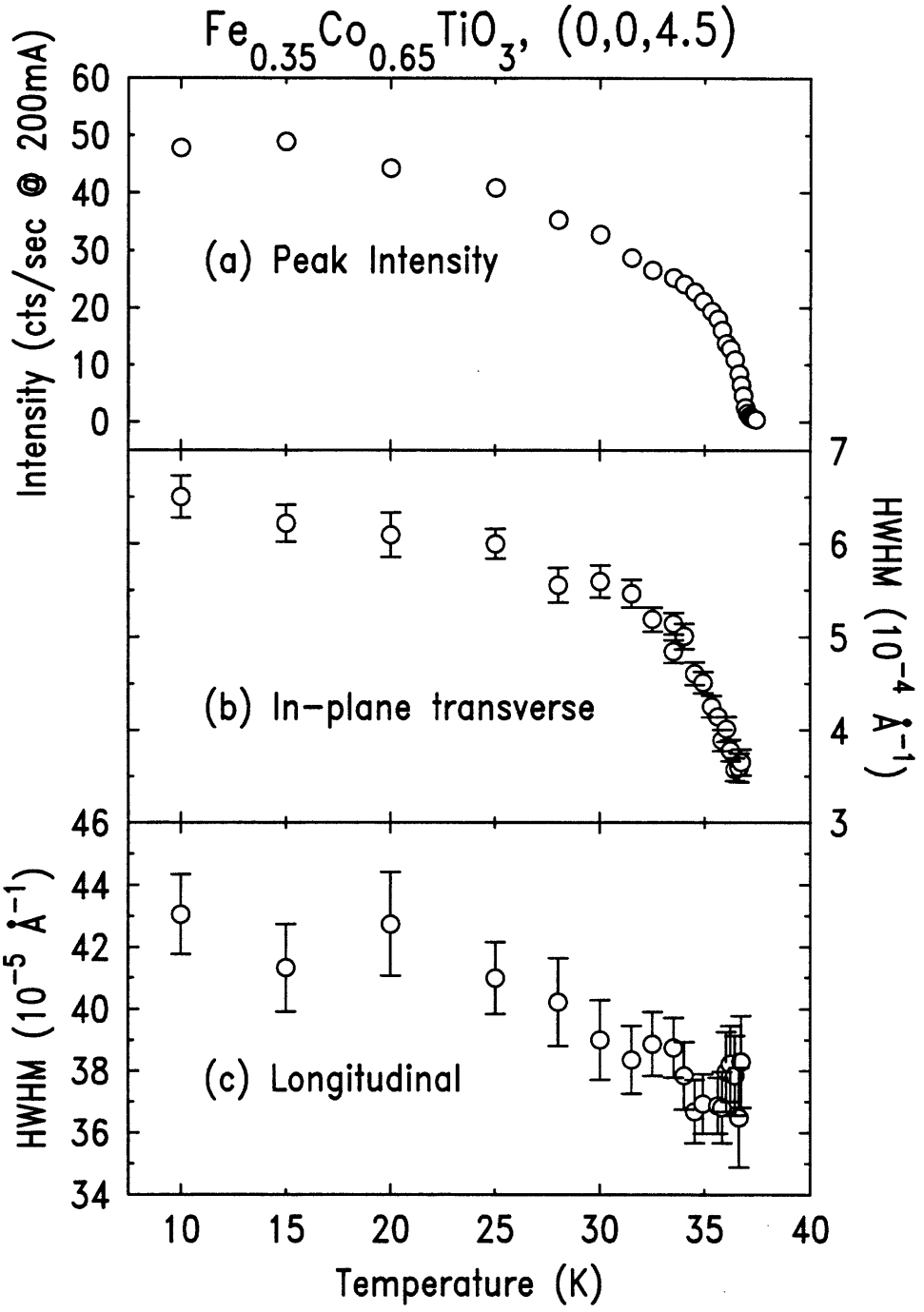

Figure 7-2: The temperature dependence of the peak intensity(a), the transverse HWHM(b) and the longitudinal HWHM(c) at the magnetic-superlattice reflection $(0, 0, 4.5)$ for $Fe_{0.35}Co_{0.65}TiO_3$.

in random systems.

In Fig. 7-3, we plot the intensity, the transverse and the longitudinal HWHM of the charge reflection $(0, 0, 6)$, which reflects the electronic structure (the atomic structure) along the hexagonal c-axis direction. For temperatures higher than the XY ordering temperature $T_\perp(x = 0.35)$, when the magnetic scattering intensity at $(0, 0, 4.5)$ is zero (Fig. 7-2(a)), the charge scattering profile at $(0, 0, 6)$ is independent of temperature, and resolution-limited. However, as soon as the sample is cooled below $T_\perp$, when the finite size magnetic clusters start to appear, there follows a broadening of the charge reflection profile, along both the longitudinal and the transverse directions, indicating the breakup into structural domains following the onset of the (short-range) ordering of the XY spin component $\vec{S}_\perp$. The more pronounced broadening along the transverse direction in both Fig. 7-2 and Fig. 7-3 reflects the effects of mosaicity, as elucidated later in this Chapter.

Fig. 7-4 summarizes the alteration of the magnetic and atomic structure along the hexagonal c-axis following the short-range ordering of the XY spin component $\vec{S}_\perp$. In Fig. 7-4, we plot the integrated intensity of the magnetic reflection $(0, 0, 4.5)$, along with the in-plane transverse HWHM of the charge reflection $(0, 0, 6)$, as a function of temperature. As noted above, the $(0, 0, 6)$ broadening along the transverse direction primarily reflects the effects of mosaicity. This mosaicity effect scales linearly with the magnetic integrated intensity of $(0, 0, 4.5)$, which, in turn, is well described by a simple power law,

$$I(0, 0, 4.5) \propto |\vec{S}_\perp|^2 \propto \left(1 - \frac{T}{T_\perp(x = 0.35)}\right)^{2\beta_\perp} \tag{7.4}$$

near the transition temperature $T_\perp(x = 0.35) = 36.89(3)$K. The best fit value of $\beta_\perp$ is 0.35(2), in quantitative agreement with the theoretical result $\beta_{XY} = 0.36$ for a 3D planar (XY) magnet [1]. However, the low temperature phase in this case is by no means an ordinary ordered state. Instead, it contains both magnetic and structural domains.

So far, we have been concentrating on the magnetic and atomic structures along

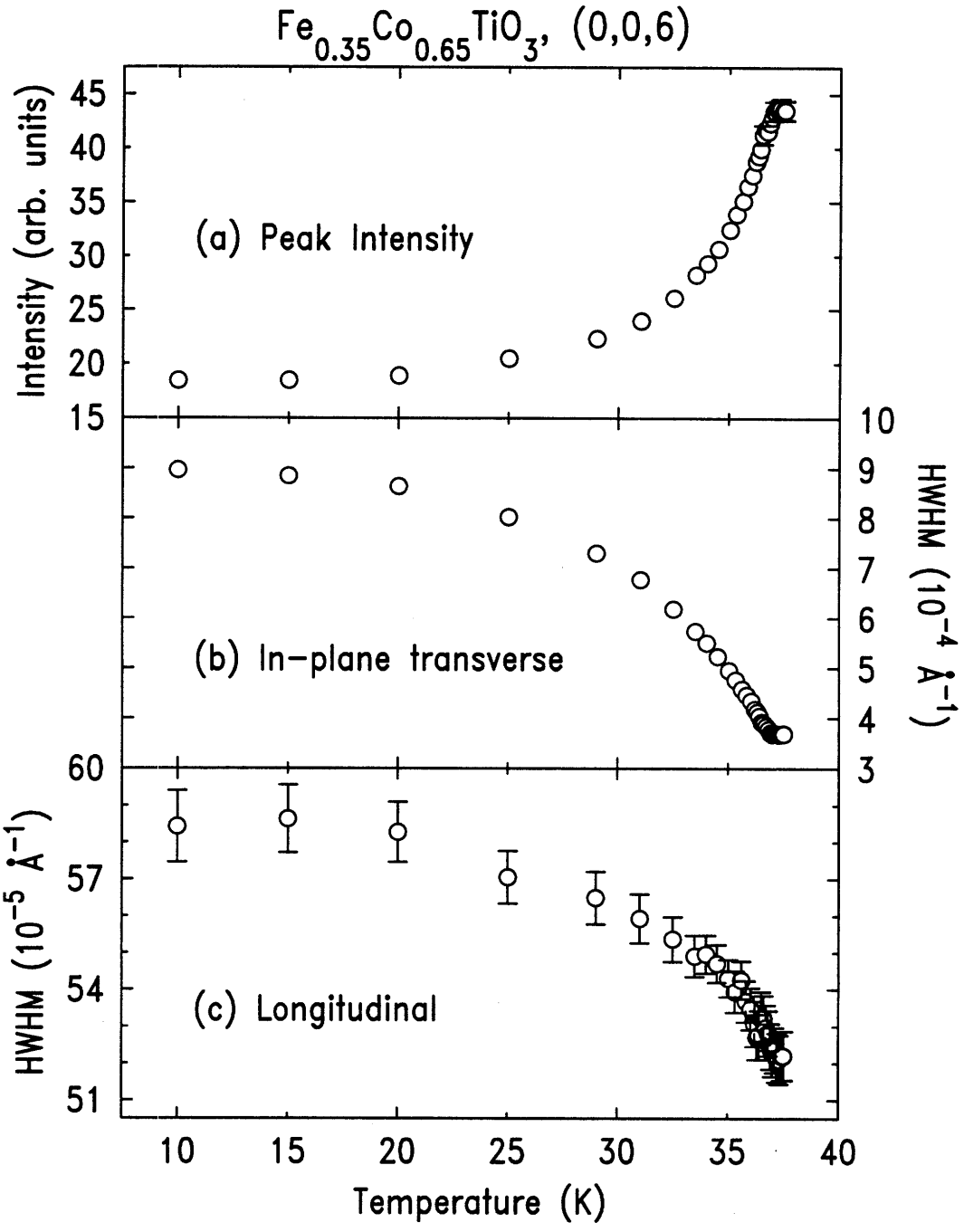

Figure 7-3: The temperature dependence of the peak intensity(a), the transverse HWHM(b), and the longitudinal HWHM(c) at the structural reflection $(0, 0, 6)$ for $Fe_{0.35}Co_{0.65}TiO_3$.

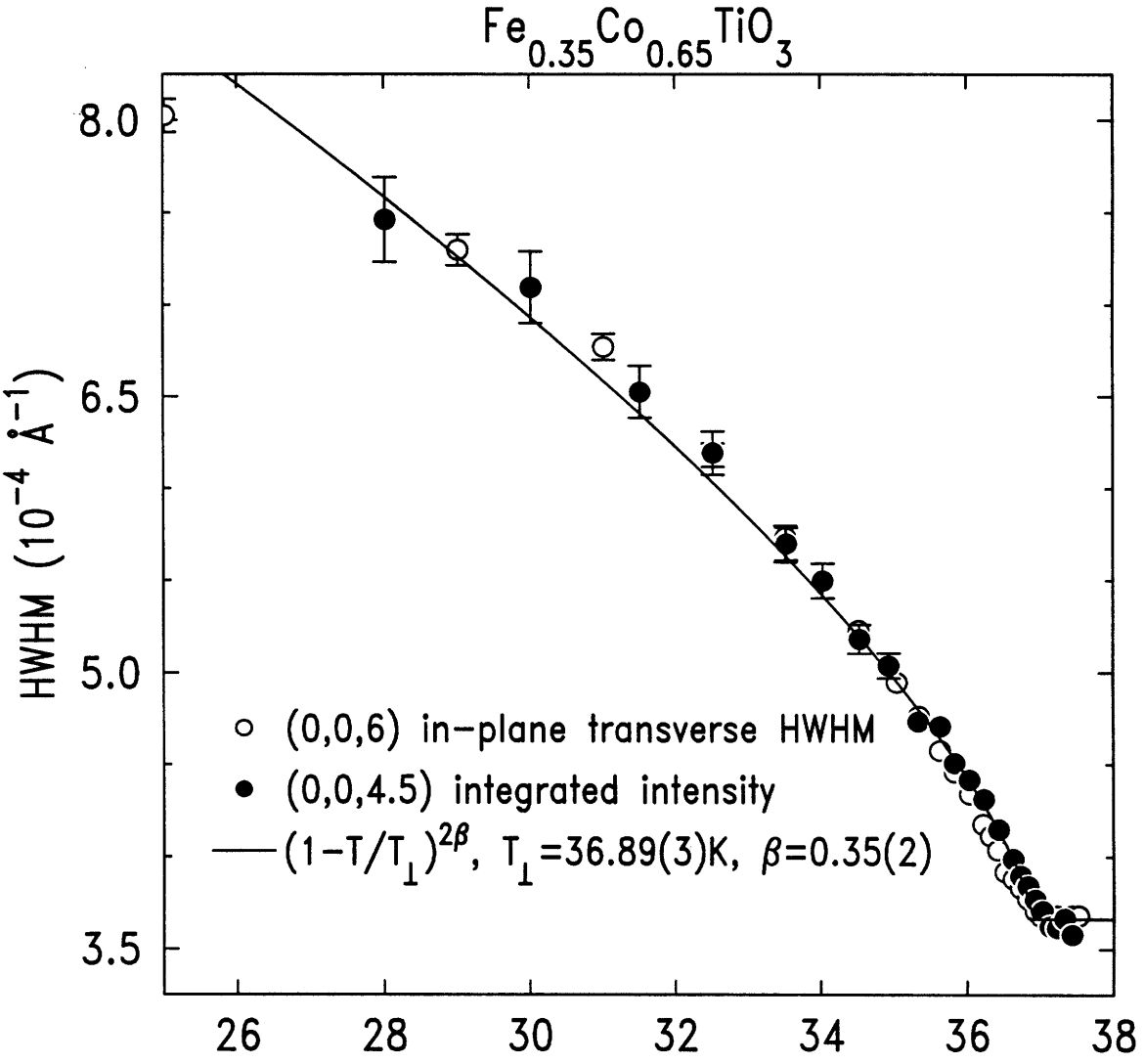

Figure 7-4: The temperature dependence of the in-plane transverse HWHM of the charge reflection (0,0,6) (unfilled circles), and the integrated intensity of the magnetic reflection (0,0,4.5) (filled circles) for $Fe_{0.35}Co_{0.65}TiO_3$.

the c-axis direction. But what happens within the hexagonal a-b plane following the short-range ordering of the XY spin component? In Fig. 7-5, we plot both the longitudinal and the transverse scans at the reciprocal lattice point $(1,1,0)$ for temperatures $T = 10.00$K (filled circles) and $T = 37.73$K (unfilled circles), which respectively reflects the atomic structure in the a-b plane before and after the establishment of the short-range order (SRO) of the XY spin component $\vec{S}_\perp$. Above the transition temperature $T_\perp$, the scattering profile at $(1,1,0)$ is independent of temperature, and resolution limited. The data are well described by the following form:

$$I \sim \frac{1}{\left\{1+\left[(q_{\rm L}-q_{\rm L}^0)/w_{\rm L}\right]^2\right\}^3 \left\{1+\left[(q_{\rm T}-q_{\rm T}^0)/w_{\rm T}\right]^2\right\}^2} \tag{7.5}$$

with $w_{\rm L} = 0.000923\text{Å}^{-1}$, and $w_{\rm T} = 0.000356\text{Å}^{-1}$. The subscripts L and T represent directions that are longitudinal and transverse to $(1,1,0)$ within the scattering plane, specifically, the subscript L denotes the direction along $(h,h,0)$, while the subscript T denotes the direction along $(h,-h,0)$. Eq. 7.5 with the parameters given above is therefore the experimentally measured resolution function at the reciprocal lattice point $(1,1,0)$. The value $w_{\rm L} = 0.000923\text{Å}^{-1}$ is consistent with theoretical expectations for the longitudinal resolution of a vertical synchrotron-x-ray scattering geometry using Ge(111) crystals as both monochromator and analyzer. The transverse resolution was controlled by the sample mosaicity. The value $w_{\rm T} = 0.000356\text{Å}^{-1}$ corresponds to a mosaicity of 0.01°. The dashed line in Fig. 7-5 is the result of a least-squares fit of the data for $T = 37.73$K to Eq. 7.5.

Below the transition temperature $T_\perp$, the scattering profile at $(1,1,0)$ broadens significantly along both the longitudinal and transverse directions. This broadening is consistent with a lattice distortion depicted in Fig. 7-6. Before the distortion, there exists a sixfold symmetry within the a-b plane, specifically, the following six reciprocal lattice vectors are equivalent: $\vec{Q}_{(1,1,0)}$, $\vec{Q}_{(2,-1,0)}$, $\vec{Q}_{(-1,2,0)}$, $\vec{Q}_{(-1,-1,0)}$, $\vec{Q}_{(-2,1,0)}$ and $\vec{Q}_{(1,-2,0)}$. However, after the distortion, these six reciprocal lattice points are no

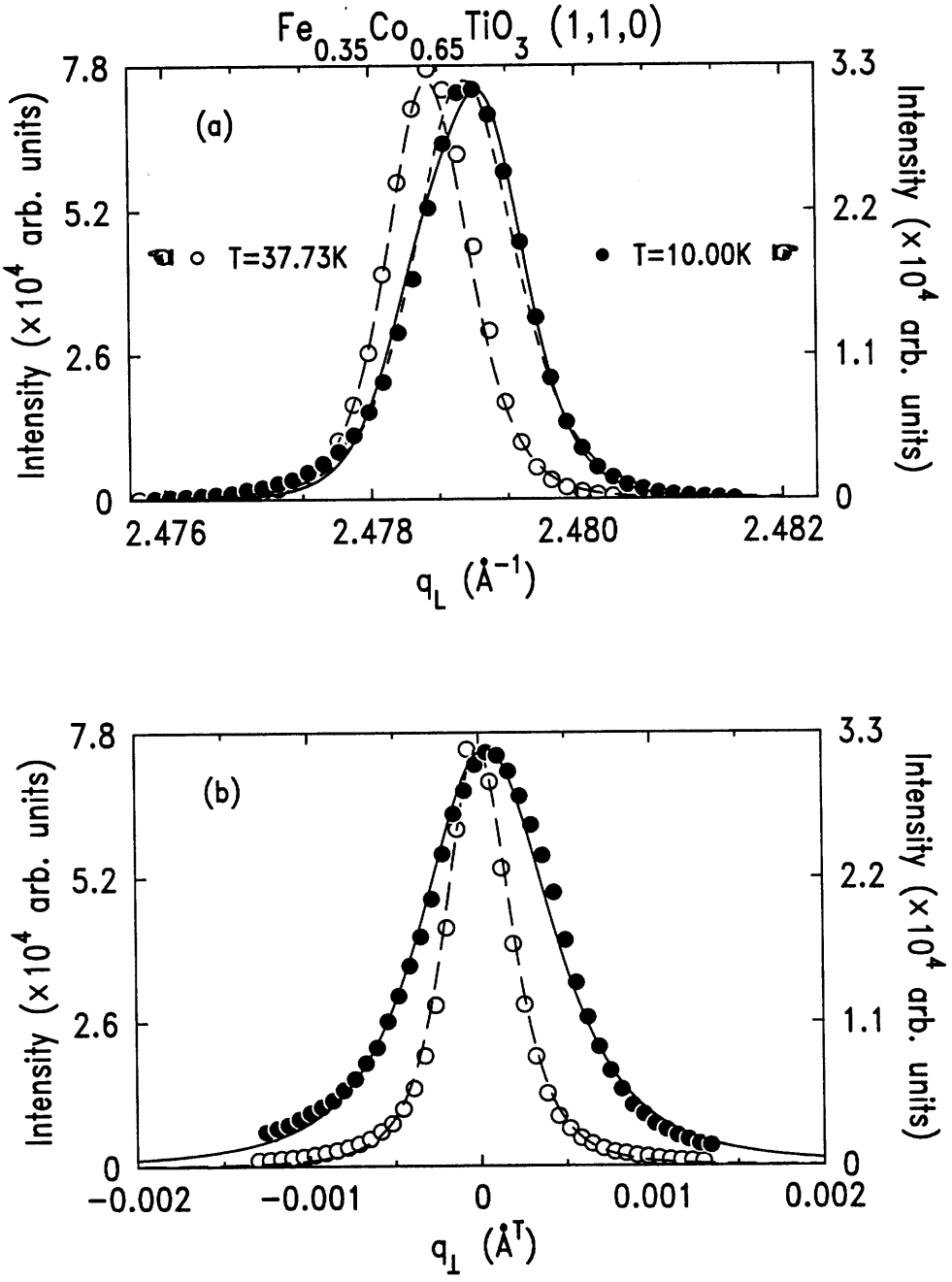

Figure 7-5: The longitudinal and the transverse scans at the reciprocal lattice point $(1, 1, 0)$ for temperatures $T = 10.00$K (filled circles) and $T = 37.73$K (unfilled circles).

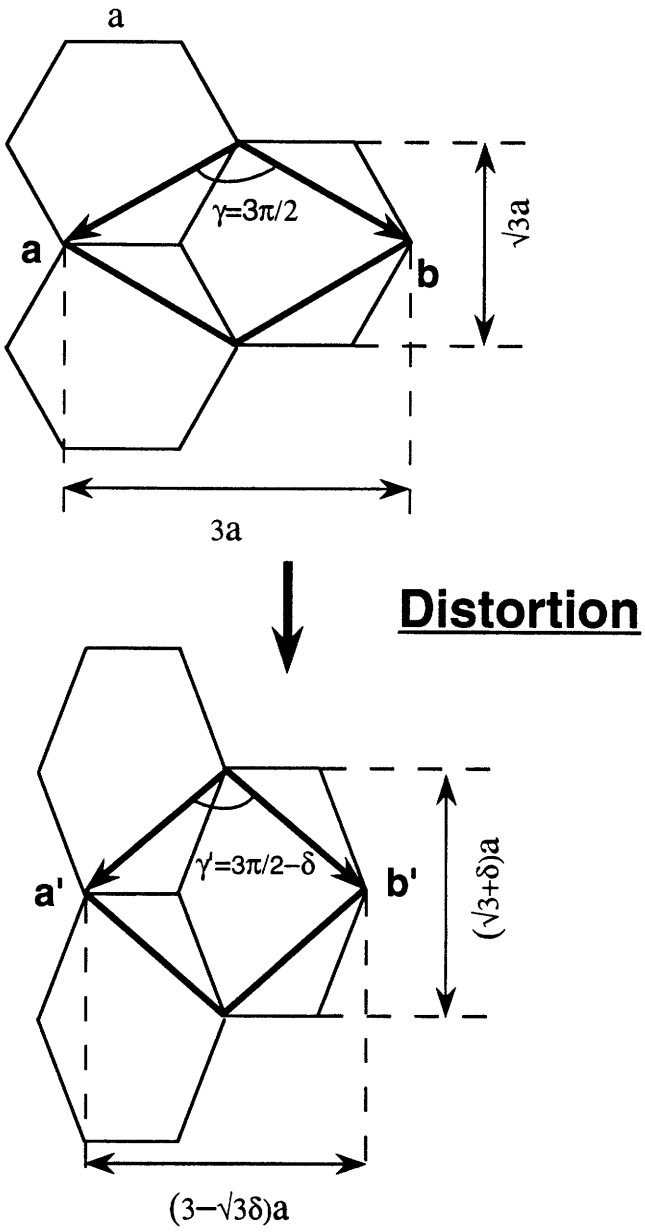

Figure 7-6: The distortion of the lattice in the hexagonal a-b plane following the short range ordering of the XY spin component $\vec{S}_{\perp}$.

longer equivalent, in particular,

$$\begin{aligned} |\vec{Q}_{(1,1,0)}| = |\vec{Q}_{(-1,-1,0)}| &= Q_0(1 - \frac{\delta}{\sqrt{3}}), \\ |\vec{Q}_{(-2,1,0)}| = |\vec{Q}_{(1,-2,0)}| = |\vec{Q}_{(2,-1,0)}| = |\vec{Q}_{(-1,2,0)}| &= Q_0(1 + \frac{\delta}{2\sqrt{3}}). \end{aligned} \tag{7.6}$$

The difference $\Delta Q \equiv |\vec{Q}_{(1,1,0)}| - |\vec{Q}_{(2,-1,0)}|$ is proportional to the distortion δ. The solid line in Fig. 7-5(a) is the result of fitting the longitudinal data of $T = 10.00$K to the function form,

$$I \sim \frac{1}{\left\{1 + [(q_{\rm L} - q_{\rm L}^0)/w_{\rm L}]^2\right\}^3} + \frac{y}{\left\{1 + [(q_{\rm L} - (q_{\rm L}^0 + \Delta Q)/w_{\rm L}]^2\right\}^3} \tag{7.7}$$

with $w_{\rm L}$ fixed at the value for the resolution, 0.000923 Å^{-1}. The coefficient y is fixed at 0.5, assuming the six equivalent domains are equally populated in the sample. The best fit value of $|\Delta Q|$ for $T = 10.00$K is 0.00061(5) Å^{-1}, which corresponds to a lattice distortion $\delta \simeq 0.0003$. Clearly, the broadening along the longitudinal direction at $(1, 1, 0)$ is well accounted for by this lattice distortion, which is presumably induced by the magnetoelastic coupling. We note that the broadening of the longitudinal scattering profile can also be satisfactorily described by the finite size effect. The dashed line for data of $T = 10.00$K is the result of a least-squares fit of the data to a Lorentzian squared cross-section convoluted with the resolution function. However, we shall see later in this Chapter that, although both lattice distortion and finite size effects contribute to the broadening of the longitudinal scattering profile, it is the former that plays the more important role.

The broadening along the transverse direction in Fig. 7-5(b) therefore reflects the corresponding twinning arising from the lattice distortion. This twinning effect is of the order of δ. Quantitative information regarding the broadening along the transverse direction, however, depends on the details of the twinning. The solid line in Fig. 7-5(b) is the best fit of the data at $T = 10.00$K to a Lorentzian squared

(twinning)

$$I \sim \frac{1}{\left\{1 + [(q_{\rm T} - q_{\rm T}^0)/\kappa_{\rm T}]^2\right\}^2} \tag{7.8}$$

convoluted with the resolution function. The twinning angle at $T = 10.00$K is given by $\delta\theta \equiv \kappa_{\rm T}/|\vec{\rm Q}_{(1,1,0)}| \sim 0.01°$.

In Fig. 7-7, we plot the temperature dependence of ΔQ and $\kappa_{\rm T}$. Clearly, in order to resolve the small values of ΔQ for temperatures near the transition temperature, higher resolution measurements are needed.

Since the component in the hexagonal a-b plane does not order in $Fe_{0.35}Co_{0.65}TiO_3$ [140], the magnetic x-ray intensity at both the magnetic-superlattice reflection points $(0, 0, 4.5)$ and $(1, 1, 1.5)$ arises from the ordering of the component along the hexagonal c-axis. For the purpose of calibrating the ratio $\frac{I_\perp(1,1,1.5)}{I_\perp(0,0,4.5)}$, we measured the magnetic x-ray intensity at the reciprocal lattice point $(1, 1, 1.5)$, and it was found that for the $x = 0.35$ sample,

$$\frac{I_\perp(1,1,1.5)}{I_\perp(0,0,4.5)} \sim \frac{I(1,1,1.5)}{I(0,0,4.5)} \sim 0.4. \tag{7.9}$$

This may be compared with the spin-only value of 0.2. This discrepancy in the ratio $\frac{I_\perp(1,1,1.5)}{I_\perp(0,0,4.5)}$ reflects the effect of the orbital moment $L_\perp$ as well as the details of the crystal shape.

7.2.2 $Fe_{0.50}Co_{0.50}TiO_3$

Similar to the situation in $Fe_{0.35}Co_{0.65}TiO_3$, both the magnetic and the atomic structures along the hexagonal c-axis direction are found to break into domains following the (short-range) ordering of the XY spin component $\vec{\rm S}_\perp$. In Fig. 7-8, we plot the integrated intensity of the magnetic-superlattice peak $(0, 0, 4.5)$ (top panel), and the transverse HWHM of the structural peak $(0, 0, 6)$ (bottom panel). The broadening of the structural peak $(0, 0, 6)$ along the transverse direction, which is dominated by mosaicity, is found to follow the growth of the magnetic intensity near the transition temperature (cf. Fig. 7-4). However, contrary to the sharp growth of the magnetic intensity and the transverse HWHM in $Fe_{0.35}Co_{0.65}TiO_3$, the transition is "rounded"

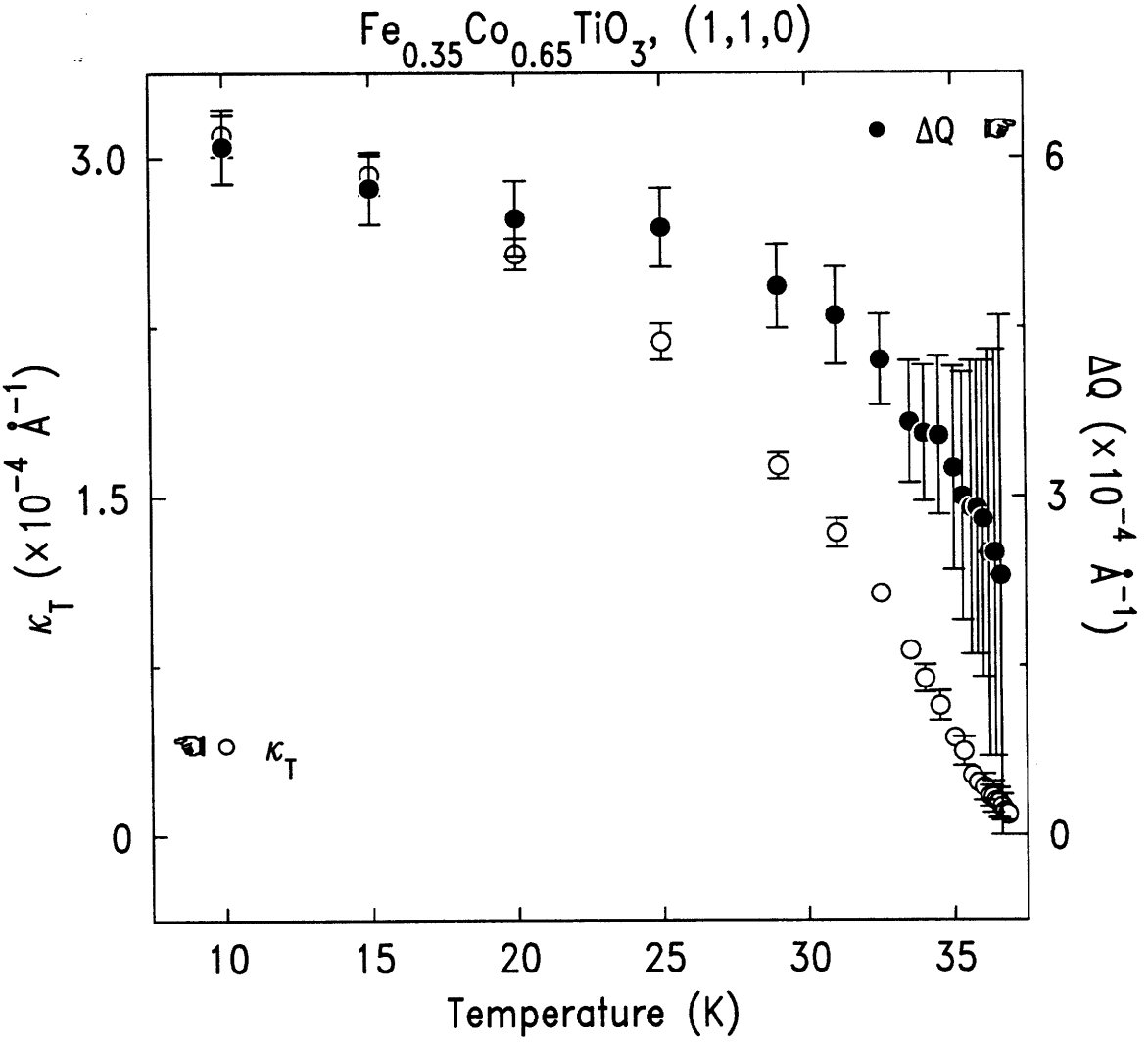

Figure 7-7: The temperature dependence of ΔQ(unfilled circles) and κ_T(filled circles) for $Fe_{0.35}Co_{0.65}TiO_3$.

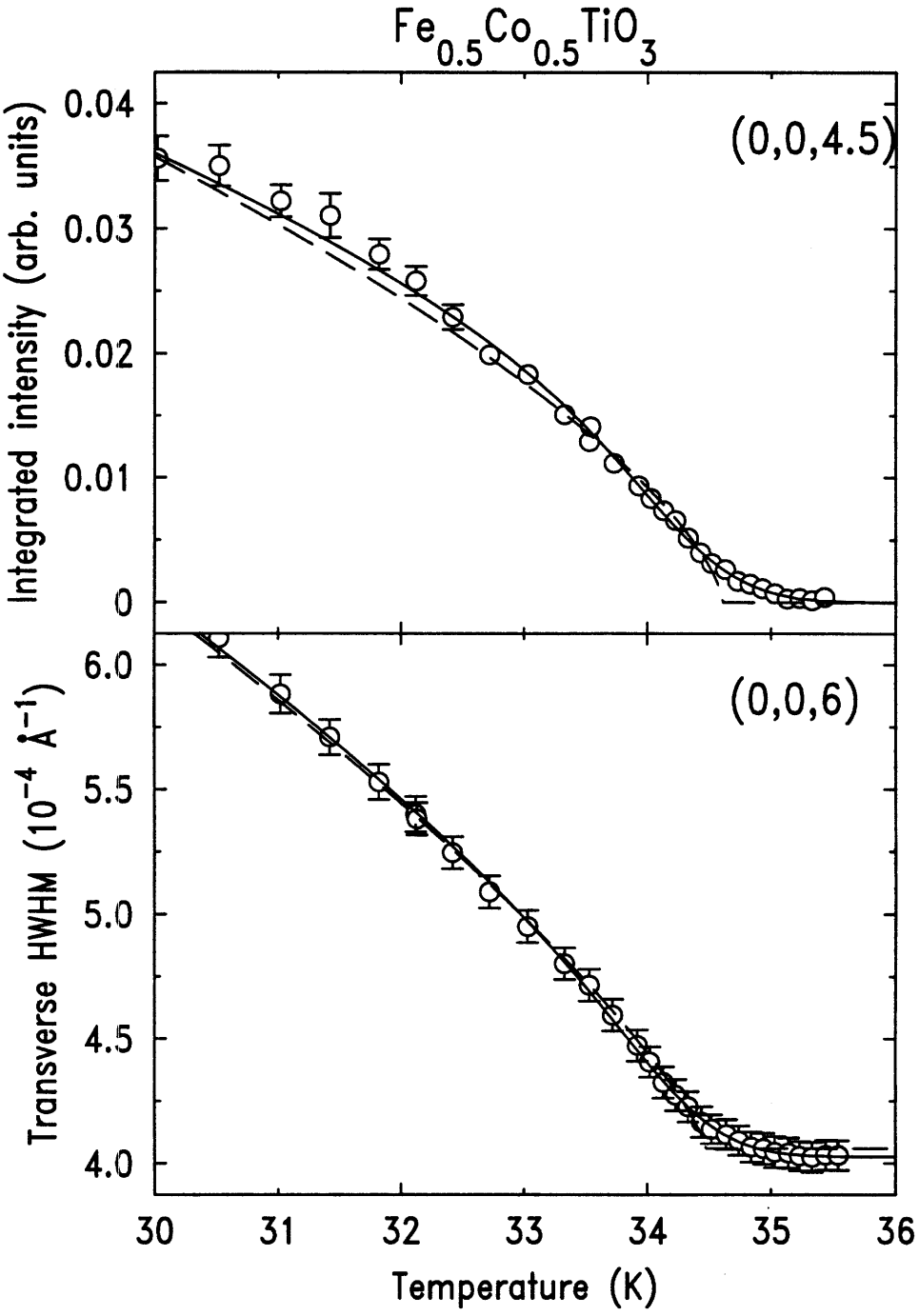

Figure 7-8: The integrated magnetic intensity at $(0, 0, 4.5)$(top panel) and the transverse HWHM of the structural reflection $(0, 0, 6)$(bottom panel) as functions of temperature.

in $Fe_{0.50}Co_{0.50}TiO_3$. The dashed lines in Fig. 7-8 are the results of least-squares fits of the data to a simple power law, $I \sim \left(1 - \frac{T}{T_\perp(x=0.50)}\right)^{2\beta_\perp}$. Clearly the power law does not describe the data near the transition very well, and specifically, the data exhibit significant rounding near the transition. We therefore fit the data to a "rounded" power law:

$$I = \frac{I_0}{\sqrt{\pi}\delta T_c} \int \left(\frac{t-T}{t}\right)^{2\beta_\perp} \exp\left(-\left(\frac{t-T_c}{\delta T_c}\right)^2\right) dt. \tag{7.10}$$

This is a power law with a Gaussian distribution of transition temperatures. Given that we do not have compelling physical explanation for this broadening, we postulate that this spread of $T_\perp$ results simply from sample concentration gradients. It is important to note that although the functional form of Eq. 7.10 is also used in describing the loss of LRO on warming from the ZFC state of the RFIM magnets, the broadening in RFIM, however, has a completely different origin (see Refs. [124, 125, 128]). The fit parameters from the magnetic integrated intensity at $(0, 0, 4.5)$ and the transverse HWHM of the charge peak $(0, 0, 6)$ are identical, within the error bars, and they are: the peak of the (transition temperature) Gaussian distribution $T_c = 34.40(5)$K, the spread of T_c, $\delta T_c = 0.75(5)$K, and the exponent $\beta_\perp = 0.32(5)$. The solid lines in Fig. 7-8 are the results from fitting the data to Eq. 7.10. The transition temperature $T_\perp(x = 0.50) = 34.4(8)$K therefore has a large error bar due to the concentration gradients in the illuminated volume.

In Fig. 7-9, we plot the integrated intensity, the longitudinal and the transverse HWHM of the magnetic-superlattice reflection $(1, 1, 1.5)$ as functions of temperature. The integrated intensity of $(1, 1, 1.5)$ is well described by a simple power law, $\left(1 - \frac{T}{T_\perp}\right)^{2\beta_\perp}$, with the best fit values for $\beta_\perp$ being 0.34(4), and the transition temperature, $T_\perp = 33.7(2)$K, in good agreement with the values deduced from the magnetic reflection $(0, 0, 4.5)$. In addition, the ratio between the magnetic x-ray intensities at the reciprocal lattice points $(1, 1, 1.5)$ and $(0, 0, 4.5)$, $\frac{I(1,1,1.5)}{I(0,0,4.5)} \sim 0.3$, is consistent with the anticipated relative intensity assuming that only the $\perp$ component orders in $Fe_{0.50}Co_{0.50}TiO_3$. Any significant ordering of the $\parallel$ component should have reflected itself in the magnetic x-ray intensity at $(1, 1, 1.5)$. Furthermore, both the

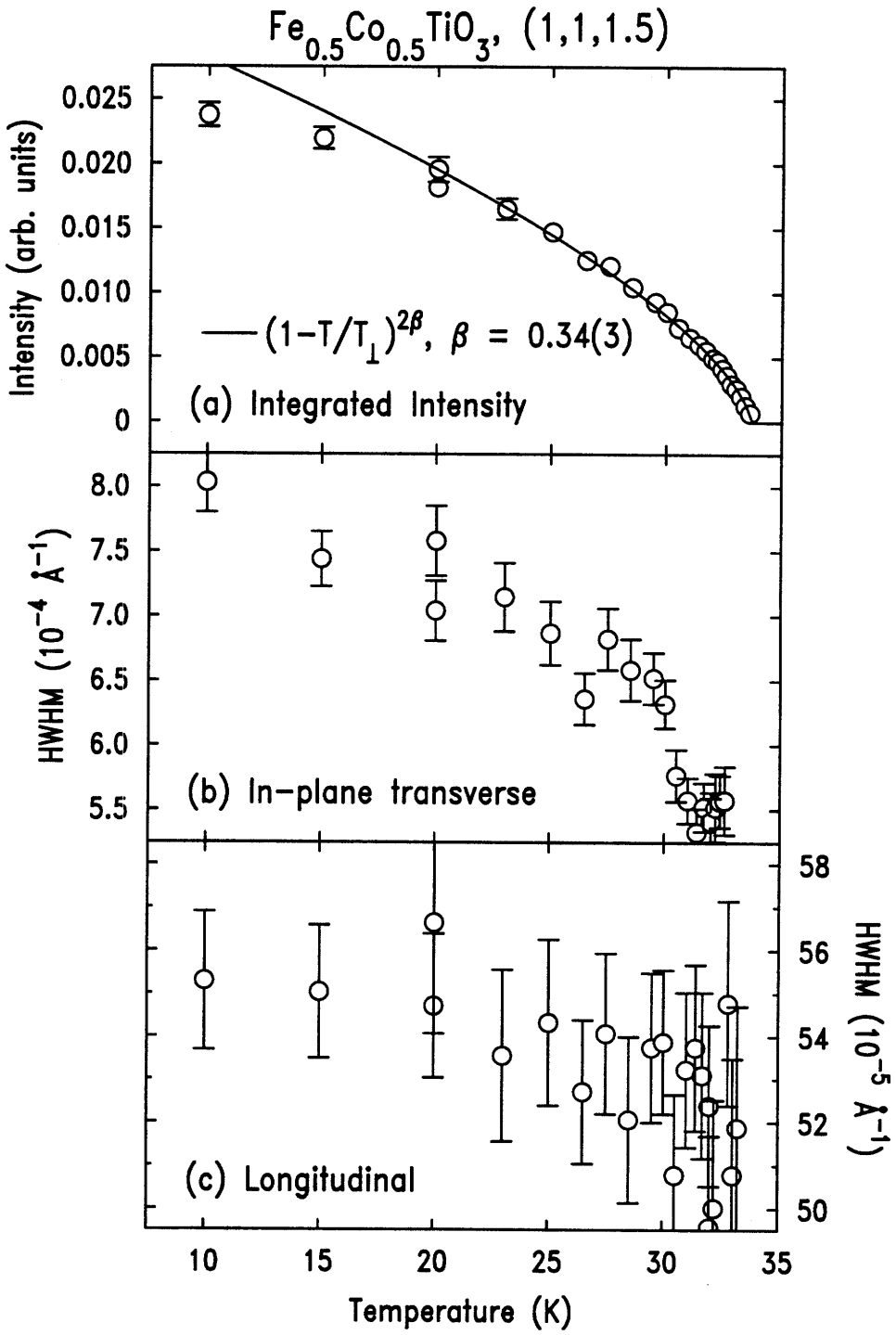

Figure 7-9: The temperature dependence of the integrated intensity(a), the transverse(b) and the longitudinal(c) HWHM at the magnetic-superlattice position $(1, 1, 1.5)$.

value $\beta_\perp = 0.32(5)$ deduced from the magnetic reflection $(0, 0, 4.5)$ and the value $\beta_\perp = 0.34(4)$ deduced from the magnetic reflection $(1, 1, 1.5)$ are in good agreement with the theoretical value $\beta_{XY} = 0.36$ for a 3D planar (XY) magnet [1].

In Fig. 7-10, we plot the longitudinal scan at the reciprocal lattice point $(1, 1, 0)$ for temperatures $T = 10.00$K (below the transition temperature $T_\perp$), and $T = 35.34$K (above the transition temperature $T_\perp$). Above $T_\perp$, the scattering profile at $(1, 1, 0)$ is independent of temperature, and resolution-limited. The data are well described by

$$I \sim \frac{1}{\left\{1 + [(q_L - q_L^0)/w_L]^2\right\}^3}. \tag{7.11}$$

The dashed line in Fig. 7-10 is the result of a least-squares fit of the data at $T = 35.34$K to Eq. 7.11. The best fit value for w_L is $w_L = 0.00093(1)\text{Å}^{-1}$. The dashed line therefore represents the experimentally measured longitudinal resolution function. However, as soon as the temperature is lowered below the transition temperature $T_\perp$, the longitudinal scan at $(1, 1, 0)$ broadens progressively with decreasing temperature, *i.e.* with increasing magnetic intensity. This broadening arises from the lattice distortion as evident in the data for $T = 10.00$K shown in Fig. 7-10. The solid line in Fig. 7-10 is the result of a least-squares fit of the data at $T = 10.00$K to

$$I \sim \frac{1}{\left\{1 + [(q_L - q_L^0)/w_L']^2\right\}^3} + \frac{y}{\left\{1 + [(q_L - (q_L^0 + \Delta Q)/w_L']^2\right\}^3} \tag{7.12}$$

with the coefficient $y = 0.35$. The best fit yields for the parameters the values $\Delta Q = 0.00125(2)\text{Å}^{-1}$ and $w_L' = 0.00105(2)\text{Å}^{-1}$. The value $y = 0.35$ implies that the six equivalent domains are not equally populated in this sample, while the value $w_L' = 0.00105(2)\text{Å}^{-1} (> w_L^{reso} = 0.00093(1)\text{Å}^{-1})$ indicates that the atomic structure has lost its LRO in the hexagonal a-b plane.

In Fig. 7-11, we show representative scans along the longitudinal direction at the magnetic-superlattice position $(1, 1, 1.5)$. In the case that the Ising spin component is not ordered, the scattering profile at $(1, 1, 1.5)$ reflects the magnetic structure of the XY spin component $\vec{S}_\perp$ within the hexagonal a-b plane. It is interesting to notice

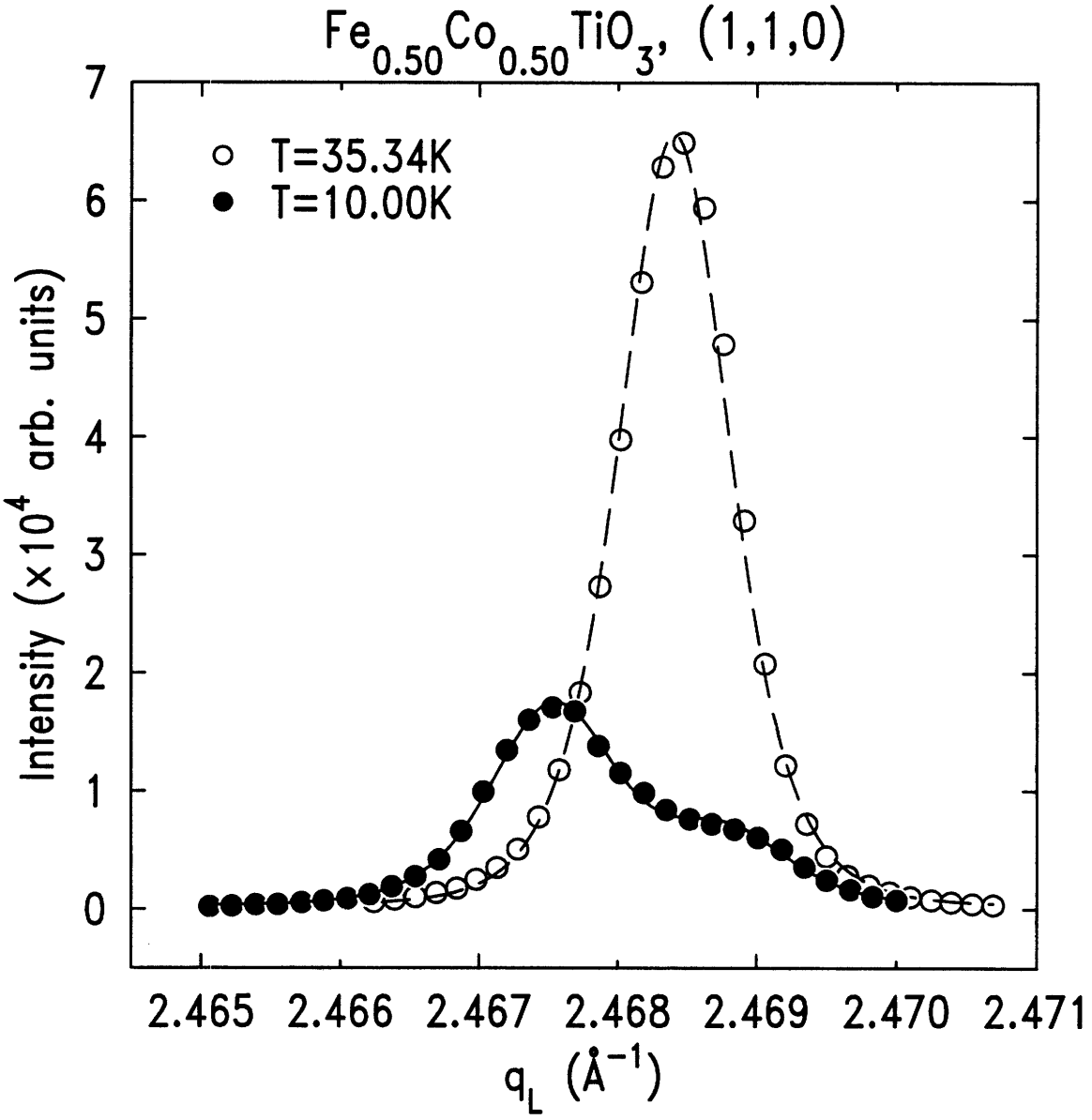

Figure 7-10: Representative longitudinal scans at the structural peak $(1, 1, 0)$ for $Fe_{0.50}Co_{0.50}TiO_3$.

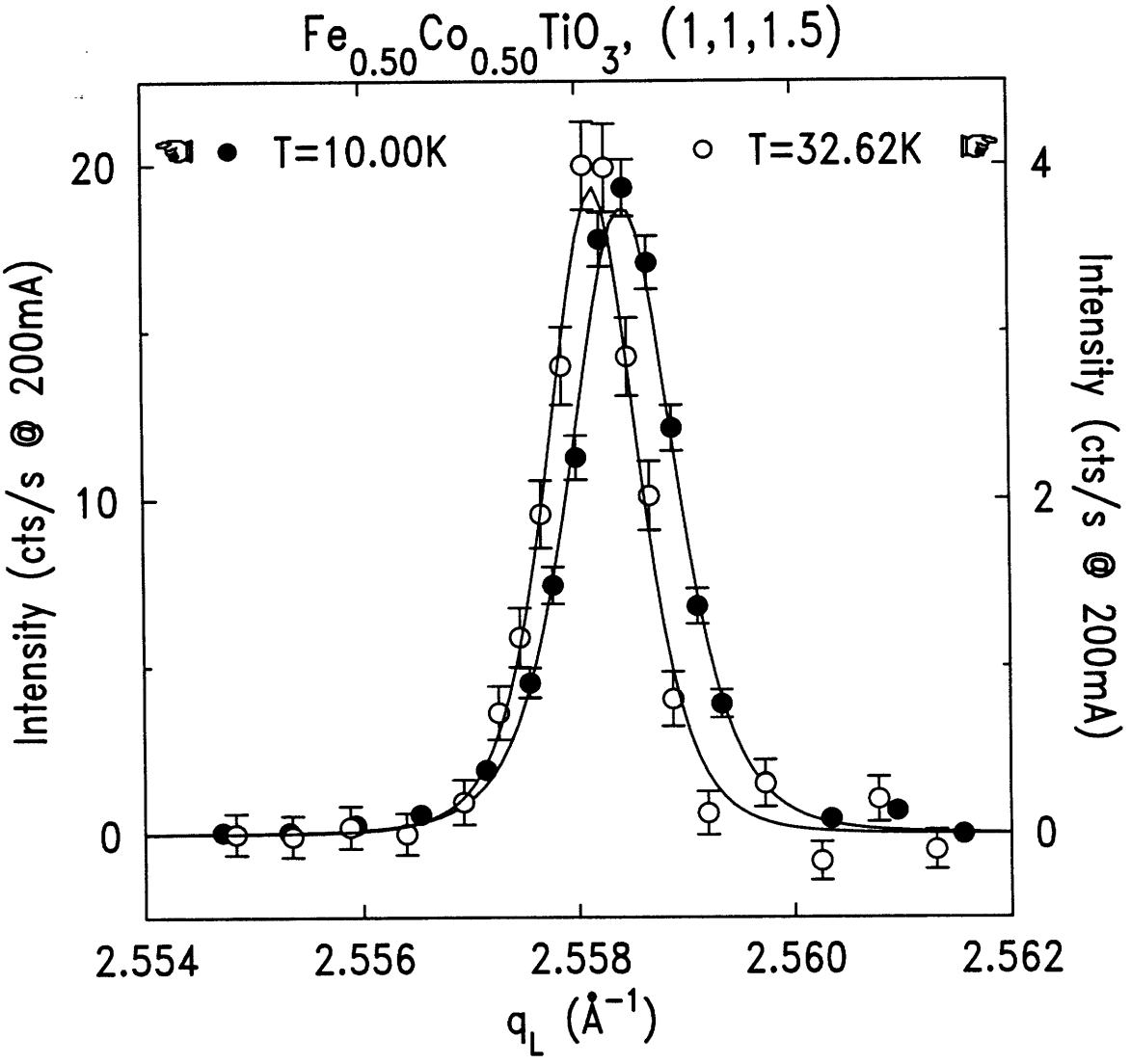

Figure 7-11: Representative longitudinal scans at the magnetic-superlattice position $(1, 1, 1.5)$ for $Fe_{0.50}Co_{0.50}TiO_3$.

that while the longitudinal profile of the structural peak $(1,1,0)$ exhibits the feature of a double-peak due to the lattice distortion, the longitudinal profile of the magnetic reflection $(1,1,1.5)$ is symmetric (cf. Fig. 7-10). This is because only the spin component perpendicular to the momentum transfer $\vec{Q}$ contributes to the magnetic scattering intensity. Furthermore, the magnetic scattering profile at $(1,1,1.5)$ for $T = 10.00$K is slightly broader than that for $T = 32.62$K. The solid lines in Fig. 7-11 are the results of least-squares fits of the data to a Lorentzian squared cross-section convoluted with the resolution. Since the magnetic intensity at $(1,1,1.5)$ goes to zero as the sample is heated above the transition temperature, it is therefore impossible to measure experimentally the resolution function at the reciprocal lattice point $(1,1,1.5)$. Fortunately, the reciprocal lattice point $(1,1,1.5)$ is very close to $(1,1,0)$, where the experimental resolution function can be obtained by measuring the scattering profiles for temperatures above the transition temperature $T_\perp$ (Eq. 7.11). We thus use Eq. 7.11 as the resolution function for $(1,1,1.5)$. Clearly, at low temperatures (e.g. $T = 10.00$K) both the magnetic and atomic structures break into domains, albeit with a very long length scale of $\sim 5,000$Å, in the a-b plane. However, given the extremely large length and the lack of precise resolution function at the reciprocal lattice point $(1,1,1.5)$, the information regarding the relative size of the magnetic and the atomic structure within the a-b plane is unobtainable.

7.2.3 $Fe_{0.65}Co_{0.35}TiO_3$

In Ref. [141, 142], Wong *et al.* suggested that in magnetic systems with competing orthogonal spin anisotropies, when one spin component orders, the other spin component may experience a site-random field through the off-diagonal coupling terms such as $G_{xz}(ij)S_x(i)S_z(j)$. Because of this random field effect, the low temperature mixed phases contain domains. However, in the earlier neutron scattering studies [139, 140, 141, 142, 143, 144, 145], the scattering profile of the mixed phases was found to be resolution-limited. Our next effort was therefore to study the mixed phases in $Fe_{0.65}Co_{0.35}TiO_3$. As suggested by Fig. 6-2, at this concentration, there are successive Ising and XY transitions with decreasing temperature, and the lower

temperature phase is a mixed phase.

In Fig. 7-12 and Fig. 7-13, we show a series of scans at the magnetic reflection $(1, 1, 1.5)$ along the longitudinal (Fig. 7-12) and the transverse (Fig. 7-13) directions. The scattering profile is resolution-limited for temperatures higher than $\sim$ 17K, whereas the reflection is significantly broader than the resolution for temperatures lower than $\sim$ 17K.

This broadening is detailed in Fig. 7-14, where we show the temperature dependence of the integrated intensity, the peak intensity, the in-plane transverse HWHM and the longitudinal HWHM of the magnetic reflection at the reciprocal-lattice position $(1, 1, 1.5)$. At a temperature $T_{\|}(x = 0.65) = 41.55(5)$K, there is a sudden rise of the scattering intensity, indicating the onset of the ordering of the Ising magnetic component $S_{\|}$. For temperatures higher than $\sim$ 17K, this magnetic reflection is resolution-limited, so that this phase has LRO. For T near $T_{\|}(x = 0.65)$, both the integrated and the peak intensities are well described by a simple power law, $I \sim \left(1 - \frac{T}{T_{\|}(x=0.65)}\right)^{2\beta_{\|}}$. The best fit value of $\beta_{\|}$ is 0.33(2), consistent with the theoretical result $\beta = 0.35(1)$ for a random exchange three-dimensional (3D) uniaxial (Ising) magnetic system [147, 148, 149]. The thick solid line BC in Fig. 6-2 is therefore confirmed to be a conventional second-order phase transition line to a LRO state, consistent with the results from earlier studies [140].

As the sample is cooled further down to below $\sim$ 17K, the magnetic reflection profile becomes broader (Fig. 7-14(c) & (d)) with a corresponding decrease in peak intensity (Fig. 7-14(b)). This indicates that below $\sim$ 17K, the magnetic structure is no longer long-range ordered; instead, it breaks into domains. The line shape of the scattering profile is consistent with a Lorentzian squared cross-section:

$$S(\mathbf{q}) = \frac{I_0}{\left\{1 + \left[(q_{\|} - q_{\|}^0)/\kappa_{\|}\right]^2 + \left[(\vec{q}_{\perp} - \vec{q}_{\perp}^0)/\kappa_{\perp}\right]^2\right\}^2} \tag{7.13}$$

where the $\|$ and $\perp$ signs are with respect to the hexagonal c axis.

The solid lines in Fig. 7-12 and Fig. 7-13 for temperatures $T = 13.51$K and $T = 16.01$K are the results of fits of the data to this Lorentzian squared cross-section

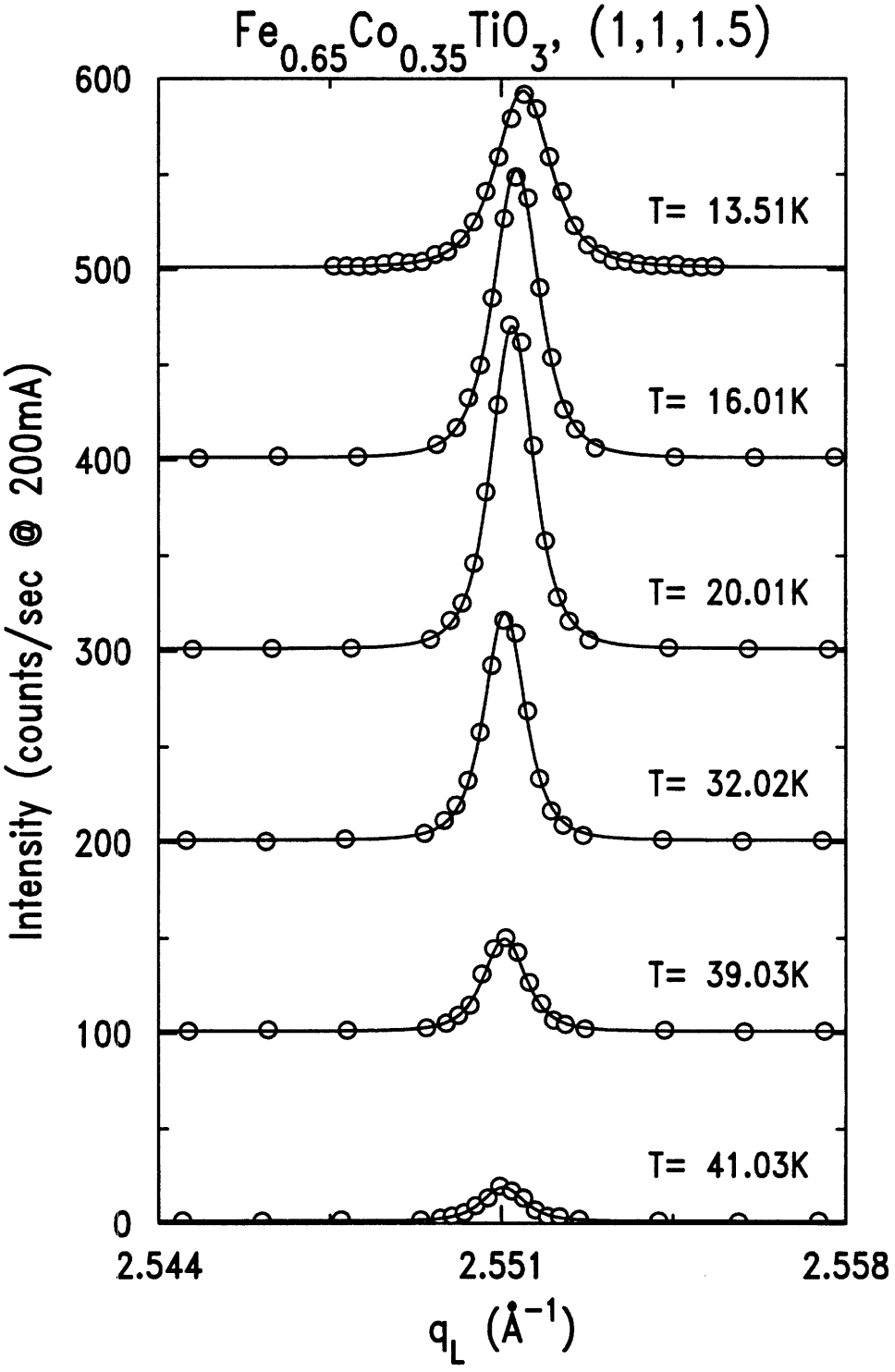

Figure 7-12: Representative scans along the longitudinal direction at the magnetic-superlattice position $(1, 1, 1.5)$ for $Fe_{0.65}Co_{0.35}TiO_3$.

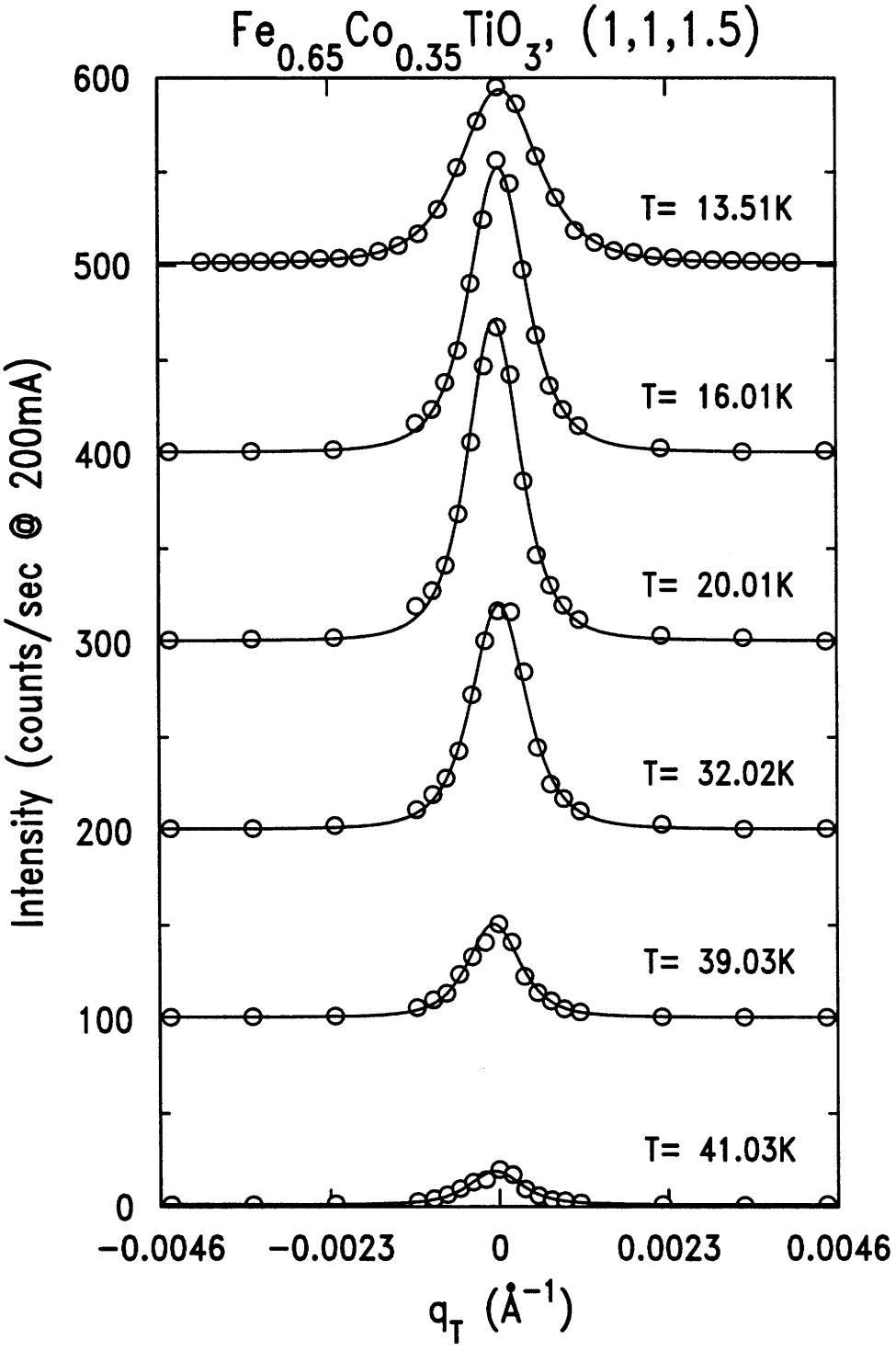

Figure 7-13: Representative scans along the in-plane transverse direction at the magnetic-superlattice position $(1, 1, 1.5)$ for $Fe_{0.65}Co_{0.35}TiO_3$.

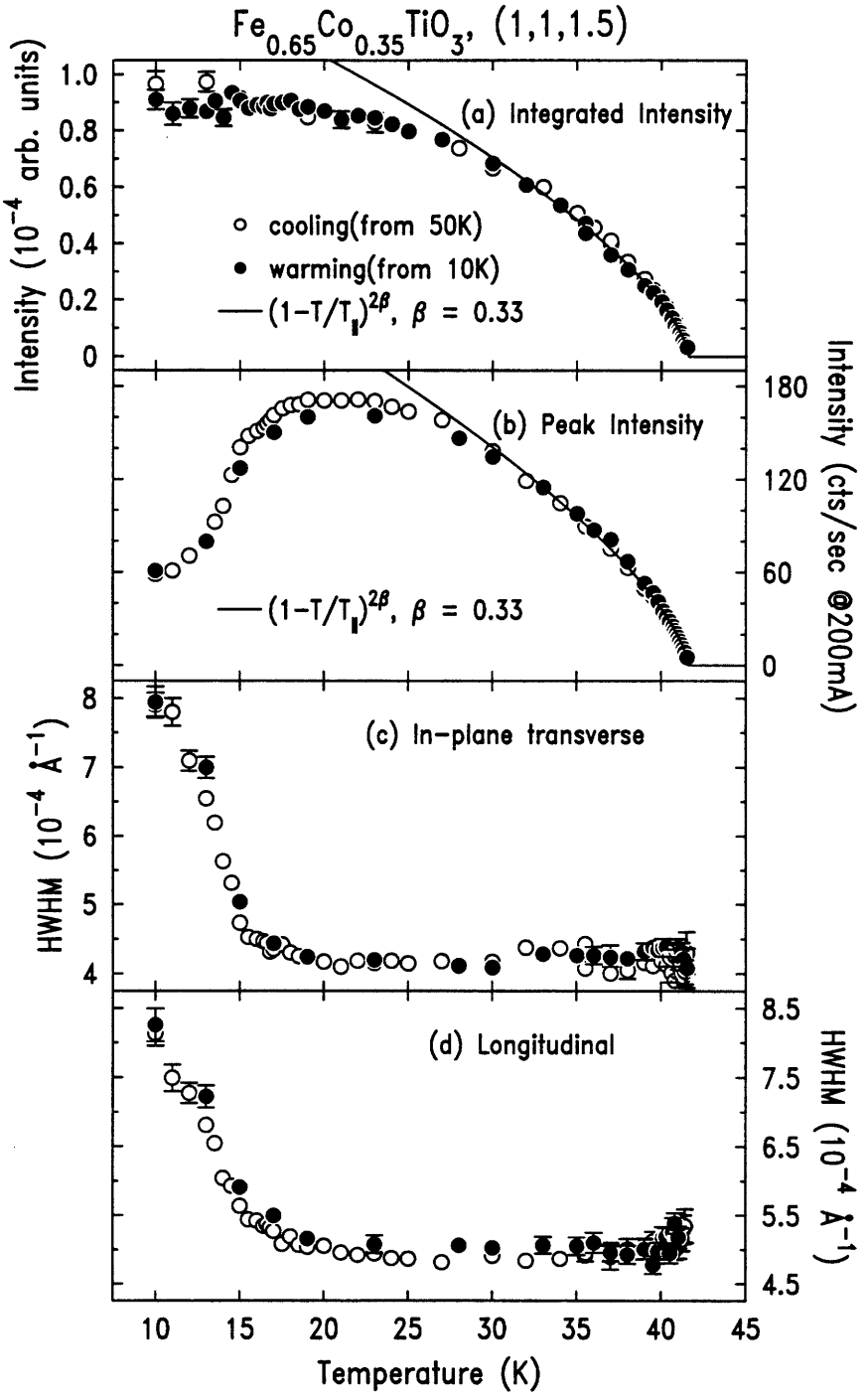

Figure 7-14: The summary plots for the magnetic-superlattice reflection $(1, 1, 1.5)$ for $Fe_{0.65}Co_{0.35}TiO_3$. The unfilled circles are the data from a cooling (from 50K) run, and the filled circles are the data from a subsequent warming (from 10K) run. (a) The integrated intensity; (b) The peak intensity; (c) The transverse HWHM; and (d) The longitudinal HWHM.

(Eq. 7.13) convoluted with the experimental resolution,

$$I(\mathbf{q}) = \int R(\zeta) S(\mathbf{q} - \zeta) d\zeta \tag{7.14}$$

where $I(\mathbf{q})$ is the measured intensity. $R(\zeta)$, the experimentally measured resolution function, has the approximate form

$$R(\zeta) \sim \frac{[1 - |(\zeta_V - q_V^0)/w_V|]}{\left\{1 + [(\zeta_L - q_L^0)/w_L]^2\right\}^2 \left\{1 + [(\zeta_T - q_T^0)/w_T]^2\right\}^2} \tag{7.15}$$

where the parameters w_L, w_T and w_V were determined by the measurements of the resolution-limited peaks for temperatures higher than $\sim$ 17K. In other words, for temperatures higher than $\sim$ 17K, the measured x-ray intensity is:

$$I(\mathbf{q}) = \int R(\zeta) I_0 \delta(\mathbf{q} - \zeta) d\zeta \sim R(\mathbf{q}). \tag{7.16}$$

Typical values for w_L, w_T, w_V are 0.0008Å^{-1}, 0.0007Å^{-1} and 0.02Å^{-1}. The value of $w_L = 0.0008$Å^{-1} is consistent with theoretical expectations for the longitudinal resolution of a vertical synchrotron-x-ray scattering geometry using Ge(111) crystals as both monochromator and analyzer. The w_T value of 0.0007Å^{-1} was controlled by the sample mosaicity, and the w_V value of 0.02Å^{-1} was controlled by the horizontal slits.

The coordinates $\{q_L, q_T, q_V\}$ are related to $\{q_\parallel, \vec{q}_\perp\}$ by

$$\begin{aligned} q_{(1,1,0)} &= q_L \cos\gamma - q_V \sin\gamma \\ q_{(3,-3,0)} &= q_T \\ q_{(0,0,l)} &= q_L \sin\gamma + q_V \cos\gamma \end{aligned} \tag{7.17}$$

where $\gamma \sim 15°$, as shown in Fig. 7-15.

In fitting the data to Eq. 7.14, we make use of Eq. 7.17. The integration along the out-of-plane direction can be performed analytically ($w_V \gg \kappa_\parallel, \kappa_\perp$), the three dimensional integration can then be reduced to a two dimensional integration. Least

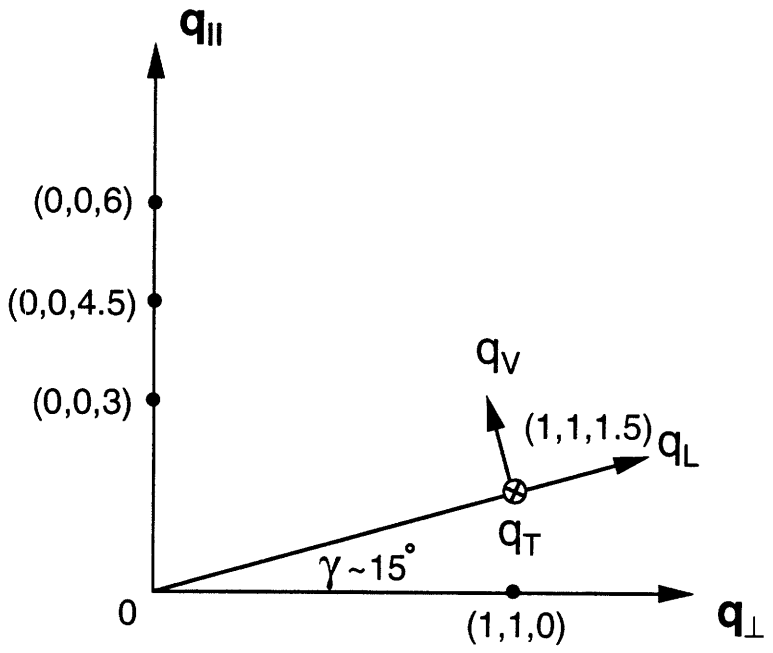

Figure 7-15: The comparison between the longitudinal component (q_{L}), the transverse component (q_{T}) and the out-of-plane component (q_{V}) of the momentum transfer with those parallel ($q_{\|}$) and perpendicular ($q_{\perp}$) to the hexagonal c-axis. The q_{T} direction is perpendicular to both the q_{L} direction and the $q_{\|}$ direction, and is therefore perpendicular to the paper plane.

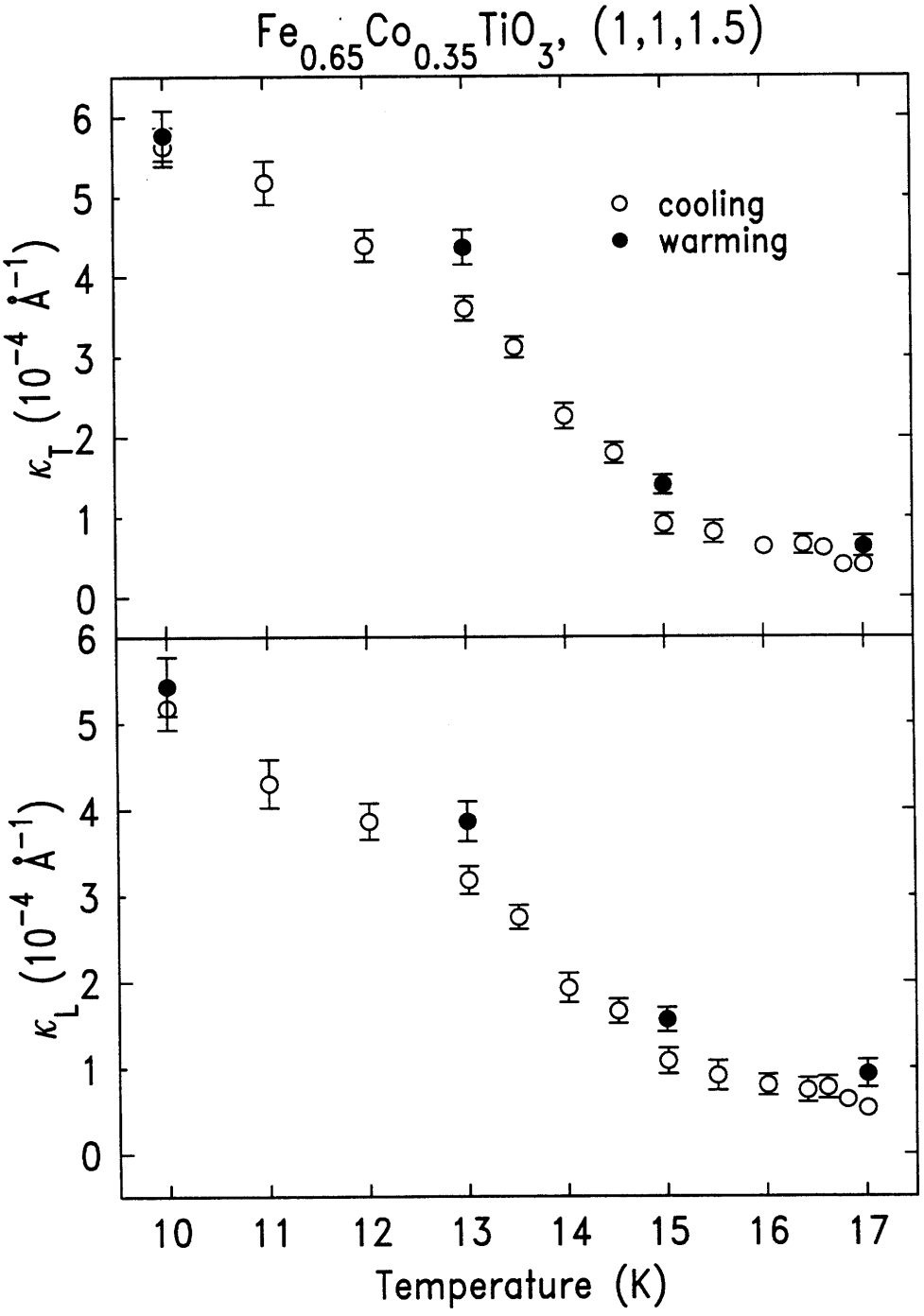

Figure 7-16: The inverse correlation length κ_L and κ_T as functions of temperature.

squares fits of data for temperatures below $\sim$ 17K to Eq. 7.13, convoluted with the instrumental resolution function, Eq. 7.15, yield values for $\kappa_{\rm L}$ and $\kappa_{\rm T}$, as shown in Fig. 7-16. At T = 10K, the in-plane domain size of the spin component $S_{\parallel}$ is $\sim 2,000$Å.

As suggested by earlier neutron studies [140], for $Fe_{0.65}Co_{0.35}TiO_3$ there is an ordering of the XY spin component $\vec{S}_{\perp}$ at $\sim$ 17K. Representative transverse scans at the magnetic-superlattice reflection $(0, 0, 4.5)$ are shown in Fig. 7-17. As noted before, the magnetic x-ray intensity at $(0, 0, 4.5)$ is proportional to $|\vec{S}_{\perp}|^2$. Unfortunately, the scattering intensity at $(0, 0, 4.5)$ was extremely weak, which limited the information obtainable on the ordering of the XY spin component $\vec{S}_{\perp}$. However, similar to the case in both $Fe_{0.35}Co_{0.65}TiO_3$ and $Fe_{0.50}Co_{0.50}TiO_3$, the atomic structure along the c-axis direction breaks into domains following the onset of this ordering of the XY spin component, as shown Fig. 7-18. It is therefore clear that the XY magnetic ordering along the hexagonal c-axis is also short-ranged. This is because generally one expects that the correlation length of the magnetic structure will be smaller, but not larger, than that of the atomic structure.

We remarked early on that the much more significant broadening of the transverse scans for the $(0, 0, l)$ reflections reflects mosaicity effects arising from the establishment of the SRO of the XY spin component. This can be further seen by by comparing directly the following three peaks: $(0, 0, 3)$(charge), $(0, 0, 4.5)$(magnetic) and $(0, 0, 6)$(charge). If the broadening along the transverse direction was mainly due to finite size effects, the domain size, κ^{-1}, deduced from the data at these three reflections should be the same. However, if the broadening along the transverse direction arises primarily from mosaicity, the angular width should be identical at these three peaks. As shown in Fig. 7-19, mosaicity is clearly the dominant cause of the broadening along the transverse direction for the $(0, 0, l)$ reflections for temperatures below $\sim$ 17K.

In Fig. 7-20, we plot both the longitudinal and the transverse scans at the reciprocal lattice point $(1, 1, 0)$ at temperatures T = 10.00K (the mixed phase), T = 25.02K (the $S_{\parallel}$-ordered phase) and T = 50.03K (the paramagnetic phase) for $Fe_{0.65}Co_{0.35}TiO_3$.

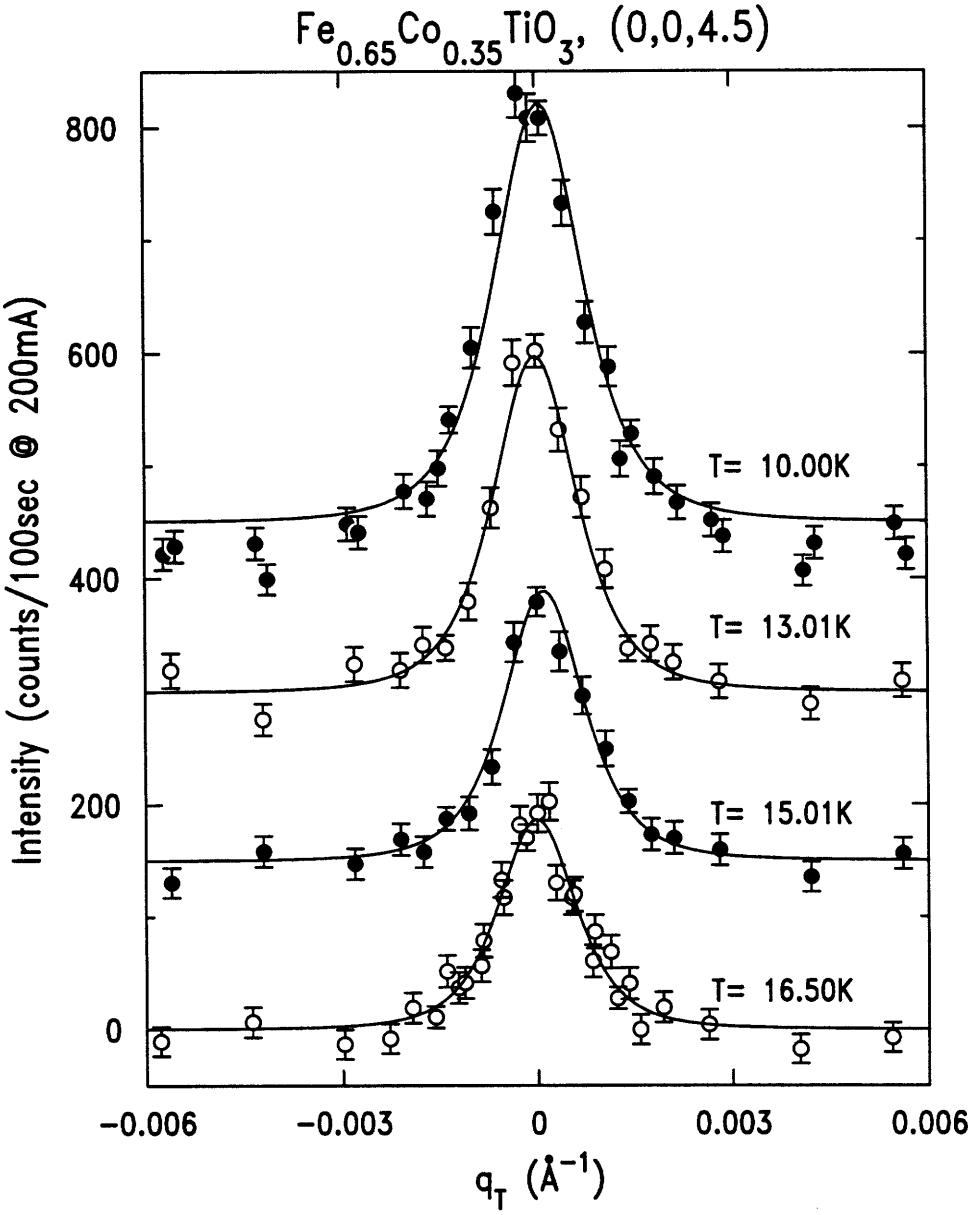

Figure 7-17: Representative transverse scans at the magnetic-superlattice reflection $(0, 0, 4.5)$ for $Fe_{0.65}Co_{0.35}TiO_3$. A flat background was subtracted for data at each temperature.

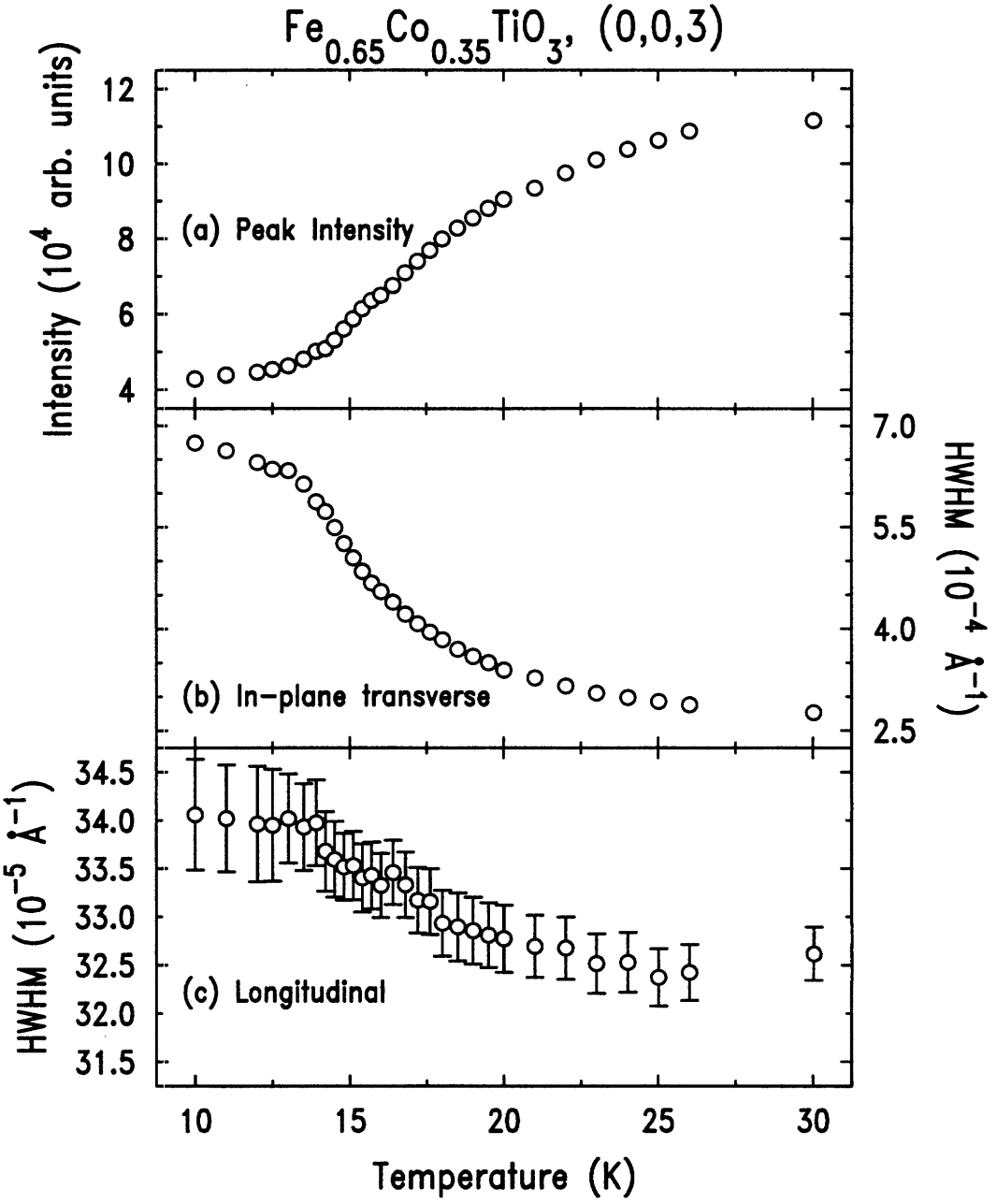

Figure 7-18: The temperature dependence of the peak intensity(a), the transverse HWHM(b) and the longitudinal HWHM(c) of the structural peak $(0, 0, 3)$ for $Fe_{0.65}Co_{0.35}TiO_3$.

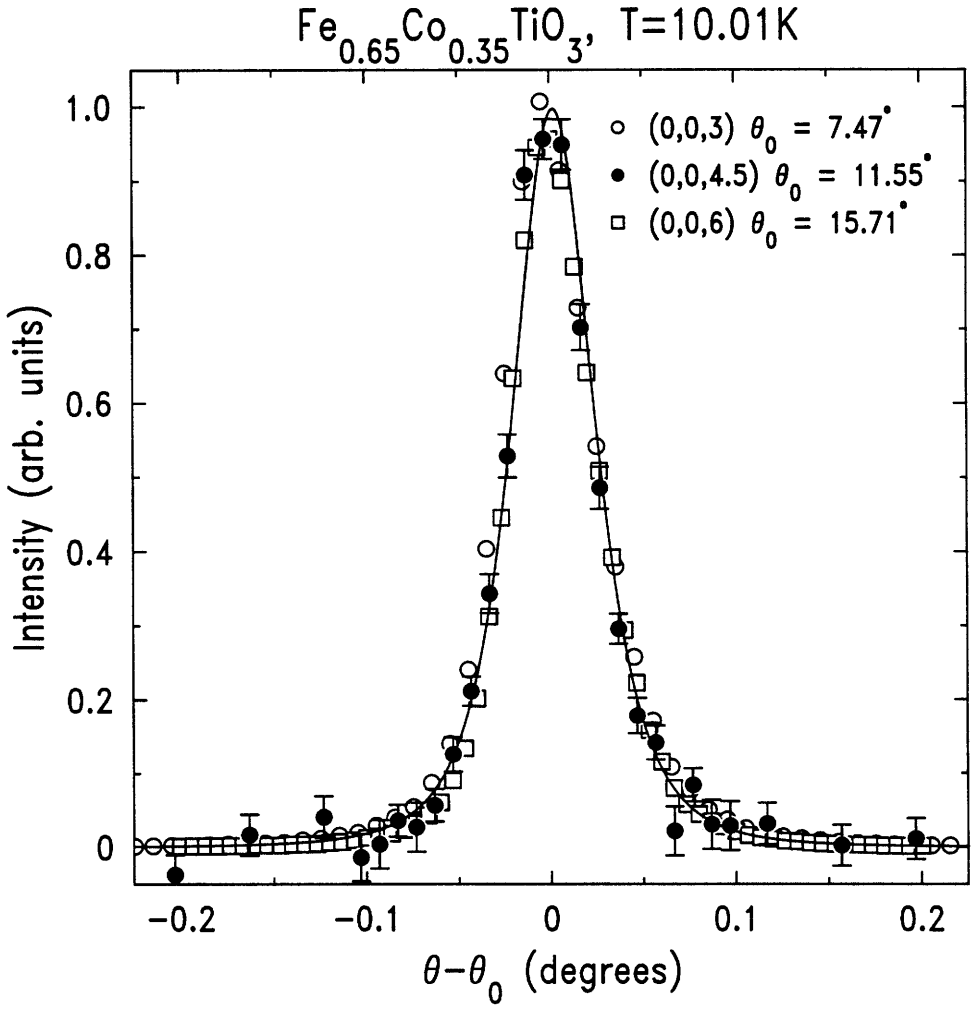

Figure 7-19: The broadening along the traverse direction as a result of changing mosaicity effect, rather than the finite size (domain) effect. The unfilled circles are data at $(0, 0, 3)$, which is a charge peak. The filled circles are data at $(0, 0, 4.5)$, which is a magnetic peak. The unfilled square symbols are the data at $(0, 0, 6)$, which is another charge peak. Clearly, the transverse broadening results mainly from mosaicity effects. The solid line in the figure is the best fit of a simple Lorentzian squared to the data.

As noted above, the scattering profile at $(1,1,0)$ reflects the structure in the hexagonal a-b plane. In both the paramagnetic and the $S_{||}$-ordered phases, the scattering profile at $(1,1,0)$ is resolution-limited and independent of temperature. The dashed lines are the results of least-squares fits of the data for $T = 25.02$K and $T = 50.03$K to the form:

$$I \sim \frac{1}{\left\{1 + [(q_L - q_L^0)/w_L]^2\right\}^2 \left\{1 + [(q_T - q_T^0)/w_T]^2\right\}^2} \tag{7.18}$$

with $w_L = 0.000767\text{Å}^{-1}$, and $w_T = 0.000845\text{Å}^{-1}$. The value $w_T = 0.000845\text{Å}^{-1}$ corresponds to a mosaicity of 0.025°. Eq. 7.18 with above-stated parameters is the experimentally measured resolution function. For temperatures below $\sim$ 17K, the longitudinal data are again consistent with a lattice distortion within the a-b plane. The solid line in Fig. 7-20 is the result of a least-squares fit of the data for $T = 10.00$K to

$$I \sim \frac{1}{\left\{1 + [(q_L - q_L^0)/w_L]^2\right\}^2} + \frac{y}{\left\{1 + [(q_L - (q_L^0 + \Delta Q)/w_L]^2\right\}^2} \tag{7.19}$$

with the coefficient y fixed at 0.5.

7.3 Discussion

Among the data presented, one common feature is the breakup of both the magnetic and the atomic structure of the crystal into domains following the ordering of the XY spin components. This breakup of the XY phases into domains corresponds to our expectations for random anisotropy systems, with strong magnetoelastic coupling. The most straightforward origin of the random anisotropy in $Fe_xCo_{1-x}TiO_3$ is the random nature of the mixture itself. Specifically, by analogy with Ref. [141, 142], substitution of Co^{2+} ions with Fe^{2+} ions reduces the local symmetry of the crystal field acting on the Co^{2+} ions. In particular, this substitution induces random diagonal and off-diagonal exchange terms of the form $G_{lm}(ij)S_l(i)S_m(j)$ $(l, m = x, y$ or $z(||))$

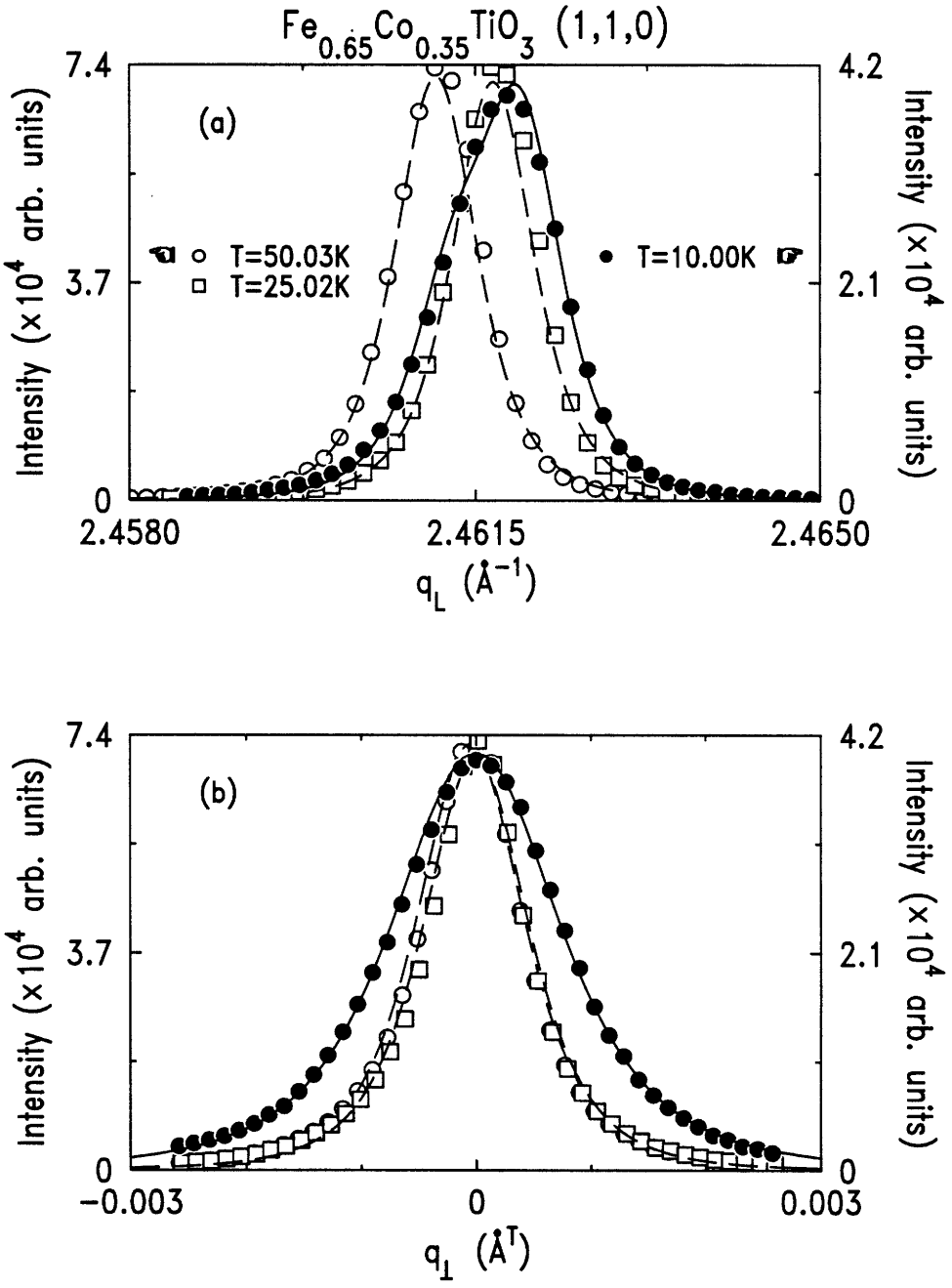

Figure 7-20: The longitudinal and the transverse scans at the reciprocal lattice point $(1, 1, 0)$ for temperatures $T = 10.00$K (the mixed phase), $T = 25.02$K (the $S_{||}$-ordered phase) and $T = 50.03$K (the paramagnetic phase).

in the effective spin Hamiltonian

$$\mathcal{H} = 2\sum_{ij}\{J_{\|}(ij)\mathrm{S}_{\|}(i)\mathrm{S}_{\|}(j) + J_{\perp}(ij)[\vec{\mathrm{S}}_{\perp}(i)\cdot\vec{\mathrm{S}}_{\perp}(j)]\}. \tag{7.20}$$

This follows most simply from the anisotropy in the g-term induced by the resultant lower symmetry crystal field.

In the cases of $x = 0.35$ and 0.50, because of the presence of terms of the form $G_{xx}(ij)\mathrm{S}_x(i)\mathrm{S}_x(j) \neq G_{yy}(ij)\mathrm{S}_y(i)\mathrm{S}_y(j)$, and terms like $G_{xy}(ij)\mathrm{S}_x(i)\mathrm{S}_y(j)$, the $\vec{\mathrm{S}}_{\perp}$-ordering transition falls into the universality class of a 3D XY magnet with random anisotropy. This identification assumes that an XY magnet with a three-fold random anisotropy is equivalent to an XY magnet with random anisotropy. In the framework of the mean-field approximation, the anisotropy field $\vec{\mathrm{H}}_{\mathrm{A}}(\mathrm{i})$ at the ith spin under the term $G_{xx}(ij)\mathrm{S}_x(i)\mathrm{S}_x(j)$, is proportional to $(G_{xx}(ij) - G_{yy}(ij)) < |\vec{\mathrm{S}}_{\perp}| >$. This random anisotropy field is zero above and at the transition temperature $T_{\perp}$, but nonzero and increasing with decreasing temperature below $T_{\perp}$. This is consistent with the experimental findings of Fig. 7-2 and Fig. 7-9 where, as the temperature is lowered below $T_{\perp}$, the domain size decreases progressively as a result of the increasing strength of the random anisotropy field, $\vec{\mathrm{H}}_A \sim |\vec{\mathrm{S}}_{\perp}|$. We emphasize that the thermal disordering effects become less important as one lowers the temperature. This therefore reflects the domination of the quenched disorder over the thermal disorder at lower temperatures in random systems. The transition from the paramagnet to the $\vec{\mathrm{S}}_{\perp}$-domain state is therefore critical at $T_{\perp}$ even though there is no conventional LRO below $\mathrm{T}_{\perp}$. The line AB in the phase diagram (Fig. 6-2) thus appears to be as a novel type of critical line.

In the case of $x = 0.65$, on the one hand, for the XY spin component $\vec{\mathrm{S}}_{\perp}$, besides the random anisotropy effect described above, since the spin component $\mathrm{S}_{\|}$ has already ordered, the spin component $\vec{\mathrm{S}}_{\perp}$ experiences a site-random field $G(ij)_{\|\perp} < S_{\|} >$. Further, since the $\mathrm{S}_{\|}$ component has almost reached its saturation value at the XY transition temperature, we might expect this random field effect to dominate the phase behavior of the XY spin component $\vec{\mathrm{S}}_{\perp}$ for $x = 0.65$. On the other hand, for

the Ising spin component $S_{\|}$, it experiences a local random field $G(ij)_{\|\perp} < S_{\perp} >$ following the short-range ordering of the XY spin component $\vec{S}_{\perp}$ at $\sim$ 17K. Naively, this $S_{\perp}$-driven random field effect would seem to explain the destruction of the Ising LRO below 17K. However, there is a serious caveat in this argument. Specifically, since the Ising LRO is well established above 17K then the above process corresponds to the ZFC rather than FC procedure. Thus, if the behavior corresponds to that observed in other RFIM systems, then the Ising random field created by the $\vec{S}_{\perp}$ ordering should not have destroyed the Ising LRO. Apparently, therefore, the more complicated coupled Ising-XY nature of this system obviates the simple mean-field based analogy to the RFIM. Clearly, a more sophisticated theory will be required to understand the rich physics exhibited by this system.

In addition to the above, as has been found in holmium [150], strains in the near-surface region through the magnetoelastic coupling represent a second possible source of random anisotropy; their relative role in $Fe_xCo_{1-x}TiO_3$ may be clarified by future x-ray experiments on pure $CoTiO_3$. X-ray measurements at higher energies in the mixed crystals should reveal any possible depth dependence of the XY domain size.

Chapter 8

Field Effects in the Random Ising Magnet $Fe_{0.75}Co_{0.25}TiO_3$ — RFIM

In Chapter 7, we have been emphasizing the XY behavior in the mixed Ising-XY random magnet $Fe_xCo_{1-x}TiO_3$; the Ising behavior by itself does not appear to introduce any unexpected new features. However, we have already seen that following the (short range) ordering of the XY spin component $\vec{S}_\perp$, the Ising spin component $S_\parallel$ lost the LRO due to the random field effects induced by the off-diagonal coupling terms of the form $G_{\perp\parallel}(ij)S_\parallel(i)S_x(j)$. Moreover, with the application of a magnetic field, $Fe_xCo_{1-x}TiO_3$, for $x > 0.5$, becomes a possible prototype for the Random Field Ising Model (RFIM). In this Chapter, we report an x-ray-scattering study of the Ising ($S_\parallel$) ordering in $Fe_{0.75}Co_{0.25}TiO_3$, and especially, its behavior in external magnetic fields.

8.1 Experimental Specifications

The experiments were again carried out on beamline X20A at NSLS. The wavelength of the incident photons was set at $\lambda = 1.305$Å (E = 9.5 KeV). The diffraction occurred in reflection geometry in the horizontal scattering plane and a flat Ge(111) crystal was used as the analyzer. An excellent quality single crystal $Fe_{0.75}Co_{0.25}TiO_3$, grown by the travelling floating zone method was used in the experiments. The sample was mounted on a copper rod in an x-ray-compatible split-pair superconducting

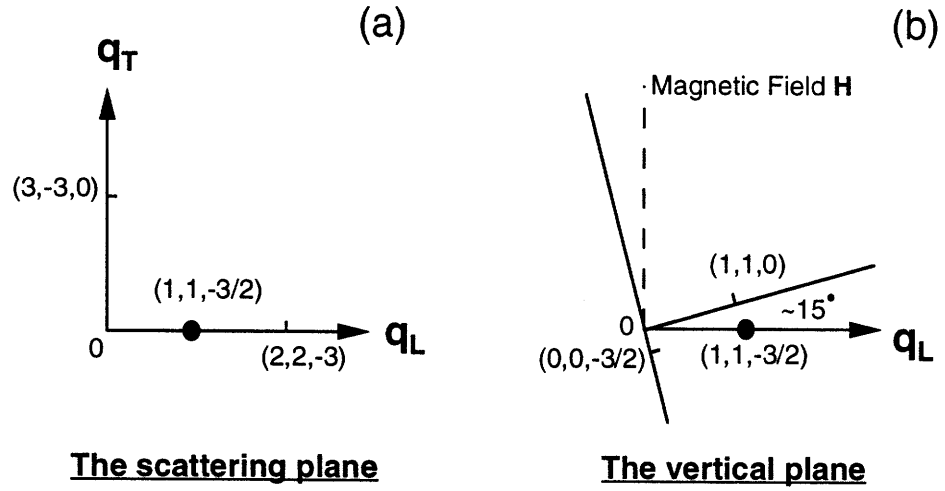

Figure 8-1: The magnetic field direction with respect to the hexagonal c-axis direction. The magnetic field is applied along the vertical direction, perpendicular to the scattering plane(a), which is horizontal. The magnetic field direction is $\sim 15°$ away from the hexagonal c-axis(b).

magnet [25], with the vectors $(1, 1, -1.5)$ and $(3, -3, 0)$ in the scattering plane. The magnetic field was applied in the vertical direction, that is, perpendicular to the scattering plane. The sublattice magnetization measurements were carried out around the magnetic-superlattice position $(1, 1, -1.5)$. Because of the constraint that the superconducting magnet could tilt a maximum of 5°, the magnetic field was *not* along the easy-axis, the c-axis. Instead, it was $\sim 15°$ away from the c-axis as illustrated in Fig. 8-1. The magnetic x-ray intensity at $(1, 1, -1.5)$ is

$$I_m \propto 0.93|\mathrm{S}_{\parallel}|^2 + 0.036|\vec{\mathrm{S}}_{\perp}|^2 + 0.038|\vec{\mathrm{S}}_{\perp} + \vec{\mathrm{L}}_{\perp}|^2. \tag{8.1}$$

In the event that the component $\vec{\mathrm{M}}_{\perp}$ does not order, as the case of $Fe_{0.75}Co_{0.25}TiO_3$, I_m is simply proportional to $|\mathrm{S}_{\parallel}|^2$, $I_m \sim |\mathrm{S}_{\parallel}|^2$.

8.2 Random Ising Magnet $Fe_{0.75}Co_{0.25}TiO_3$

At zero field, when the sample, $Fe_{0.75}Co_{0.25}TiO_3$, is cooled through the transition temperature of $T_N = 43.90(5)$K, there is a sudden rise of the scattering intensity at $(1, 1, -1.5)$, corresponding to the onset of the magnetic ordering of the spin component $S_{\|}$, with a magnetic structure which is ferromagnetic within the hexagonal a-b plane, and antiferromagnetic along the c-axis direction. The scattering profiles remain resolution limited down to 10K, which is the lowest temperature studied in the experiments. Fig. 8-2 shows scans at two representative temperatures, 10.11K and 39.01K. The top and bottom panels show scans along the longitudinal and transverse direction respectively. While the scattering profile is symmetric along the transverse direction (bottom panel), it is asymmetric along the longitudinal direction (top panel). This asymmetry in the longitudinal direction exists at all temperatures studied. The lines (solid and dashed) in Fig. 8-2 are the best fits of the data. The fitting function form was chosen, on a basis of trial and error, to reflect this observed asymmetry along the longitudinal direction. Specifically, the lines represent least-squares fits of the data to the following form:

$$I - I_{BG} = \begin{cases} \dfrac{I_0}{\left\{1 + \left[(q_{\rm L} - q_{\rm L}^0)/w_{\rm L}\right]^2\right\}\left\{1 + \left[(q_{\rm T} - q_{\rm T}^0)/w_{\rm T}\right]^2\right\}} & \text{if } q_{\rm L} \le q_{\rm L}^0 \\ \dfrac{I_0 \exp\left\{-\left[(q_{\rm L} - q_{\rm L}^0)/\sigma_{\rm L}\right]^2\right\}}{1 + \left[(q_{\rm T} - q_{\rm T}^0)/w_{\rm T}\right]^2} & \text{if } q_{\rm L} \ge q_{\rm L}^0 \end{cases} \tag{8.2}$$

where I_{BG} is the flat background, $q_{\rm L}^0 \equiv |\mathbf{q}_{(1,1,-1.5)}|$ and $q_{\rm T}^0 = 0$. The fit values for the parameters are $w_{\rm L} = 0.00141\text{Å}^{-1}$, $\sigma_{\rm L} = 0.00198\text{Å}^{-1}$ and $w_{\rm T} = 0.000573\text{Å}^{-1}$. Eq. 8.2, with the parameters given above, is therefore the experimentally measured in-plane resolution function for the horizontal scattering configuration.

Since the scattering profile is resolution limited, the peak intensity is therefore proportional to the integrated intensity, which, in turn, is proportional to $S_{\|}^2$. In Fig. 8-3, we plot the scattering intensity as a function of temperature near the transition temperature, T_N, at zero field. The solid line is the result of a least squares fit of the

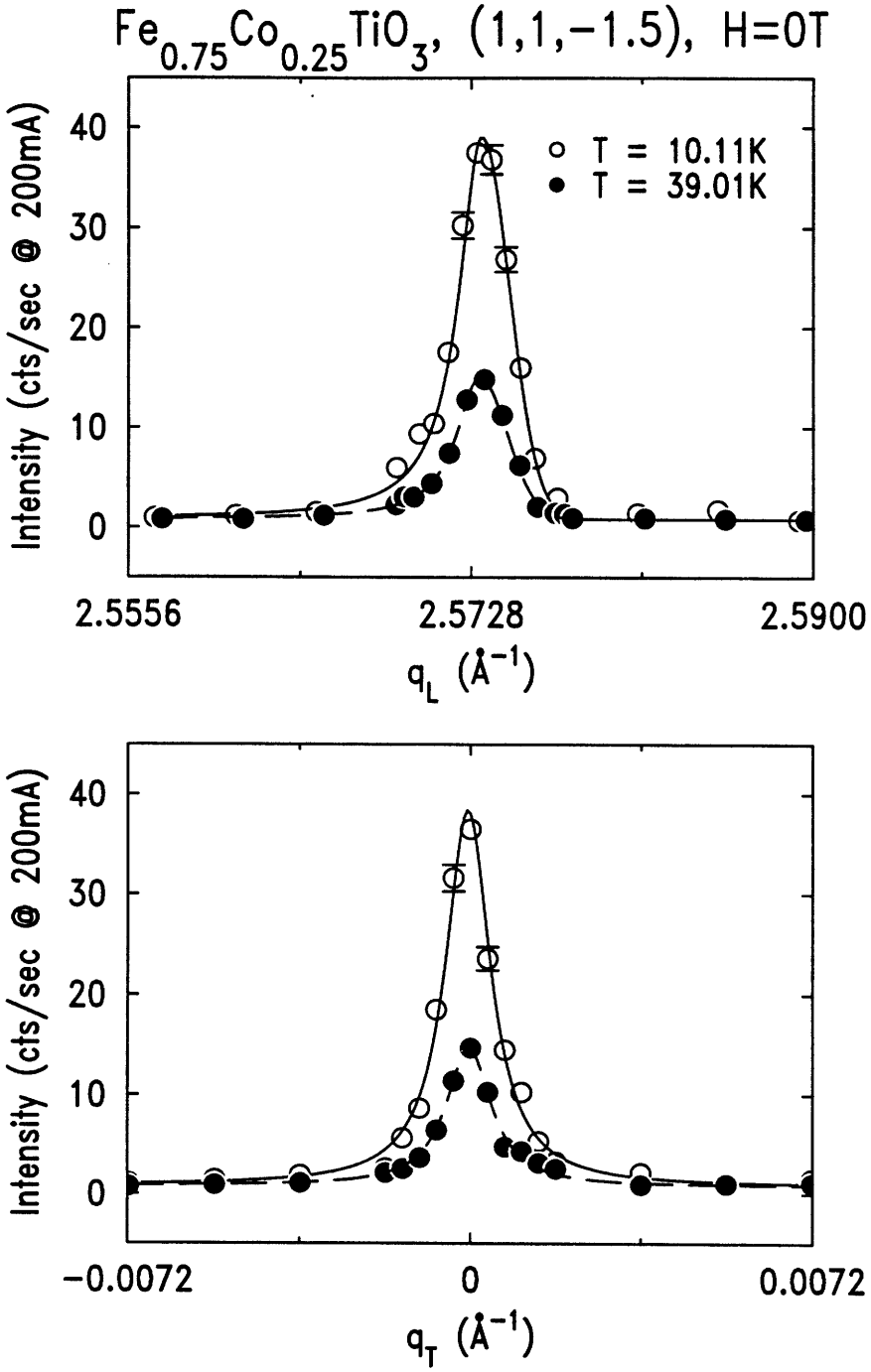

Figure 8-2: Representative scans at the reciprocal lattice position $(1, 1, -1.5)$ for $Fe_{0.75}Co_{0.25}TiO_3$ at zero field. The unfilled circles are data taken at 10.11K, while the filled circles are data taken at 39.01K. The solid and the dashed lines are the fits of the data to Eq. 8.2 at 10.11K and 39.01K, respectively. Top Panel: Longitudinal scans. Bottom Panel: Transverse scans.

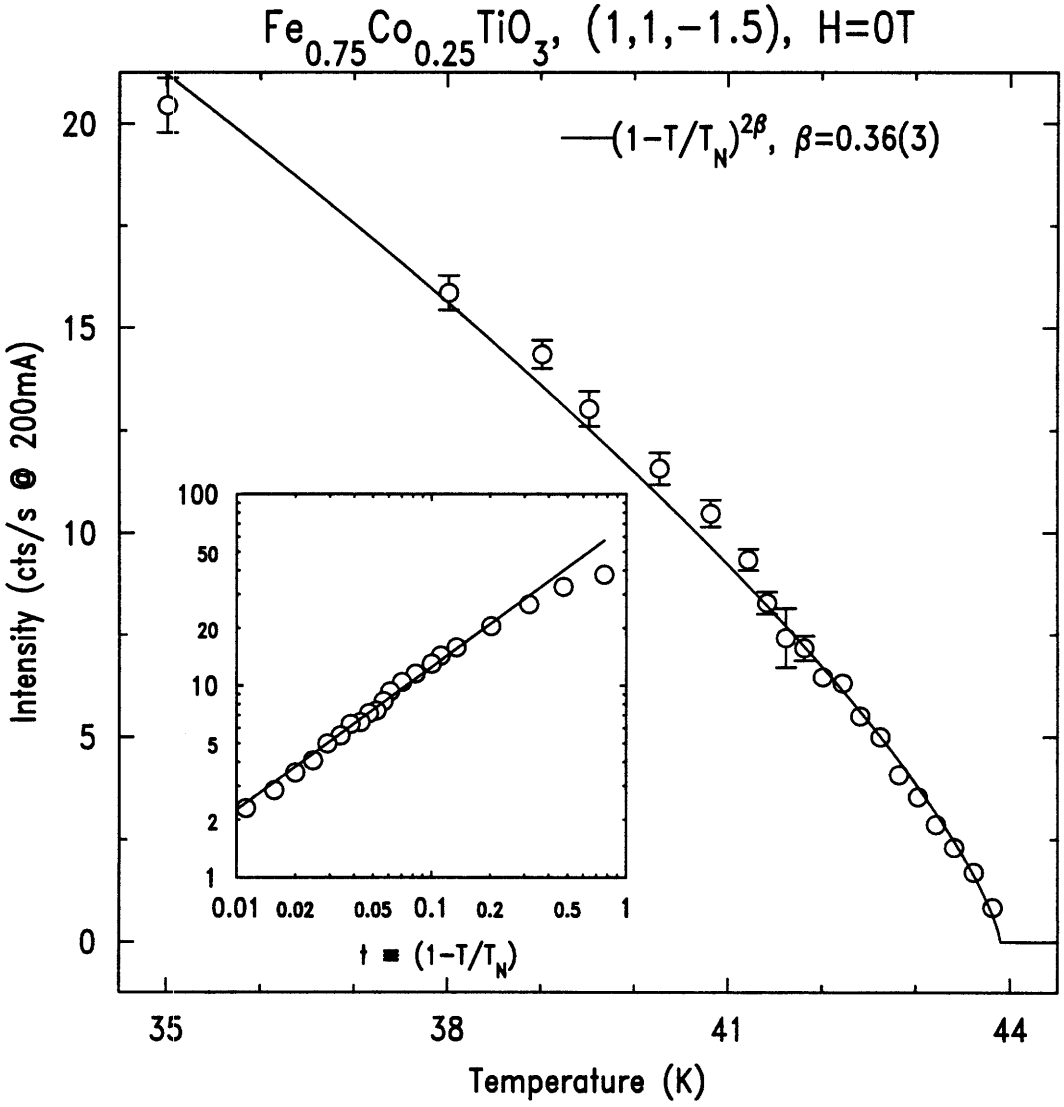

Figure 8-3: The ordering of the spin component $S_{\|}$ at zero field for $Fe_{0.75}Co_{0.25}TiO_3$. The solid line represents a least-squares fit of the data to a simple power law, $I \sim S_{\|}^2 \sim \left(1 - \frac{T}{T_N}\right)^{2\beta}$. The inset shows the data on a log-log scale, and the horizontal axis is the reduced temperature, $t \equiv 1 - \frac{T}{T_N}$.

data to a simple power law,

$$I \sim S_{\parallel}^2 \sim \left(1 - \frac{T}{T_N}\right)^{2\beta}. \tag{8.3}$$

The best fit β value is 0.36(3), consistent with the theoretical value $\beta = 0.35(1)$ expected for the REIM [147, 148, 149], as well as the zero field results of the diluted Ising antiferromagnets $Mn_xZn_{1-x}F_2$ [124, 125] and $Fe_xZn_{1-x}F_2$ [128, 151]. The inset shows the same plot on a log-log scale, where the horizontal axis is the reduced temperature, $t \equiv 1 - \frac{T}{T_N}$. Clearly, the power law relation describes the data near the transition temperature rather well.

Following the observation of Fishman and Aharony [115], the phase behavior of $Fe_{0.75}Co_{0.25}TiO_3$ in an external uniform field should fall into the universality class of the Random Field Ising Model (RFIM). The applied uniform field produces a random staggered field both directly from the random Zeeman energy [152], and also indirectly through the randomness of the exchange constants [115]. A characteristic feature of the properties among the RFIM systems studied so far is that there exists a well-defined metastability boundary in the H–T plane, which separates a high temperature phase in which the properties are independent of the procedure by which the system is prepared, and a low temperature phase in which the results are history dependent (for reviews see Refs. [116, 117, 118, 119]). This is also found to be the case for the mixed random Ising magnet $Fe_{0.75}Co_{0.25}TiO_3$ in magnetic fields, as illustrated in Fig. 8-4, which shows the scattering profiles obtained when the state is reached via two different routes: ZFC in which the sample is cooled first to a low temperature state in the absence of a magnetic field, a magnetic field subsequently applied; and FC in which the sample is cooled in the presence of a magnetic field. The results (Fig. 8-4) exhibit strong hysteresis. The scattering profiles obtained with the FC procedure have a much wider width in wave vector than those obtained with the ZFC procedure. This means that, whereas the ZFC state has LRO, the FC state is short-ranged ordered.

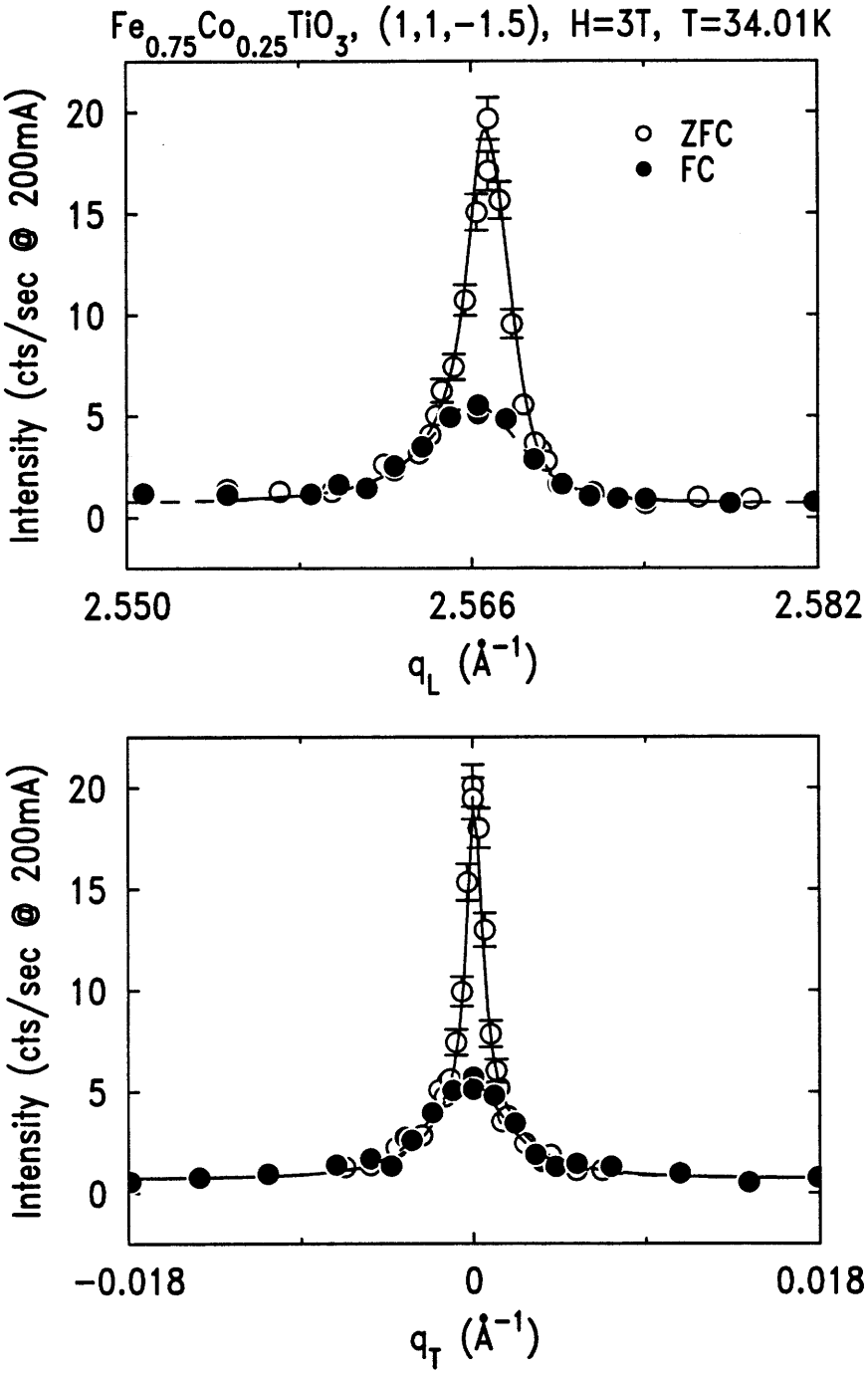

Figure 8-4: The hysteresis shown in the scattering profile measurements. The unfilled circles are data taken on warming from the ZFC state, and the filled circles are data taken from the FC state. Top Panel: Longitudinal scans. Bottom Panel: Transverse scans.

8.3 ZFC Results

We first present the data taken on warming from the ZFC state in $Fe_{0.75}Co_{0.25}TiO_3$. The sample was cooled into the Néel state in the absence of the magnetic field, a magnetic field subsequently applied, and the data were taken on warming. Concordant with the results in the diluted Ising antiferromagnets, the LRO was found to persist to a field-dependent metastability temperature $T_M(H)$. For the field $H = 3$T, the diminution of this LRO is plotted in Fig. 8-5. We notice that the transition is "rounded" near the transition, this is reminiscent of the "*trompe l'oeil* critical behavior" [124, 125, 128], which is the empirical finding in the RFIM systems $Mn_xZn_{1-x}F_2$ and $Fe_xZn_{1-x}F_2$, that the loss of the LRO on warming from the ZFC state is well described by a power-law with a Gaussian distribution of transition temperatures. The solid line in Fig. 8-5 is the best fit of the data to the following functional form:

$$I = \frac{I_0}{\sqrt{\pi}\sigma} \int \left[\left(1 + \frac{t-T}{t-T_{co}} \right)^{1/2\beta} - 1 \right]^{2\beta} \exp\left(- \left(\frac{t-T_C}{\sigma} \right)^2 \right) dt \qquad (8.4)$$

with the center of the Gaussian distribution $T_C = 34.00(5)$K, the exponent $\beta = 0.15(3)$, the spread of transition temperature, $\sigma = 0.41(5)$K and the crossover temperature $T_{co} = 27.6(8)$K. We emphasize that this broadening near the transition is *not* due to any concentration gradients, nor is it due to the field inhomogeneities, instead, it is an inherent feature of the RFIM [124, 125].

Eq. 8.4 is written to reflect the behavior of the experimental data, that is, at low temperatures there is a linear temperature dependence of the order parameter squared, but as the temperature is raised closer to the metastability temperature, the data exhibit rounded power law behavior. T_{co} is a crossover temperature from the linear dependence to a "rounded" power law description. This form incorporates a "mean-field-critical crossover form" proposed by Thurston *et al.* [153] and the "rounded" power law emerged in studies of diluted antiferromagnets in magnetic fields [124, 125, 128]. Note that T_C is different from the metastability temperature T_M. T_C is the peak of the Gaussian distribution, whereas the metastability temperature T_M is the temperature above which the ZFC LRO intensity disappears[125].

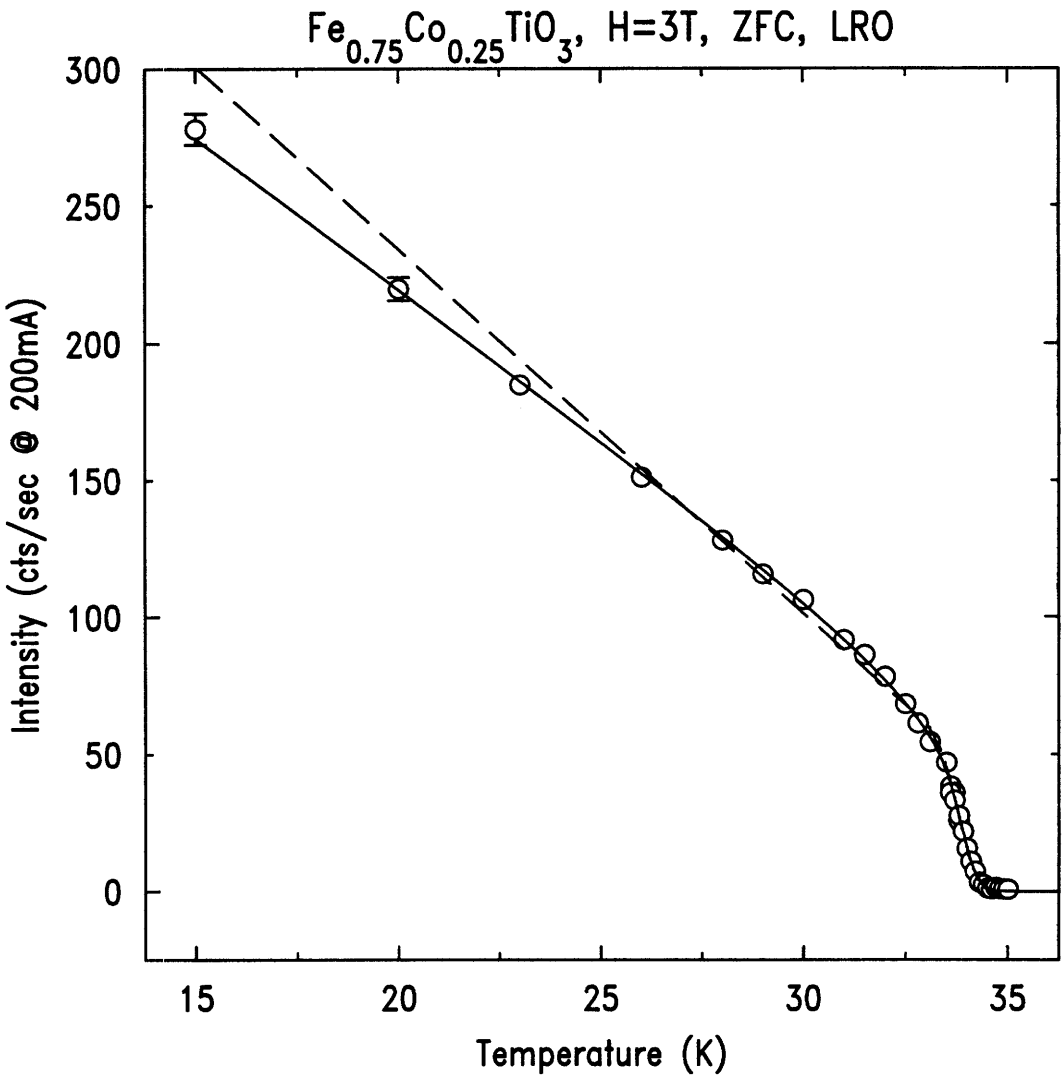

Figure 8-5: The shedding of the long-range order (LRO) on warming from a ZFC state at the external field H=3T. The solid line is a least-squares fit of the data to a heuristic mean-field-rounded-power-law crossover form Eq. 8.4. The dashed line is the best fit of the data to a first order transition with a Gaussian distribution of transition temperatures.

The dashed line in Fig. 8-5 is a least-squares fit of the data to a first order transition [154],

$$I \sim \begin{cases} 0 & \text{if } T > t_c \\ A + B(t_c - T) & \text{if } T \leq t_c \end{cases}$$

where there is a Gaussian distribution of the transition temperature t_c,

$$p(t_c) \sim \exp\left(-\left(\frac{t_c - T_C}{\sigma}\right)^2\right). \tag{8.5}$$

The best fit parameters are $T_C = 33.8(1)$K and $\sigma = 0.5(3)$. Clearly, for the ZFC data in $Fe_{0.75}Co_{0.25}TiO_3$, the rounded power law with a mean field-critical crossover (Eq. 8.4) describes the data better.

The temperature dependence of the LRO on warming from the ZFC state was studied for several different fields. The results are illustrated in Fig. 8-6, in which we plot the evolution of the order parameter squared on warming from the ZFC state for magnetic fields $H = 1$T, 2T and 3T, together with the results from zero field. For $H = 1$T (Fig. 8-6(b)), the transition appears to be sharp, and the data are well described by a simple power law, $I \sim (1 - \frac{T}{T_M(1T)})^{2\beta}$, with $T_M(1T) = 42.45(3)$K, and $\beta = 0.32(3)$. However, for data taken at $H = 2$T (Fig. 8-6(c)), we again see that the data exhibit "rounding" near the phase transition; with a rounding at $H = 2$T which is less pronounced than that at $H = 3$T (Fig. 8-5 or Fig. 8-6(d)). The solid line in Fig. 8-6(c) is the best fit to Eq. 8.4, with the best fit parameters given by: $T_C(2T) = 39.16(5)$K, $\beta = 0.20(5)$, $\sigma(2T) = 0.27(3)$K and $T_{co} = 29.8(1.0)$K. In studies of the RFIM systems $Mn_xZn_{1-x}F_2$ and $Fe_xZn_{1-x}F_2$, it was pointed out that this "rounding" results from the random field, and in particular, in detailed magnetic x-ray studies, it was found that the spread of T_C, σ, increased with increasing magnetic field H like H^2 [124, 125]. The data of $H = 3$T and $H = 2$T for $Fe_{0.75}Co_{0.25}TiO_3$ are clearly consistent with this result, and with this in mind, it is possible that the T_C spread at 1T, $\sigma(1T)$ was too small to be visible. Further the values for the exponent β of the "rounded" power law, 0.20(2) for $H = 2$T and 0.15(3) for $H = 3$T, are consistent with the equivalent results $\beta = 0.20(5)$ from $Mn_xZn_{1-x}F_2$ [124, 125], and

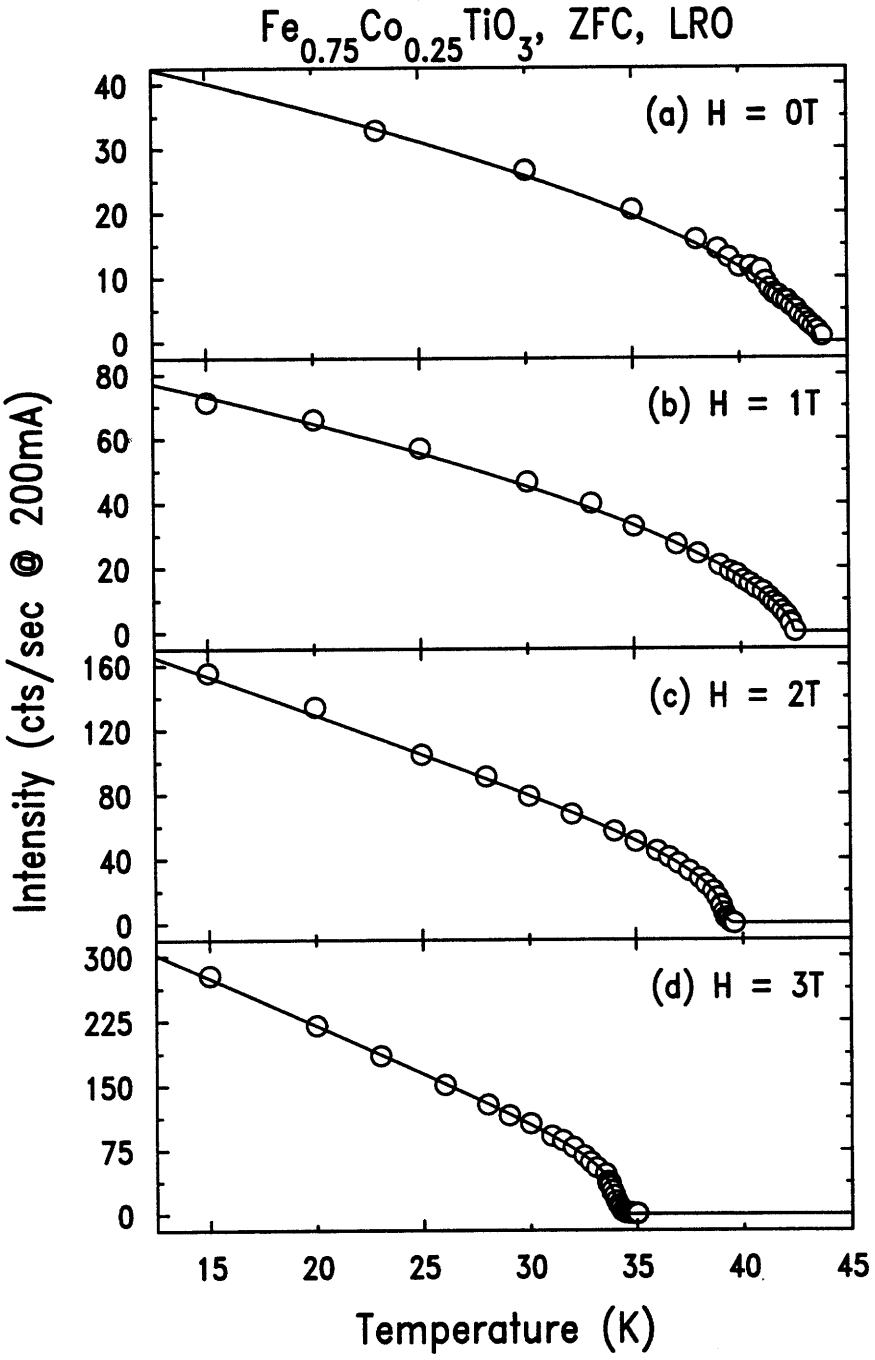

Figure 8-6: The shedding of long-range order (LRO) on warming from the ZFC state in magnetic fields H=1T(b) 2T(c) and 3T(d) is plotted together with the results from zero field(a).

values ranging from 0.21 to 0.12 for $Fe_xZn_{1-x}F_2$ [128, 151].

In Fig. 8-6, we notice the metastability temperature T_M, at which the LRO disappears, decreases with increasing magnetic field, as shown in Fig. 8-7. This also determines the metastability boundary in the H–T plane for $H \leq 3$T. Using scaling arguments, Fishman and Aharony [115] suggest that the random field transition temperature follows the form,

$$T_N(H) = T_N(0) - bH^2 - aH^{2/\phi} \tag{8.6}$$

where bH^2 is the conventional mean field shift, which is very small. In the case of $Fe_{0.75}Co_{0.25}TiO_3$, this term merely produces a shift of 0.06K for a field of 3T. We emphasize that $T_N(H)$ is the temperature at which in equilibrium, a transition to the LRO in the RFIM occurs, but in practice, due to the anomalously slow dynamics above $T_N(H)$, the system falls out of the equilibrium at a higher temperature, the metastability temperature $T_M(H)$, below which the magnetic correlations are history dependent. Nevertheless, we assume here that the scaling arguments that lead to Eq. 8.6 also apply to the metastability boundary $T_M(H)$. The solid line in Fig. 8-7 is the fit of the data to the functional form

$$T_M(H) = T_N(0) - bH^2 - aH^{2/\phi}. \tag{8.7}$$

The best fit exponent ϕ, in a least-squares sense, is $\phi = 1.2(1)$. This value of ϕ is to be compared with the theoretical prediction of $\phi = 1.4$ [155] for Eq. 8.6. In earlier studies of diluted RFIM systems with weak spin anisotropies, it was discovered that for magnetic fields not too far from the bicritical point, the transition temperature was depressed further due to the additional crossover to the bicritical behavior at higher fields. Accordingly, fits of $T_M(H)$ including data approaching the bicritical point yielded a smaller value for the exponent ϕ. This was the case, for example, in $Mn_{0.50}Zn_{0.50}F_2$ [123] ($\phi = 1.15(15)$), and this is also the case in $Fe_{0.75}Co_{0.25}TiO_3$. Specifically, for the magnetic field $H = 4$T, the x-ray scattering profile at the reciprocal lattice point $(1, 1, -1.5)$ differs significantly from those at lower fields, as

shown in Fig. 8-8. This indicates the existence of a multicritical point for a magnetic field value between 3T and 4T. A detailed study of the phase behavior for higher fields are unfortunately prohibited by the extremely weak x-ray scattering intensity. The equivalent result for the crossover exponent ϕ in $Fe_{0.50}Zn_{0.50}F_2$ is $\phi = 1.41(6)$ [126, 151].

Fig. 8-6 also presents us with a rather striking feature. That is, if we fix the temperature at 15K, and read off the ZFC intensity at different magnetic fields of Fig. 8-6, we arrive at the result shown at Fig. 8-9. The intensity data exhibit a quadratic dependence on the magnetic field. The solid line in Fig. 8-9 is the result of a least-squares fit of the data to the function form

$$I(H) = I(0T) + bH^2. \tag{8.8}$$

In the meantime, the x-ray scattering intensity of the charge peak $(2, 2, -3)$, at which the momentum transfer $\vec{Q}$ is collinear with that at $(1, 1, -1.5)$, is independent of the magnetic field as shown in Fig. 8-10. Furthermore, we repeated the same measurements, under the identical conditions, with neutron scattering techniques. The neutron intensity at $(1, 1, -1.5)$ as a function of magnetic field for temperature $T = 15$K is shown by the filled circles in Fig. 8-9. The neutron and x-ray intensities are normalized at zero field. In contrast to the result of x-ray measurements, there is no apparent field-dependence of the neutron intensity at $(1, 1, -1.5)$. If the additional x-ray scattering intensity at $(1, 1, -1.5)$ for the $H = 3$T ZFC state were purely magnetic, this would require either a factor of $\sim \sqrt{7} \simeq 2.6$ increase of the magnetic moment at $H = 3$T, or the same factor increase of the magnetic structure factor, both of which would have also reflected themselves in the neutron scattering intensity at $(1, 1, -1.5)$. But, this is clearly not the result exhibited in Fig. 8-9.

However, the additional x-ray intensity at $(1, 1, -1.5)$ may arise from a lattice distortion. In order to contribute to x-ray scattering intensity at $(1, 1, -1.5)$, this lattice distortion must be such that it doubles the periodicity along the hexagonal c-axis direction. This distortion can be understood as originating from the coupling

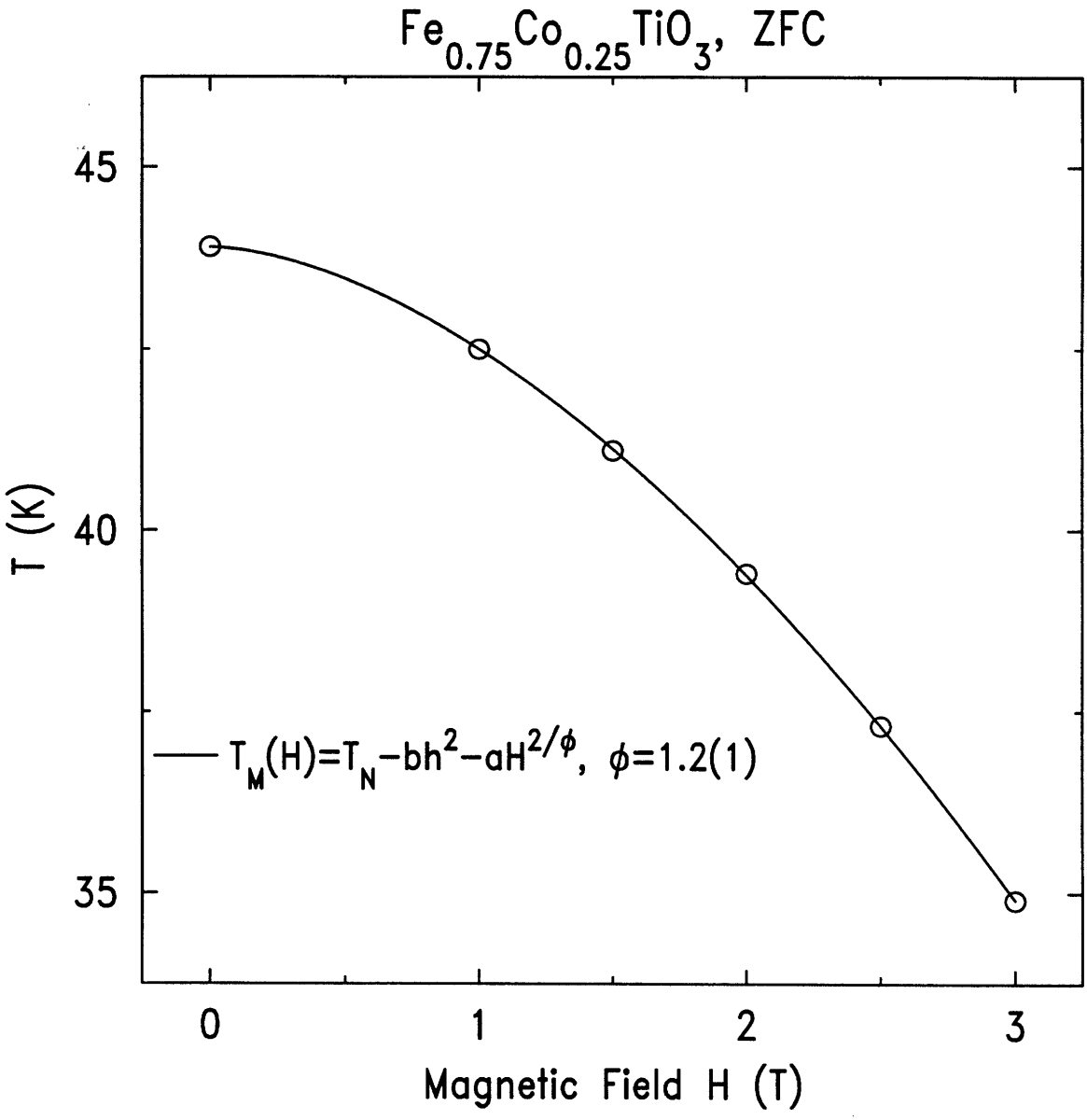

Figure 8-7: The metastability temperature T_M as a function of magnetic field. The solid line is a least-squares fit of the data to the function $T_M(H) = T_N(0) - bH^2 - aH^{2/\phi}$, with the best fit value for the crossover exponent given by $\phi = 1.2(1)$.

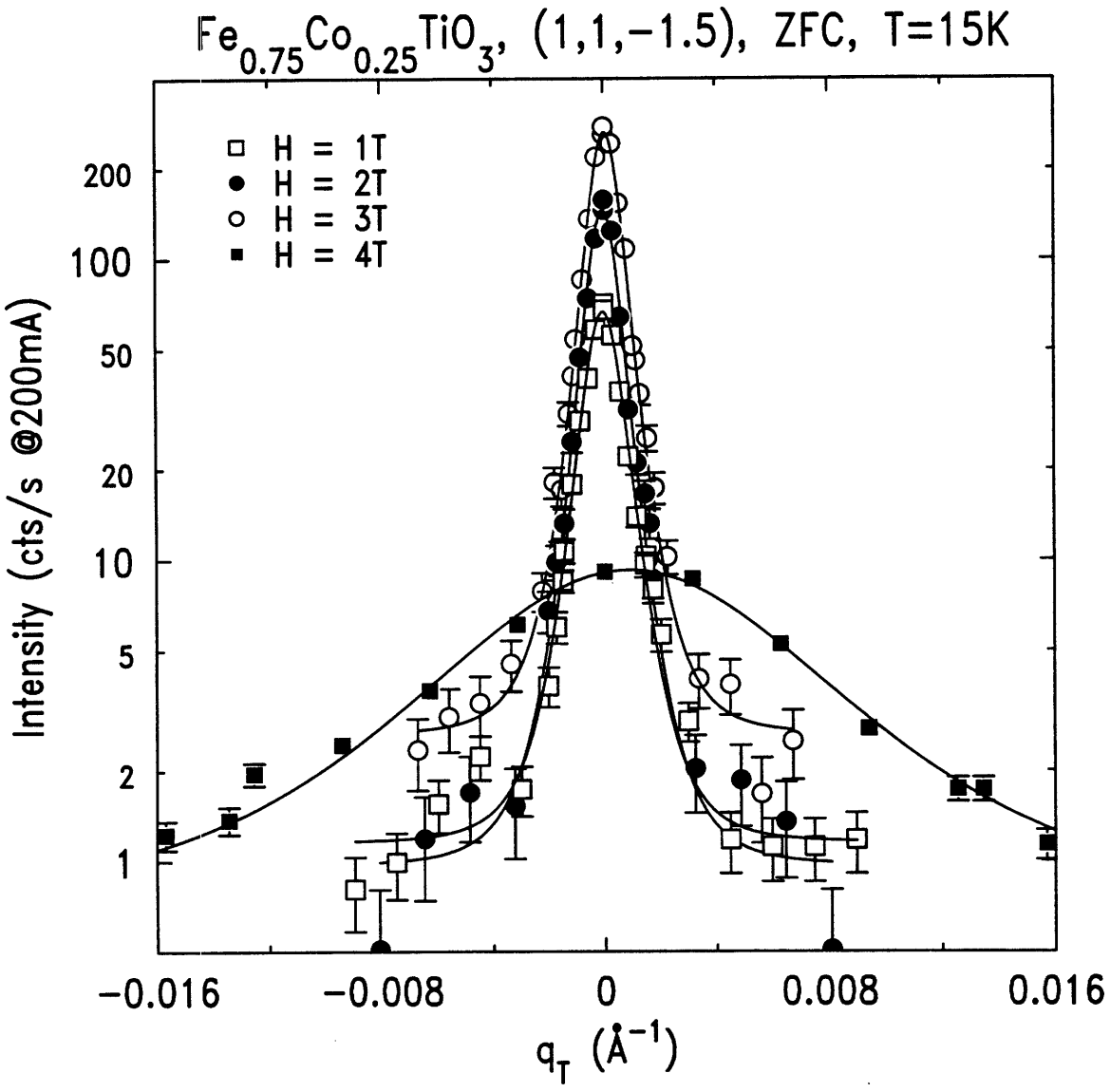

Figure 8-8: The transverse scans in the ZFC state at $T = 15$K for magnetic fields $H = 1$T, 2T, 3T and 4T.

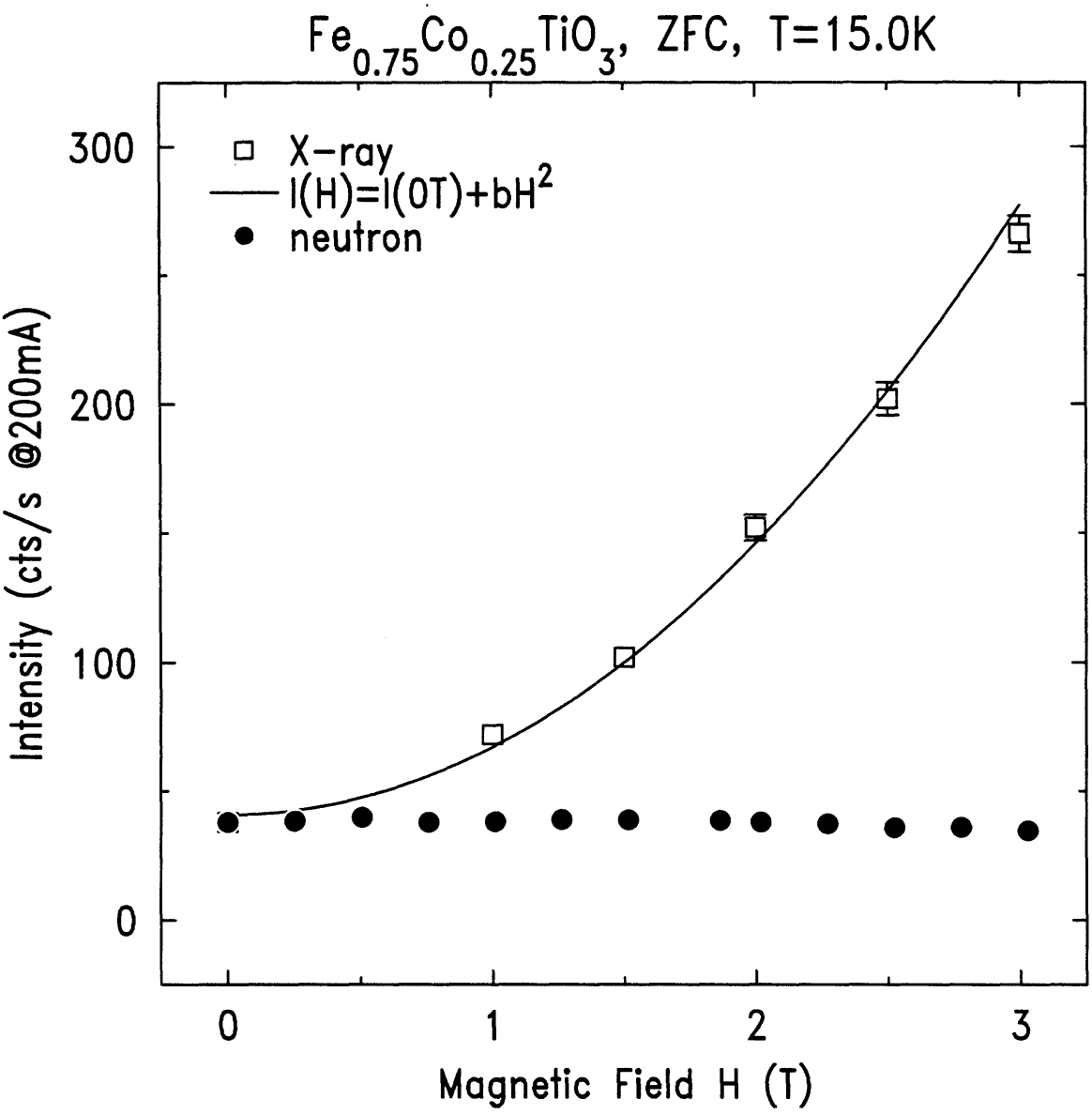

Figure 8-9: The ZFC intensities at $T = 15$K, from x-ray(unfilled squares) and neutron(filled circles) scattering measurements as functions of magnetic field. The x-ray intensity increases with magnetic field quadratically, $I(H) = I(0T) + bH^2$, while the neutron data is almost independent of magnetic field. The x-ray and neutron intensity data are normalized at zero field.

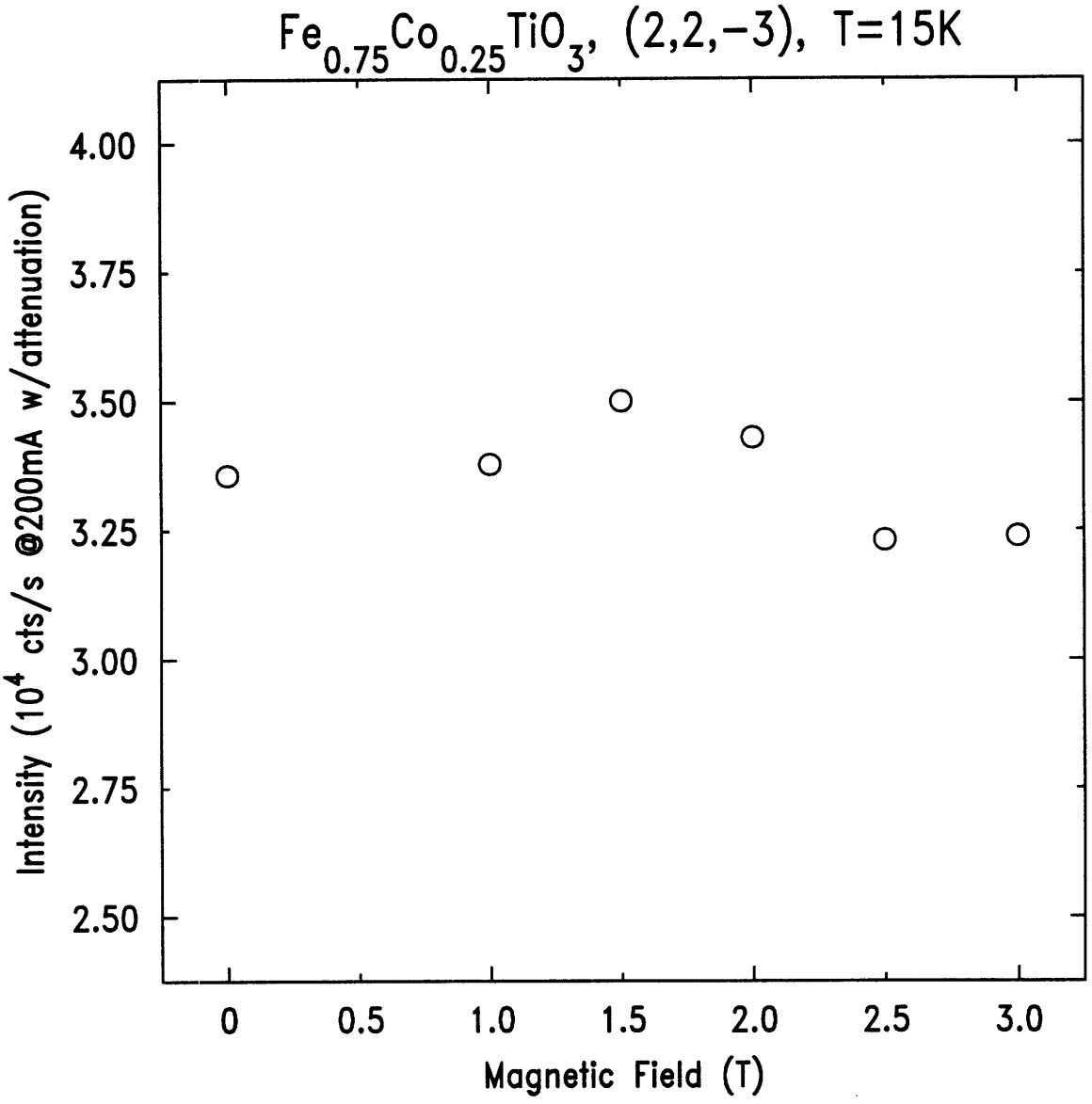

Figure 8-10: The x-ray scattering intensity at $(2, 2, -3)$ as a function of magnetic field for $T = 15$K.

between the lattice and the magnetism via a coupling term of the form $\delta_s M_s M$, in which δ_s is the staggered lattice distortion which contributes to the additional scattering intensity at the reciprocal point $(1, 1, -1.5)$, M_s is the staggered magnetic moment and M is the uniform magnetization. The change of the free energy $\Delta\mathcal{F}$ can then be written as:

$$\Delta\mathcal{F} \sim \gamma\delta_s M_s M + \frac{1}{2}\delta_s^2 \tag{8.9}$$

where $\frac{1}{2}\delta_s^2$ is the increase of the elastic energy due to the distortion. It then follows that

$$\delta_s \sim M_s M. \tag{8.10}$$

The scattering intensity at the reciprocal lattice point $(1, 1, -1.5)$ now includes both the magnetic contribution, $I_M \sim M_s^2$, and the charge scattering arising from this staggered distortion, $I_C \sim \delta_s^2 \sim (M_s M)^2$. For small magnetic fields, the uniform magnetization M is linearly dependent on the external field magnetic field H as shown in Fig. 8-11. In Fig. 8-11, we show the data from a SQUID magnetometry measurement of the uniform magnetization M as a function of magnetic field H at $T = 15$K for $Fe_{0.75}Co_{0.25}TiO_3$. The scattering intensity at $(1, 1, -1.5)$ is then given by

$$I = I_M + I_C \sim M_s^2 + c(M_s M)^2 \sim M_s^2(1 + aH^2), \tag{8.11}$$

which is exactly the result displayed in Fig. 8-9. It is important to note that the temperature dependence of the scattering intensity at the reciprocal lattice point $(1, 1, -1.5)$ continues to reflect the temperature dependence of the sublattice magnetization M_s. The discrepancy between x-ray and neutron measurements of $(1, 1, -1.5)$ may then be attributed to the fact that for neutrons the magnetic and nuclear scattering cross-sections are comparable whereas for x-rays, charge scattering is intrinsically six orders of magnitude larger than magnetic scattering. Thus a 10^{-3} distortion would produce a negligible relative increase in the intensity for neutrons, but would produce intensity comparable to that from the magnetic scattering for x-rays.

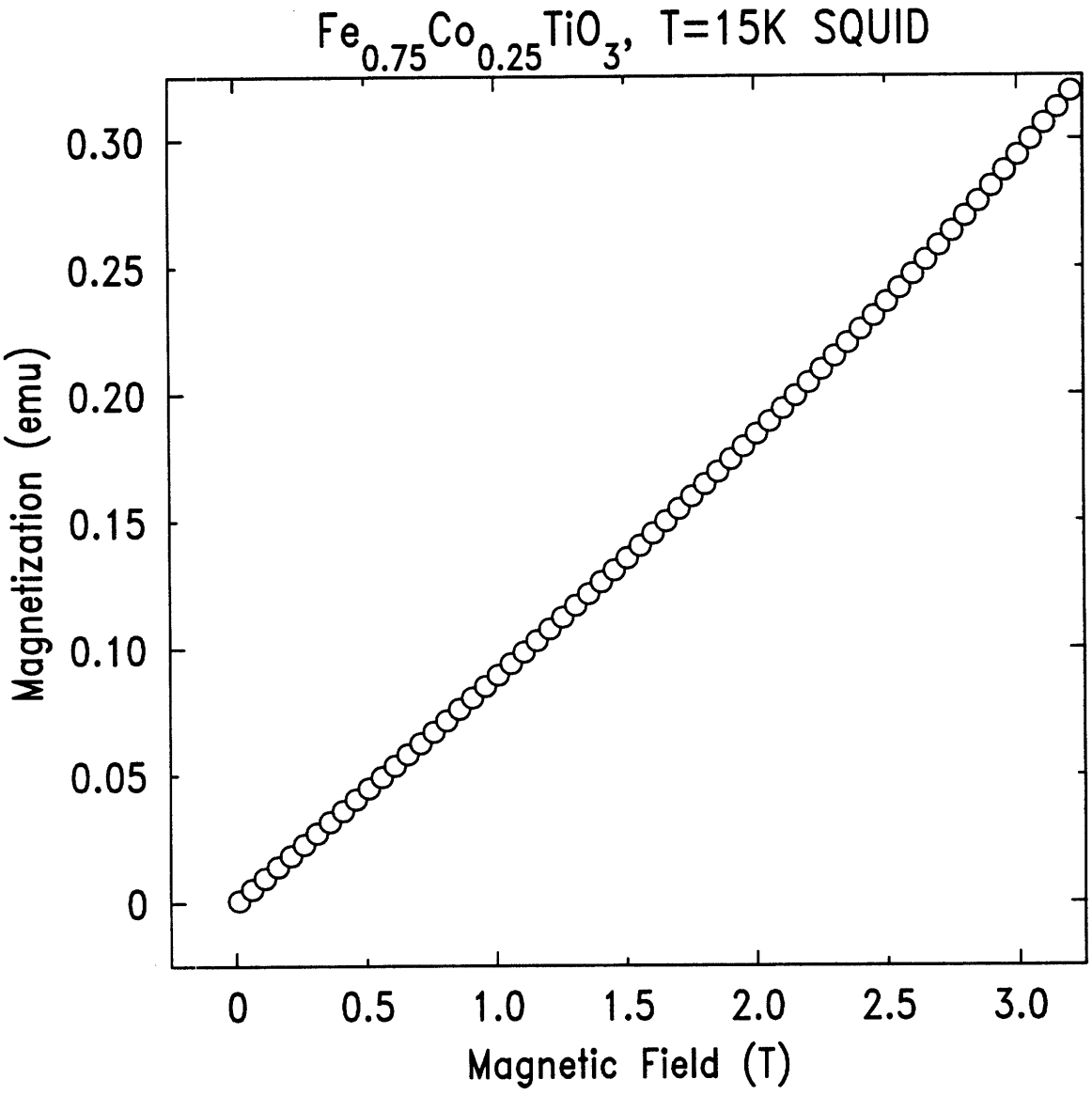

Figure 8-11: The field dependence of the uniform magnetization from a SQUID magnetometry measurement.

8.4 FC Results

We now turn our attention to the FC results, that is, the sample was cooled from the paramagnetic phase in the presence of a magnetic field. A series of FC scans are shown in Fig. 8-12 for several temperatures on cooling at an external magnetic field of 3T. It is evident that the peaks are much broader than the experimental resolution, which is indicated by the dashed lines in Fig. 8-12. The state is, however, not frozen, as the data show a steady evolution of the scattering profile which is very broad at 34.21K and ranges to much narrower (albeit still broader than the resolution) peak at 20.01K. Similar to the situation in the diluted Ising antiferromagnets, the FC data at every temperature could be well described by a cross-section of Lorentzian squared form,

$$S(\mathbf{q}) = \frac{A_0}{\left\{1 + \left[(q_{\mathrm{L}} - q_{\mathrm{L}}^0)/\kappa_{\mathrm{L}}\right]^2 + \left[(q_{\mathrm{T}} - q_{\mathrm{T}}^0)/\kappa_{\mathrm{T}}\right]^2 + \left[(q_{\mathrm{V}} - q_{\mathrm{V}}^0)/\kappa_{\mathrm{V}}\right]^2\right\}^2} \tag{8.12}$$

convoluted with the experimental resolution (Eq. 8.2). The solid lines in Fig. 8-12 are the results of fitting of the data to Eq. 8.12 convoluted with the experimental resolution. This implies that the FC state is composed entirely of short-range ordered domains.

The temperature dependence of the FC state was studied for several different fields. The results of the fits for the inverse domain size, κ_{T}, at several magnetic fields are shown in Fig. 8-13. The domain size, the inverse of κ_{T}, decreases with increasing temperature, and with increasing magnetic field. These are, respectively, the consequences of the increase of thermal disorder and the increase in random field, both of which cause the domain size to decrease. These results are consistent with those obtained from the diluted systems $Mn_xZn_{1-x}F_2$ and $Fe_xZn_{1-x}F_2$ [116, 118, 124, 125].

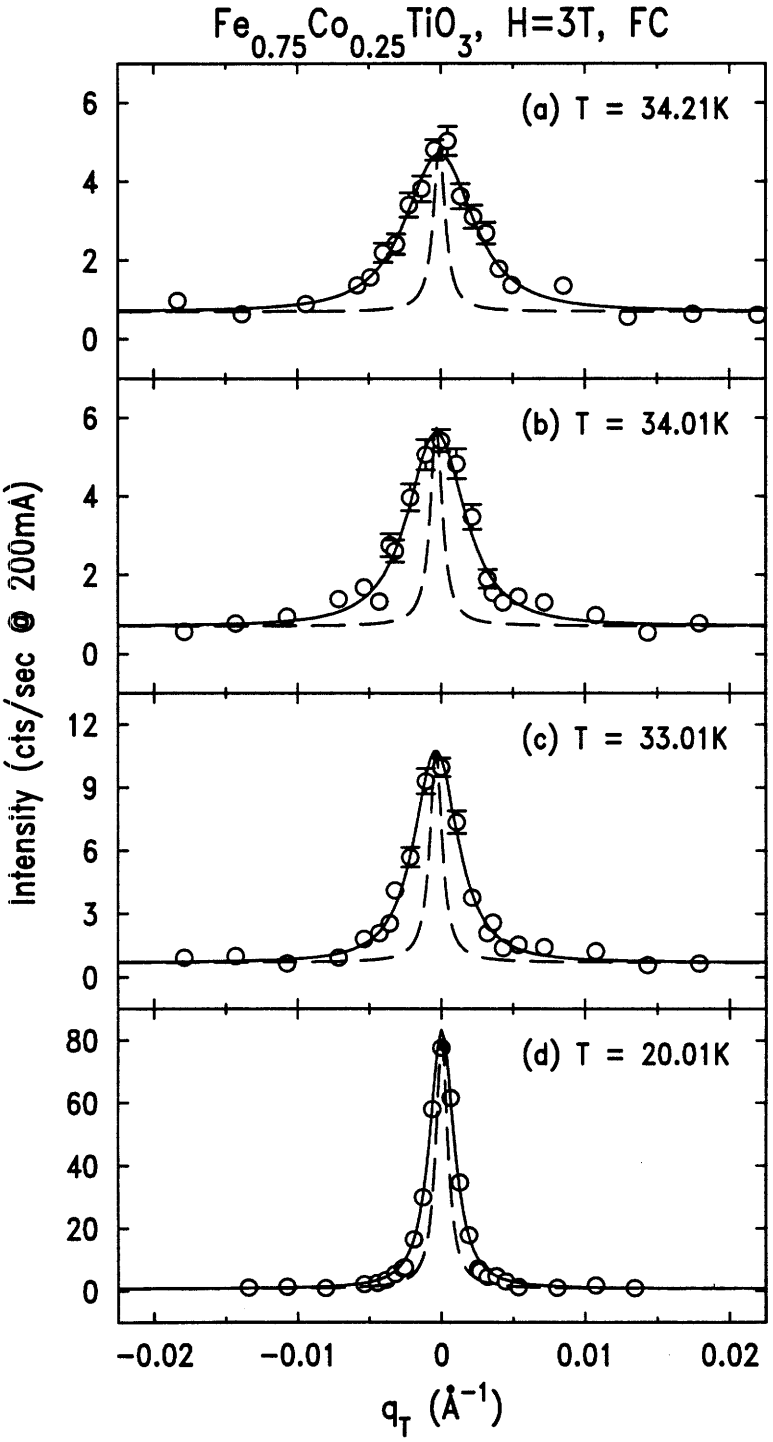

Figure 8-12: Transverse scans through the $(1, 1, -1.5)$ peak in a FC run for H=3T. The solid lines are the fits of the data to Eq. 8.12, convoluted with the experimental resolution, and the dashed lines indicate the experimental resolution.

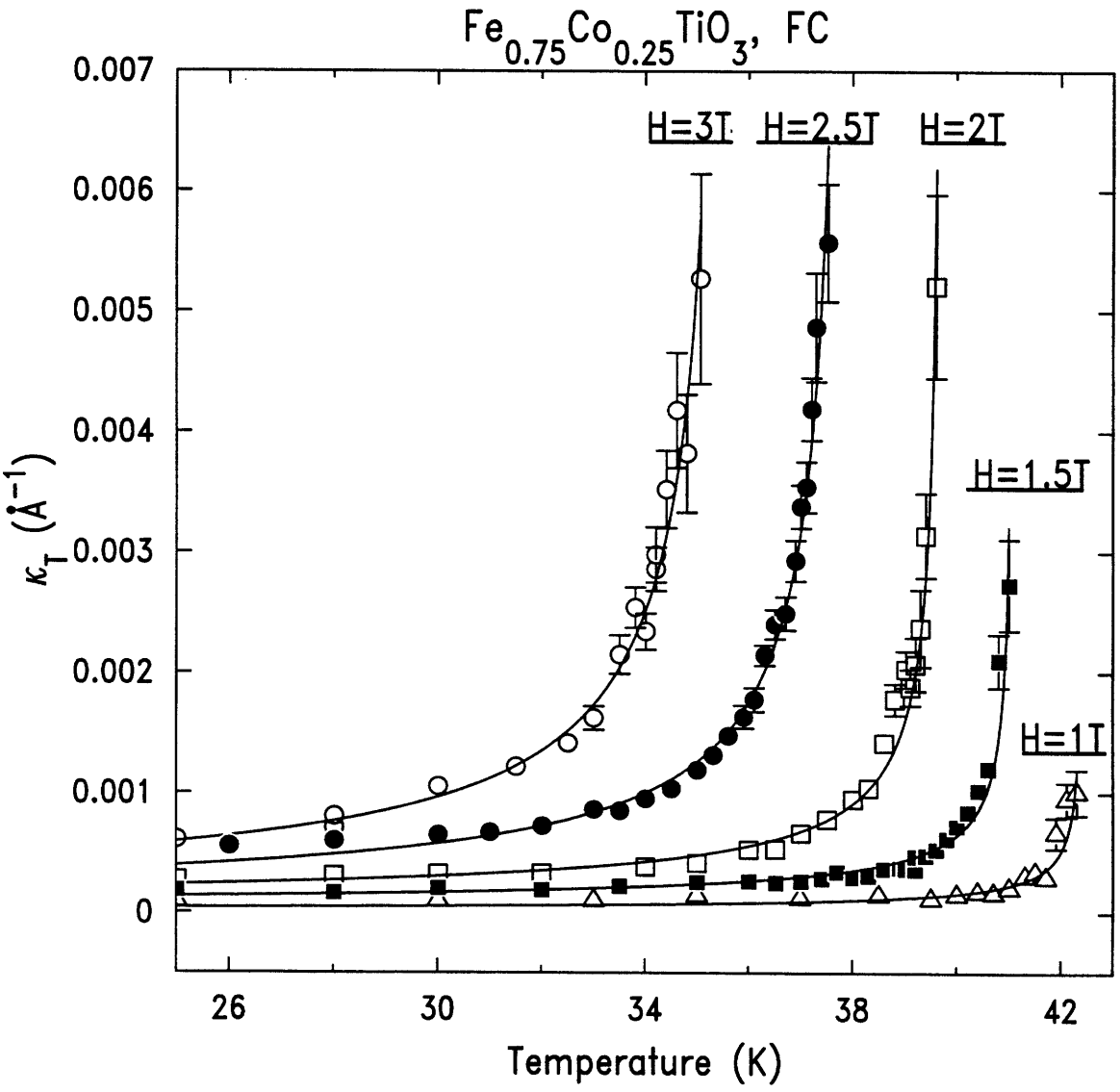

Figure 8-13: The inverse of the domain size, κ, as a function of temperature for several magnetic fields.

8.5 Summary

In many aspects, the random Ising magnet $Fe_{0.75}Co_{0.25}TiO_3$ in a magnetic field appears to be a good realization of the RFIM model. First, at zero field, we find that $Fe_{0.75}Co_{0.25}TiO_3$ undergoes a phase transition at T_N, to a LRO state, which is ferromagnetic within the hexagonal a-b plane, and antiferromagnetic along the c-axis direction, with the spins along the the c-axis. In addition, we find that the transition is well described by a power law, $I \propto \left(1 - \frac{T}{T_N}\right)^{2\beta}$, with the best fit β value of 0.36(3), consistent both with the theoretical value $\beta = 0.35(1)$ for the REIM [147, 148, 149] and with the zero field experimental results of the diluted Ising antiferromagnets $Mn_xZn_{1-x}F_2$ [124, 125] and $Fe_xZn_{1-x}F_2$ [128, 151]. Second, we find that if the sample is cooled in the presence of a magnetic field, then the LRO is not established, and the scattering profiles in the low temperature FC states are well described by a Lorentzian squared cross-section. However, if the sample is cooled to low temperatures first, and a magnetic field subsequently applied then in that case, the LRO is retained on warming until the sample is heated above a field-dependent metastability temperature $T_M(H)$. These history dependent results agree in detail with the results from the studies on the diluted RFIM systems [116, 117, 118, 119, 124, 125]. Third, similar to the "*trompe l'oeil* critical behavior" found in the diluted metal fluorides [124, 125, 128, 151], the loss of the LRO on warming from the ZFC state is found to be well described by a power law with a Gaussian distribution of transition temperatures and a $\beta_{ZFC} \sim 0.15$. Fourth, the metastability temperature, T_M is found to decrease with increasing magnetic field, $T_M H = T_N(0) - bH^2 - aH^{2/\phi}$, with the best fit value for the crossover exponent $\phi = 1.2(1)$. This smaller value (than the theoretical value $\phi = 1.4$) for ϕ arises from the close proximity of a multicritical at higher fields.

Furthermore, we observed a drastic field-dependence of the x-ray, but not the neutron, scattering intensity at the superlattice reciprocal point $(1, 1, -1.5)$. This additional x-ray intensity is believed to arise from a staggered lattice distortion. In particular, the quadratic magnetic field dependence of the additional intensity can be

explained through a lattice and magnetism coupling of the form, $\delta_s M_s M$. It is noted that the temperature dependence of the scattering intensity is still determined by the temperature dependence of the sublattice magnetization. This is a new effect which has not been observed previously in synchrotron x-ray scattering measurements. It may, nevertheless, be important in many magnetic systems with strong spin-lattice coupling.

In summary, we have carried out a detailed synchrotron x-ray-scattering study of the mixed Ising-XY random magnet $Fe_xCo_{1-x}TiO_3$. The measurements demonstrate the power of magnetic x-ray scattering techniques, as well as the importance of quenched disorder in phases and phase transitions in solid state systems.

The phase diagram for $Fe_xCo_{1-x}TiO_3$ in the concentration-temperature (x-T) plane is found to consist of four phases: paramagnet, $S_{\|}$-ordered antiferromagnet, $\vec{S}_{\perp}$-domain state, and a mixed domain state, in which both the $\vec{S}_{\perp}$ and $S_{\|}$ form short-range ordered domains (Fig. 6-2).

The transition from the thermally disordered paramagnet to the $S_{\|}$-order phase (thick solid line BC) is a conventional second-order phase transition ($x = 0.65$, and 0.75). The sublattice magnetization $M_{\|}$ is well described by a simple power law, $M_{\|} \propto \left(1 - \frac{T}{T_{\|}}\right)^{\beta_{\|}}$, the best fit values of $\beta_{\|}$, 0.33(1) for concentration $x = 0.65$ and 0.36(3) for $x = 0.75$, are in good agreement with the theoretical value $\beta = 0.35(1)$ expected for the REIM [147, 148, 149]. The phase behaviors of the random Ising magnet $Fe_{0.75}Co_{0.25}TiO_3$ in external magnetic fields, in many aspects, are consistent with the experimental observation of the RFIM to-date. The drastic increase of the x-ray scattering intensity at the reciprocal lattice point $(1, 1, -1.5)$ is attributed to a field induced staggered lattice distortion.

The transition from the $S_{\|}$ long-range ordered phase to the mixed domain state (thin solid line BE) is smeared ($x = 0.65$), and Ising and XY order parameters are clearly coupled. In particular, the mixed phase is found to contain domains. We therefore verified experimentally the suggestion put forwards by Wong *et al.* in Ref. [141]. Specifically, this domain state is found to be well described by a Lorentzian squared cross-section, consistent with a real space exponential decaying correlation function.

The transition between the paramagnet and the $\vec{S}_{\perp}$-domain state (thick dashed line AB) is a novel phase transition ($x = 0.35$ and 0.50) in the sense that the correlation length diverges along that line, even though there is no low temperature long-range ordered phase. Instead, the low temperature phase contains both magnetic and structural domains.

Furthermore, following the SRO of the spin component $\vec{S}_{\perp}$, through the magnetoelastic coupling, the atomic structure is distorted in the hexagonal a-b plane (Fig. 7-6), and presumably, the magnetoelastic coupling is also responsible for the breakup of the crystal structure into domains. Clearly, it would be highly desirable to repeat the same measurements as reported in this paper on the similar Ising-XY magnetic systems, such as $Fe_xCo_{1-x}Cl_2$ and $Fe_xCo_{1-x}Br_2$.

Bibliography

[1] M. F. Collins, *Magnetic Critical Scattering* (Oxford University Press, New York, 1989).

[2] J. M. Yeomans, *Statistical Mechanics of Phase Transitions* (Clarendon Press, Oxford, 1992).

[3] H. E. Stanley, *Introduction to Phase Transitions and Critical Phenomena* (Oxford Science Publications, New York, 1987).

[4] S.-K. Ma, *Modern Theory of Critical Phenomena* (Addison-Wesley, California, 1982).

[5] R. B. Griffiths, Phys. Rev. Lett. **24**, 1479 (1970).

[6] R. B. Griffiths and J. C. Wheeler, Phys. Rev. **A2**, 1047 (1970).

[7] L. P. Kadanoff, *Proc. 1970 Varenna Summer School on Critical Phenomena* (M. S. Green, Ed.) (Academic Press, New York, 1971).

[8] F. D. M. Haldane, Phys. Rev. Lett. **50**, 1153 (1983).

[9] F. D. M. Haldane, Phys. Lett. **93A**, 464 (1983).

[10] M. Steuner and H. Dachs, Solid State Commun. **9**, 1603 (1971).

[11] R. J. Birgeneau, R. Dingle, M. T. Hutchings, G. Shirane and S. L. Holt, Phys. Rev. Lett. **26**, 718 (1971).

[12] R. J. Birgeneau, J. Skalyo and G. Shirane, Phys. Rev. B **3**, 736 (1971).

[13] E. J. Samuelsen, Phys. Rev. Lett. **31**, 936 (1973).

[14] M. E. Fisher and D. R. Nelson, Phys. Rev. Lett. **32**, 1350 (1974).

[15] D. R. Nelson, J. M. Kosterlitz and M. E. Fisher, Phys. Rev. Lett. **33**, 813 (1974).

[16] J. M. Kosterlitz, D. R. Nelson and M. E. Fisher, Phys. Rev. B **13**, 412(1976).

[17] M. E. Fisher, AIP Conf. Prof. **24**, 273 (1975).

[18] A. Aharony and A. D. Bruce, Phys. Rev. Lett. **33** 427 (1974).

[19] A. Aharony, K. A. Müller and W. Berlinger, Phys. Rev. Lett. **38**, 33 (1977).

[20] A. D. Bruce and A. Aharony, Phys. Rev. B **11**, 478 (1975).

[21] L. D. Landau and I. M. Lifshitz, *Statistical Mechanics* (Pergamon, New York, 1958).

[22] R. E. Peierls, *Quantum Theory of Solids* (Oxford University, London, 1955).

[23] H. Winick, Scientific American, Novermber (1987).

[24] J. D. Jackson, *Classical Electrodynamics* (John Wiley & Sons, New York, 1975).

[25] J. P. Hill, Ph. D. thesis, Massachusetts Institute of Technology, 1992.

[26] P. M. Platzman and N. Tzoar, Phys. Rev. B **2**, 3556 (1970).

[27] F. de Bergevin and P. M. Brunel, Acta. Crystallogr. Sect A **37**, 314 (1981).

[28] P. M. Brunel, G. Patraff, F. de Bergevin, F. Rousseau and M. Lemonnier, Acta. Crystallogr. Sect A **39**, 84 (1983).

[29] D. E. Moncton, F. Gibbs and J. Bohr, Nucl. Instrum. Methods **A26**, 839 (1986).

[30] G. Beni and P. Pincus, J. Chem. Phys. **57**, 3531 (1972).

[31] M. C. Cross and D. S. Fisher, Phys. Rev. B **19**, 402 (1979).

[32] J. W. Bray, H. R. Hart Jr., L. V. Interrante, I. S. Jacobs, J. S. Kasper, G. D. Watkins, S. H. Wee and J. C. Bonner, Phys. Rev. Lett. **35** 744 (1975).

[33] I. S. Jacobs, J. W. Bray, H. R. Hart Jr., L. V. Interrante, J. S. Kasper,G. D. Watkins, D. E. Prober and J. C. Bonner, Phys. Rev. B **14**, 3036 (1976).

[34] D. E. Moncton, R. J. Birgeneau, L. V. Interrante and F. Wudl, Phys. Rev. Lett. **39**, 507 (1977).

[35] J. des Cloizeaux and J. J. Pearson, Phys. Rev. **128**, 2131 (1962).

[36] J. W. Bray, L. V. Interrante, I. S. Jacobs and J. C. Bonner, in *Extended Linear Chain Compounds*, edited by J. S. Miller (Plenum, New York, 1983).

[37] E. Pytte, Phys. Rev. B **10**, 4637 (1974).

[38] P. Jordan and E. Wigner, Z. Phys. **47**, 631 (1928).

[39] S. Rodriquez, Phys. Rev. **116**, 1474 (1959).

[40] T. D. Schultz, D. C. Mattis and E. H. Lieb, Rev. Mod. Phys. **36**, 856 (1964).

[41] L. N. Bulaevskii, Zh. Eksp. Theor. Fiz. **43**, 968 (1962), [Sov. Phys.-JETP **16**, 685 (1963)].

[42] H. Fröhlich, Proc. R. Soc. A **223**, 296 (1954).

[43] G. Rickayzen, *Theory of Superconductivity* (John Wiley, New York, 1965).

[44] G. Beni, J. Chem. Phys. **58**, 3200 (1973).

[45] P. Pincus, Solid State Commun. **9**, 1971(1971).

[46] A. Luther and I. Peschel, Phys. Rev. B **12**, 3908 (1975).

[47] J. M. Luttinger, J. Math. Phys. **4**, 1154 (1963).

[48] D. C. Mattis and E. H. Lieb, J. Math. Phys. **6**, 304 (1965).

[49] W. Duffy, Jr. and K. P. Barr, Phys. Rev. **165**, 647 (1968).

[50] J. W. Bray, Solid State Commun. **26**, 771 (1978).

[51] L. N. Bulaevskii, A. I. Buzdin and D. I. Khomskii, Solid State Commun. **27**, 5 (1978).

[52] M. C. Cross, Phys. Rev. B **20**, 4606 (1979).

[53] V. Kiryukhin, B. Keimer and D. E. Moncton, Phys. Rev. Lett. **74**, 1669 (1995).

[54] V. Kiryukhin and B. Keimer, Phys. Rev. B **52**, R704 (1995).

[55] H. M. McConnell, R. Lynden-Bell, J. Chem. Phys. **36**, 2393 (1962).

[56] D. D. Thomas, H. Keller and H. M. McConnell, J. Chem. Phys. **39**, 2321 (1962).

[57] D. B. Chesnut, J. Chem. Phys. **45**, 4677 (1966).

[58] S. Huizinga, J. Kommandeur, G. A. Sawatzky, B. T. Thole, K. Kopenga, W. J. M. de Jonge and D. Roos, Phys. Rev. B **19** 4723 (1979).

[59] H. Völlenkle, A. Wittmann and H. Nowotony, Monatsh. Chem. **98**, 1352 (1967).

[60] *Structure Report* **32A**, 494 (1967).

[61] M. Nishi, O. Fujita and J. Akimitsu, Phys. Rev. B **50**, 6508 (1994).

[62] M. Hase, I. Terasaki, Y. Sasago, K. Uchinokura and H. Obara, Phys. Rev. Lett. **70**, 3651 (1993).

[63] Q. J. Harris, Q. Feng, R. J. Birgeneau, K. Hirota, G. Shirane, M. Hase and K. Uchinokura, Phys. Rev. B **52** 15 420 (1995).

[64] O. Fujita, J. Akimitsu, M. Nishi and K. Kakurai, Phys. Rev. Lett. **74**, 1677 (1995).

[65] O. Kamimura, M. Terauchi, M. Tanaka, O. Fujita and J. Akimitsu, J. Phy. Soc. Jpn. **63**, 2467 (1994).

[66] J. P. Pouget, L. P. Regault, M. Ain, B. Hennion, J. P. Renard, P. Veillet, G. Dhalenne and A. Revcolevschi, Phys. Rev. Lett. **72**, 4037 (1994).

[67] K. Hirota, D. E. Cox, J. E. Lorenzo, G. Shirane, J. M. Tranquada, M. Hase, K. Uchinokura, H. Kojima, Y. Shibuya and I. Tanaka, Phys. Rev. Lett. **73**, 736 (1994).

[68] E. D. Specht, Ph.D. thesis, Massachusetts Institute of Technology, 1986.

[69] M. Hase, I. Terasaki, K. Uchinokura, M. Tokunaga, N. Miura and H. Obara, Phys. Rev. B **48**, 9616 (1993).

[70] K. Hirota, G. Shirane, Q. J. Harris, Q. Feng, R. J. Birgeneau, M. Hase and K. Uchinokura, Phys. Rev. B **72**, 15 412 (1995).

[71] Q. J. Harris, Q. Feng, R. J. Birgeneau, K. Hirota, K. Kakurai, J. E. Lorenzo, G. Shirane, M. Hase, K. Uchinokura, H. Kojima, T. Tanaka and Y. Shibuya, Phys. Rev. B **50** 12 606 (1994).

[72] J. C. Bonner and M. E. Fisher, Phy. Rev. **135**, A640 (1964).

[73] G. Castilla, S. Chakravarty and V. J. Emery, Phys. Rev. Lett. **75**, 1823 (1995).

[74] L. F. Mattheiss, Phys. Rev. B **49**, 14050 (1994).

[75] J. Zhang, A. R. Bishop and D. Schmeltzer, Phys. Rev. B **52**, 6723 (1995).

[76] J. Riera and A. Dobry, Phys. Rev. B **51** 16098 (1995).

[77] J. Riera and S. Koval, Phys. Rev. B **53**, 770 (1996).

[78] T. Barnes, E. Dagotto, J. Riera and E. S. Swanson, Phys. Rev. B **47**, 3196 (1993).

[79] T. M. Rice, S. Gopalan, M. Sigrist and F. C. Zhang (unpublished).

[80] M. L. Plumer, Phys. Rev. B, **53**, 594 (1996).

[81] J. E. Lorenzo, K. Hirota, G. Shirane, J. M. Tranquada, M. Hase, K. Uchinokura, H. Kojima, T. Tanaka and Y. Shibuya, Phys. Rev. B **50**, 1278 (1994).

[82] N. W. Ashcroft and N. D. Mermin, *Solid State Physics* (Saunders, Philadelphia, 1976).

[83] K. Kindo *et al.*, preprint, 1994.

[84] A. D. Bruce and R. A. Cowley, *Structural Phase Transitions* (Taylor & Francis, London, 1981).

[85] H. Winkelmann, E. Gamper, B. Büchner, M. Braden, A. Revcolevschi and G. Dhalenne, Phys. Rev. B **51**, 12884 (1995).

[86] M. Poirier, M. Castonguay, A. Revcolevschi and G. Dhalenne, Phys. Rev. B **51**, 6147 (1995).

[87] M. Poirier, M. Castonguay, A. Revcolevschi and G. Dhalenne, Phys. Rev. B **52**, 16058 (1995).

[88] M. Saint-Paul, G. Reményi, N. Hegmann, P. Monceau, G. Dhalenne and A. Revcolevschi, Phys. Rev. B **52**, 15298 (1995).

[89] T. R. Thurston, G. Helgesen, L. D. Gibbs, J. P. Hill, B. D. Gaulin and G. Shirane, Phys. Rev. Lett., **70** 3151(1993).

[90] T. R. Thurston, G. Helgesen, J. P. Hill, L. D. Gibbs, B. D. Gaulin and P. J. Simpson, Phys. Rev. B **49** 15730(1994).

[91] P. M. Gehring, K. Hirota, C. F. Majkrzak and G. Shirane, Phys. Rev. Lett., **71** 1087(1993).

[92] P. Gehring, K. Hirota, C. F. Majkrzak and G. Shirane, Phys. Rev. B **51**, 3234 (1995).

[93] K. Hirota, G. Shirane, P. M. Gehring and C. F. Majkrzak, Phys. Rev. B **49** 11967(1994).

[94] T. W. Ryan, R. J. Nelmes, R. A. Cowley and A. Gibaud, Phys. Rev. Lett. **56**, 2704 (1986).

[95] A. Gibaud, T. W. Ryan and R. J. Nelmes, J. Phys. C **20**, 3833 (1987).

[96] A. Gibaud, R. A. Cowley and P. W. Mitchell, J. Phys. C **20** 3849(1987).

[97] S. R. Andrews, J. Phys. C **11**, 3721(1986).

[98] K. Hirota, J. P. Hill, S. M. Shapiro, G. Shirane and Y. Fujii, Phys. Rev. B **52**, 13195 (1995).

[99] U. J. Nicholls and R. A. Cowley, J. Phys. C, **20** 3417(1987).

[100] D. F. McMorrow, N. Hamaya, S. Shimomura, Y. Fujii, S. Kishimoto and H. Iwasaki, Solid State Commun. **76** 443(1990).

[101] H. B. Neumann, U. Rütt, J. R. Schneider and G. Shirane, Phys. Rev. B, **52**, 3981 (1995).

[102] T. Nattermann and J. Villain, Phase Transitions, **11**, 5 (1988).

[103] D. Mukamel and E. Pytte, Phys. Rev. B **25**, 4779 (1982).

[104] R. A. Cowley, H. Yoshizawa, G. Shirane, M. Hagen and R. J. Birgeneau, Phys. Rev. B **30**, 6650 (1984).

[105] A. Aharony, R. J. Birgeneau, C. W. Garland, Y-J. Kim, V. V. Lebedev, R. R. Netz and M. J. Young, Phys. Rev. Lett. **74**, 5064 (1995).

[106] M. Schwartz and A. Soffer, Phys. Rev. B **33** 2059(1986).

[107] M. Gofman, J. Adler, A. Aharony, A. B. Harris and M. Schwartz, Phys. Rev.Lett. **71** 1569(1993).

[108] J. G. Le Guillou and J. Zinn-Justin, Phys. Rev. B **21**, 3976 (1980).

[109] A. J. Guttman, Phys. Rev. B **33**, 5039 (1986).

[110] M. Altarelli, M. D. Núñez-Regueiro and M. Papoular, Phys. Rev. Lett., **74** 3840(1995).

[111] See for example P. W. Mitchell, R. A. Cowley, H. Yoshizawa, P. Bóni, Y. J. Uemura and R. J. Birgeneau, Phys. Rev. B **34**, 4719 (1986).

[112] A. Weinrib and B. I. Halperin, Phys. Rev. B **27**, 413 (1983).

[113] See for example G. Nounesis, M. J. Young, K. I. Blum, C. W. Garland and R. J. Birgeneau, Z. Phys. B **90**, 357 (1993).

[114] Y. Imry and S.-K. Ma, Phys. Rev. Lett. **35**, 1399 (1975).

[115] S. Fishman and A. Aharony, J. Phys. C **12**, L729 (1978).

[116] R. J. Birgeneau, R. A. Cowley, G. Shirane and H. Yoshizawa, J. Stat. Phys. **34**, 817 (1984).

[117] D. P. Belanger, S. M. Rezende, A. R. King and V. Jaccarino, J. Appl. Phys. **57**, 3294 (1985).

[118] R. A. Cowley, R. J. Birgeneau and G. Shirane, Physica **A140**, 285 (1986).

[119] D. P. Belanger, Phase Transitios **11**, 53 (1988).

[120] P. Wong and J. W. Cable, Phys. Rev. B **28**, 5361 (1983).

[121] R. A. Cowley, H. Yoshizawa, G. Shirane and R. J. Birgeneau, Z. Phys. B **58**, 15 (1984).

[122] H. Yoshizawa, R. A. Cowley, G. Shirane and R. J. Birgeneau, Phys. Rev. B **31**, 4548 (1985).

[123] R. A. Cowley, G. Shirane, H. Yoshizawa, Y. J. Uemura and R. J. Birgeneau, Z. Phys. B **75**, 303 (1989).

[124] J. P. Hill, Q. Feng, R. J. Birgeneau and T. R. Thurston, Phys. Rev. Lett. **70**, 3655 (1993).

[125] J. P. Hill, Q. Feng, R. J. Birgeneau and T. R. Thurston, Z. Phys. B **92**, 285 (1993).

[126] D. P. Belanger, A. R. King, V. Jaccarino and J. L. Cardy, Phys. Rev. B **28**, 2522 (1983).

[127] A. R. King and V. Jaccarino, Phys. Rev. B **43**, 10797 (1991).

[128] R. J. Birgeneau, Q. Feng, Q. J. Harris, J. P. Hill, A. P. Ramirez and T. R. Thurston, Phys. Rev. Lett., **75**, 1198 (1995).

[129] D. S. Fisher, M. P. A. Fisher and D. A. Huse, Phys. Rev. B **43**, 130 (1990).

[130] A. Aharony and E. Pytte, Phys. Rev. Lett. **45**, 1583 (1980).

[131] J. Villain and J. F. Fernandez, Z. Phys. B **54**, 139 (1984).

[132] A. Aharony and E. Pytte, Phys. Rev. B **27**, 5872 (1983).

[133] E. M. Chudnovsky, J. Applied Phys. **64**, 5771 (1988) and the references therein.

[134] M. J. P. Gingras and D. A. Huse, Phys. Rev. B **53**, 15193 (1996).

[135] Ralph W. G. Wyckoff, *Crystal Structure* (John Wiley & Sons, New York, 1964).

[136] G. Shirane, S. J. Pickart, R. Nathans and Y. Ishikawa, J. Phys. Chem. Solids **10**, 35 (1959).

[137] R. E. Newnham, J. H. Fang and R. P. Santoro, Acta Cryst. **17**, 240 (1964).

[138] J. B. Goodenough and J. J. Stickler, Phys. Rev. **164**, 768 (1967).

[139] A. Ito, S. Morimoto, Y. Someya, Y. Syono and H. Takei, Solid State Commun. **41**, 507 (1982).

[140] A. Ito, S. Morimoto, Y. Someya, Y. Syono and H. Takei, J. Phys. Soc. Jpn. **51**, 3173 (1982).

[141] P.-Z. Wong, P. M. Horn, R. J. Birgeneau, C. R. Safinya and G. Shirane, Phys. Rev. Lett. **45**, 1974 (1980).

[142] P. Wong, P. M. Horn, R. J. Birgeneau and G. Shirane, Phys. Rev. B **27**, 428 (1983).

[143] K. Katsumata, J. Tuchendler and S. Legrand, Solid State Commun. **49**, 83 (1984).

[144] K. Katsumata, J. Tuchendler and S. Legrand, Phys. Rev. B **30** 1377 (1984).

[145] K. Katsumata, S. M. Shapiro, M. Matsuda, G. Shirane and J. Tuchendler, Phys. Rev. B **46**, 14906 (1992).

[146] M. Blume and D. Gibbs, Phys. Rev. B **37**, 1779 (1988).

[147] K. E. Newman and E. K. Riedel, Phy. Rev. B **25**, 264 (1982).

[148] G. Jug, Phys. Rev. B **27** 609 (1983).

[149] I. O. Maier and A. I. Sokolov, Fiz. TveRd. Tela (Leningrad) **26**, 3453 (1984) [Sov. Phys.—Solid State **26**, 2076 (1984)].

[150] G. Helgesen, J. P. Hill, T. R. Thurston, D. Gibbs, J. Kwo and M. Hong, Phys. Rev. B **50**, 299990 (1994).

[151] J. P. Hill, Q. Feng, Q. J. Harris, R. J. Birgeneau, A. P. Ramirez and A. Cassanho, preprint (1996).

[152] P. Wong, S. von Molnar and P. Dimon, Solid State Commun. **48**, 573 (1983).

[153] T. R. Thurston, C. J. Peters, R. J. Birgeneau and P. M. Horn, Phys. Rev. B **37**, 9559 (1988).

[154] P. Wong, submitted.

[155] A. Aharony, Europhys. Lett. **1**, 617 (1986).